

**Processing and Properties of Boron Carbide  
based Composite with Rare Earth Metal  
Oxide as Sinter Additive**

*By*

**SAIRAM K**

**Enrolment No.: ENGG01201304036**

**Bhabha Atomic Research Centre, Mumbai**

*A thesis submitted to the  
Board of Studies in Engineering Sciences*

*In partial fulfillment of requirements*

*For the Degree of*

**DOCTOR OF PHILOSOPHY**

**of**

**HOMI BHABHA NATIONAL INSTITUTE**

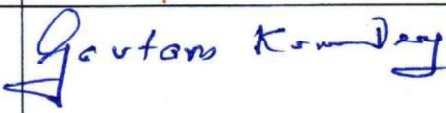
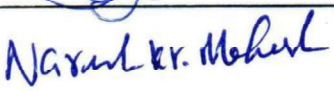


**October, 2020**

# Homi Bhabha National Institute

## Recommendations of the Viva Voce Committee

As members of the Viva Voce Committee, we certify that we have read the dissertation prepared by **K Sairam** titled "**Processing and properties of boron carbide based composites with rare earth oxide as sinter additive**" and recommend that it may be accepted as fulfilling the thesis requirement for the award of Degree of Doctor of Philosophy.

Viva Voce Committee		Signature	Date
Chairman:	Prof. Srikumar Banerjee		14.10.2020
Guide / Convener:	Prof. Tarasankar Mahata		14.10.2020
Co-guide:	Prof. Bikramjit Basu		14.10.2020
Examiner:	Prof. Amartya Mukhopadhyay		14.10.2020
Member-1:	Prof. G.K. Dey		14/10/2020
Member-2:	Prof. (Mrs.) S.B. Roy		14.10.2020
Member-3:	Prof. N.K. Maheshwari		14/10/2020

Final approval and acceptance of this thesis is contingent upon the candidate's submission of the final copies of the thesis to HBNI.

I/We hereby certify that I/we have read this thesis prepared under my/our direction and recommend that it may be accepted as fulfilling the thesis requirement.

Date: 14.10.2020

Place: HBNI

  
Signature  
(Co-Guide)

  
Signature  
(Guide)

## STATEMENT BY AUTHOR

This dissertation has been submitted in partial fulfillment of requirements for an advanced degree at Homi Bhabha National Institute (HBNI) and is deposited in the Library to be made available to borrowers under rules of the HBNI.

Brief quotations from this dissertation are allowable without special permission, provided that accurate acknowledgement of source is made. Requests for permission for extended quotation from or reproduction of this manuscript in whole or in part may be granted by the Competent Authority of HBNI when in his or her judgment the proposed use of the material is in the interests of scholarship. In all other instances, however, permission must be obtained from the author.



**K. Sairam**

## DECLARATION

I, hereby declare that the investigation presented in the thesis has been carried out by me. The work is original and has not been submitted earlier as a whole or in part for a degree / diploma at this or any other Institution / University.



**K. Sairam**

## List of Publications arising from the thesis

### Journal

1. “Influence of spark plasma sintering parameters on densification and mechanical properties of boron carbide”, **K. Sairam**, J.K. Sonber, T.S.R.Ch. Murthy, C. Subramanian, R.K. Fotedar, P. Nanekar, R.C. Hubli. *International Journal of Refractory Metals and Hard Materials*, **2014**; 42: 185–192.
2. “Competition between densification and microstructure development during spark plasma sintering of B<sub>4</sub>C–Eu<sub>2</sub>O<sub>3</sub>”, **K. Sairam**, B. Vishwanadh, J.K. Sonber, T.S.R.Ch. Murthy, S. Majumdar, T. Mahata, B. Basu. *Journal of the American Ceramic Society*, **2018**; 101[6]: 2516-2526.
3. “Effect of rare earth oxide (Eu<sub>2</sub>O<sub>3</sub>) addition on mechanical and thermo-physical properties of B<sub>4</sub>C” (*manuscript under preparation*).

### Chapters in books and lectures notes

1. “Mechanical properties of HfB<sub>2</sub> reinforced B<sub>4</sub>C matrix ceramics processed by in situ reaction of B<sub>4</sub>C, HfO<sub>2</sub> and CNT”, **K. Sairam**, T. S. R. Ch. Murthy, J. K. Sonber, C. Subramanian, R. C. Hubli, A. K. Suri, in: Materials Challenges and Testing for Manufacturing, Mobility, Biomedical Applications and Climate. Eds. W. Udomkitchdecha, Th. Böllinghaus, A. Manonukul, J. Lexow, *Springer International Publishing*, ISBN: 978-3-319-11340-1; **2014**: 87-96.

### Conferences

1. “Feasibility of sintering carbide ceramic by SPS technique under pressureless sintering conditions” 4<sup>th</sup> Global Young Investigator Forum: Novel Ceramic Processing Methods and Synthesis Routes, **K. Sairam**, J.K. Sonber, T.S.R.Ch. Murthy, C. Subramanian, and R.C. Hubli. 39<sup>th</sup> International Conference & Exposition on Advanced Ceramics & Composites (39<sup>th</sup> ICACC) organized by The American Ceramic Society, Florida [**2015**].
2. “Scratch test of boron carbide composites”, **K. Sairam**, K.A. Bharath Krishna, A. Sashanka, J.K. Sonber, T.S.R.Ch. Murthy, R.D. Bedse, B. Sunil Kumar, Kulwant Singh, G.V.S. Nageswara Rao, T. Srinivasa Rao, J.K. Chakravarty, Conference on Advances in Refractory and Reactive Metals and Alloys (ARRMA) at BARC, Mumbai, (**2016**).



**K. Sairam**

*Dedicated to*

*Bhagawan Sri Sathya Sairam, Teachers, Friends and Shri.Rajagopalan (Grandfather)  
(late), Relatives (Murali, Prema, Magesh, Kasthuri, Mannar, Renga, Alagar, Lalitha),  
Meenakshi (Mother), Sushma Sairam (Spouse), Sai Granthii (Daughter) and Scooby.*

## ACKNOWLEDGEMENTS

I wish to express my sincere and grateful thanks to my guides, Dr. R.C. Hubli, Prof. Bikramjit Basu and Dr. Tarasankar Mahata for providing me this interesting project and most importantly, an opportunity to work with them. I am thankful for their invaluable advice and support throughout every step of this research work.

I would also like to thank Doctoral Committee (DC-II) Chairman Dr. Srikumar Banerjee and other respected members of the Committee for reviewing my progress and giving valuable technical inputs. Special thanks to Dr. A.K. Suri, Dr. J.K. Chakravartty and Dr. G.K. Dey, former Directors, Materials Group, BARC, for their concerns on my research and career. I extend my sincere thanks to Dr. Madangopal Krishnan (Associate Director, Materials Group, BARC) and Dr. Vivekanand Kain (Head, MP&CED, BARC) for providing facilities and extending their help as and when required.

I extend my sincere thanks to Dr. Sanjib Majumdar (Head, HTMDS), Shri. C. Subramanian, Dr. T.S.R.Ch. Murthy, Dr. Jitender Sonber, Shri R.D. Bedse, Dr. B. Vishwanadh, Dr. P. Nanekar, Dr. A. Nagaraj, Dr. A.K. Sahu, Dr. P.K. Patro, Dr. R.K. Lenka, Dr. B. Paul, Shri K. Nachiket, Smt. N. Jothilakshmi and Prof. Basu's IISc lab. members for their valuable technical support.

Finally, I would like to express my sincere thanks to my mother, relatives and friends (Dr. Uttam Jain, Shri Sagar Sonak, Smt. Jothilakshmi, Dr. B. Sunil Kumar, Dr. Abhisek Mukherjee, Shri P.T. Rao, Dr. Sanjay Kumar, Shri K. Nachiket, Shri P. Chidambaram, Dr Ramanathan and Shri Gnanapandithan) for their continuous support, guidance and encouragement which are driving forces for my work.



**K. Sairam**

# CONTENTS

	Page No.
<b>Abstract</b>	xi
<b>List of Figures</b>	xiii
<b>List of Tables</b>	xvii
<b>List of Abbreviations</b>	xviii
<b>Chapter 1: Introduction</b>	
1.1 Background	1
1.2 Gap Areas	4
1.3 Objectives	5
1.4 Structure of the thesis	6
<b>Chapter 2: Literature Review</b>	
2.1 Crystal structure and bonding nature of boron carbide	7
2.2 Phase stability in the Boron – Carbon system	9
2.3 Boron Carbide synthesis	10
2.4 Sintering of Boron Carbide and its composites	12
2.4.1 Pressure-less sintering	14
2.4.1.1 Carbon as sinter additive	15
2.4.1.2 Role of carbide/boride additives	16
2.4.1.3 Silicon as sinter aid	17
2.4.1.4 Other additives	17
2.4.2 Hot Pressing	17
2.4.2.1 Role of sinter additives	18
2.4.3 Hot Isostatic Pressing (HIP)	19
2.4.4 Spark Plasma Sintering	20
2.4.4.1 SPS Mechanism – An unresolved mystery	22
2.4.4.2 Advantages of SPS	22
2.5 Summary of literature review and proposed investigation	23
<b>Chapter 3: Experimental Work</b>	
3.1 Starting materials	25
3.2 Characterization of starting powders	26
3.2.1 Particle size analysis	26

3.2.2	Phase confirmation of powder by XRD analysis	27
3.3	Preparation of powder mixture	27
3.4	Study of reaction mechanism	27
3.4.1	Thermogravimetric analysis of powder mixture	27
3.4.2	Powder compaction and pyro-vacuum treatment	28
3.4.3	XRD phase analysis of pyro-vacuum treated material	28
3.5	Densification techniques	28
3.5.1	Spark Plasma Sintering	28
3.5.2	Densification by hot pressing	31
3.6	Density, Phase and Microstructural analysis of Sintered Pellets	32
3.6.1	Measurement of pellet dimensions and density	32
3.6.2	Phase analysis of sintered pellets	32
3.6.3	Optical Microscopy	33
3.6.4	Scanning electron microscopy	33
3.6.5	Transmission electron microscopy	33
3.7	Evaluation of Mechanical Properties Sintered Compacts	33
3.7.1	Measurement of elastic modulus	33
3.7.2	Microhardness measurement	34
3.7.3	Measurement of fracture toughness by indentation method	34
3.7.4	Measurement of Flexural Strength	35
3.8	Evaluation of thermal conductivity of sintered samples	36
3.9	Measurement of electrical conductivity of sintered samples	37
	<b>Chapter 4: Results and Discussion: Phase evolution and reaction mechanism</b>	38
4.1	Thermal Analysis of B <sub>4</sub> C-Eu <sub>2</sub> O <sub>3</sub> System	38
4.2	Phase Assemblage of Sintered B <sub>4</sub> C-Eu <sub>2</sub> O <sub>3</sub>	41
4.3	EuB <sub>6</sub> Formation: Reaction Mechanism	44
	<b>Chapter 5: Results and Discussion: Sintering and Microstructure</b>	47
5.1	Effect of Temperature on densification of B <sub>4</sub> C	47
5.2	Effect of Holding Time on densification of B <sub>4</sub> C	52
5.3	Effect of Pulse rate on densification of B <sub>4</sub> C	53
5.4	Effect of Sinter-Aid (Eu <sub>2</sub> O <sub>3</sub> ) addition on densification of B <sub>4</sub> C	55
5.4.1	SPS Operation	55
5.4.2	Densification of B <sub>4</sub> C in the presence of Eu <sub>2</sub> O <sub>3</sub>	55

5.4.3	Microstructural development during Spark Plasma Sintering of Monolithic B <sub>4</sub> C	57
5.5	Microstructural characterization of B <sub>4</sub> C doped with Eu <sub>2</sub> O <sub>3</sub>	60
5.6	Development of Twinned Microstructures during Spark Plasma Sintering of B <sub>4</sub> C	64
5.7	Role of Twin boundaries on Pores and Second Phase Morphology	68
5.8	Correlation between Twin boundary development and SPS conditions (Formation of Twin boundaries during SPS):	73
5.9	Effect of second phase on the nature of twin structures	74
5.10	Implication of Twin boundaries on strengthening	77
5.11	Discussion on Role of Oxides as Sinter-Additive to B <sub>4</sub> C	77
5.11.1	Anomaly in the densification trend of B <sub>4</sub> C: with Eu <sub>2</sub> O <sub>3</sub> additions	77
5.12	CONCLUSIONS (Sintering and Microstructure Development)	80
	<b>Chapter 6: Results and Discussion: Mechanical &amp; Thermophysical properties</b>	82
6.1	Elastic Modulus and Hardness of monolithic B <sub>4</sub> C	82
6.2	Effect of EuB <sub>6</sub> (second phase) on Elastic Modulus and Hardness of B <sub>4</sub> C	86
6.3	Fracture toughness by indentation technique	88
6.4	Flexural Strength and Estimation of Weibull Distribution Parameters	91
6.5	Thermal transport property	102
6.6	Electrical transport property	104
6.7	CONCLUSIONS (Mechanical and Thermo-Physical Properties)	108
	<b>6.7 Conclusions</b>	109
	<b>6.8 Future Scope</b>	112
	<b>6.9 References</b>	113

## ABSTRACT

Boron carbide is one of the most important compounds of boron for nuclear reactor applications. It's ability to absorb neutrons (thermal neutron capture cross section: 760 barn) without forming long lived radio-nuclides makes the material attractive as a neutron absorber in nuclear power plants. The dense B<sub>4</sub>C-based materials can be used as a control rod material in nuclear reactors due to the presence of neutron absorbing <sup>10</sup>B isotope (19.8%) in natural boron. Other nuclear applications of boron carbide include neutron shielding and emergency shut-off pellets. However, monolithic B<sub>4</sub>C suffers significant cracking during neutron irradiation due to thermal stresses and helium gas as a result of produced by <sup>10</sup>B(n,α)<sup>7</sup>Li reaction. As a result of cracking, pellet-clad mechanical and chemical interaction occurs which causes serious deformation and failure in cladding tube or control rod sub-assembly. Low thermal conductivity of B<sub>4</sub>C is the major cause for establishing thermal gradient of the orders of 1000°C/cm during neutron irradiation. In addition, B<sub>4</sub>C is extremely susceptible to brittle failure due to the He gas release causing volumetric swelling. In the above back-drop, development of boron carbide-based composites having good thermal conductivity and improved fracture resist characteristics can be suitable for the application in advanced high temperature nuclear reactors.

In the above perspective, this thesis uncovers the densification and properties of monolithic B<sub>4</sub>C and Europium oxide (Eu<sub>2</sub>O<sub>3</sub>) added B<sub>4</sub>C material via ultra-fast sintering technique (spark plasma sintering). The densification of non-oxide ceramics has been a known challenge in the field of engineering ceramics. In the first part of the thesis, the densification behaviour of boron carbide without sinter additives is reported for temperatures in the range of 1100°C to 1800°C by spark plasma sintering (SPS) technique. Effect of sintering parameters (holding time and DC pulse rate) on densification of boron carbide is reported. Pulsed DC current is found to play a dominant role in the densification of boron

carbide and in achieving near theoretical densities at lower sintering temperature compared to conventional sintering techniques.

The amount and type of sinter-aid together with sintering conditions significantly influence the microstructure in non-oxide ceramics. In this perspective, the second part of the thesis reports the use of  $\text{Eu}_2\text{O}_3$  sinter-aid and spark plasma sintering towards the densification of  $\text{B}_4\text{C}$ . The densification is largely influenced by the solid-state reactions during heating to  $1900^\circ\text{C}$ . Based on the careful analysis of the heat-treated powder mixture ( $\text{B}_4\text{C}$ - $\text{Eu}_2\text{O}_3$ ) and sintered compacts, the competitive reaction pathways are proposed to rationalize the formation of  $\text{EuB}_6$  as dominant microstructural phase. An array of distinctive morphological features in terms of intragranular and intergranular  $\text{EuB}_6$  phase as well as characteristic defect structures (asymmetric twins, stacking faults and threaded dislocations) are observed within dense  $\text{B}_4\text{C}$  matrix. An attempt has been made to explain the competition between microstructure development and densification. The developed materials were investigated for mechanical, thermal and electrical properties. The presence of second phase leads to decreased resistance for the heat flow through the components and their interfaces, thereby contributes for enhanced thermal conduction in  $\text{B}_4\text{C}$ - $\text{EuB}_6$  composite. Bi-polaron hopping and Percolation-tunneling mechanisms are the active current conduction mechanisms identified, in-case of monolithic  $\text{B}_4\text{C}$  and  $\text{B}_4\text{C}$ - $\text{EuB}_6$  composites. The enhanced electrical conductivity would facilitate the fabrication  $\text{B}_4\text{C}$  compacts by electric-discharge machining. The synergistic effects of cleavage faceting, interface debonding, crack branching together contributes towards realization of enhanced flexural strength in the developed  $\text{B}_4\text{C}$ - $\text{EuB}_6$  composite. Thus,  $\text{B}_4\text{C}$ - $\text{EuB}_6$  composite exhibited superior fracture strength, thermal and electrical properties in comparison with monolithic  $\text{B}_4\text{C}$  without deteriorating the neutron absorption characteristics of the material, which conclusively establish the potential of  $\text{B}_4\text{C}$  with predominant presence of  $\text{EuB}_6$  phase as next generation materials for high temperature nuclear reactors.

# LIST OF FIGURES

Fig. 1 Overall research structure of this thesis .....	06
Fig 2.1 Rhombohedral unit cell structure of B <sub>4</sub> C .....	07
Fig. 2.2 Boron carbide lattice showing correlation between the rhombohedral (red) and the hexagonal (blue) unit cells.....	08
Fig. 2.3 Boron - Carbon Phase Diagram .....	09
Fig. 3.1 Schematic of Spark Plasma Sintering (SPS) Facility showing the location of temperature measurement by optical pyrometer .....	29
Fig. 3.2 Schematic of Pulsed DC waveform showing 5-5 (ms-ms) pulse sequence during the holding period .....	30
Fig. 4.1(a) TG-DTA plots obtained for B <sub>4</sub> C-10vol.% Eu <sub>2</sub> O <sub>3</sub> composite mixture, (b) derivative plots of the TG-DTA data .....	39
Fig. 4.2 X-ray diffraction patterns of (a) B <sub>4</sub> C powder (for comparison) and B <sub>4</sub> C-10vol.% Eu <sub>2</sub> O <sub>3</sub> composite mixture heat treated in vacuum at different temperatures (b) 1100°C, (c) 1500°C, (d) 1900°C (with no dwell time).....	40
Fig 4.3(i) X-ray diffraction patterns of (a) Eu <sub>2</sub> O <sub>3</sub> powder, (b) B <sub>4</sub> C powder, (c) sintered monolithic B <sub>4</sub> C, (d) sintered B <sub>4</sub> C-5vol.%Eu <sub>2</sub> O <sub>3</sub> composite and (e) sintered B <sub>4</sub> C-10vol.% Eu <sub>2</sub> O <sub>3</sub> composite. All the samples are sintered in vacuum at 1900°C for 15 minutes using SPS route .....	42
Fig 4.3(ii) X-ray diffraction peaks corresponds to (104) plane of B <sub>4</sub> C phase to illustrate peak shift in B <sub>4</sub> C-5vol.% Eu <sub>2</sub> O <sub>3</sub> and B <sub>4</sub> C-10vol.% Eu <sub>2</sub> O <sub>3</sub> composite towards higher angle with respect to the monolithic B <sub>4</sub> C .....	43
Fig. 5.1 Relative density and Shrinkage of Spark Plasma Sintered B <sub>4</sub> C samples as a function of Processing Temperatures .....	48
Fig. 5.2 Ram displacement observed at different processing temperatures is plotted as a function of SPS operation sequence (Holding Period and Cooling). *Note that these curves do not represent the path of displacement; it is plotted by considering the initial and end position of Ram at different temperatures with respect to operation sequence.....	51

Fig. 5.3 Relative density and shrinkage of B <sub>4</sub> C sintered at 1800°C at different holding period (5, 10 and 15 min).....	53
Fig. 5.4 Variation of Relative Density of Sintered B <sub>4</sub> C compacts at 1600°C as a function of DC Pulse Rate .....	54
Fig. 5.5 XRD of starting B <sub>4</sub> C powder and SPS processed full dense B <sub>4</sub> C pellet.....	56
Fig. 5.6 Scanning Electron Micrograph of fully dense B <sub>4</sub> C compact processed at 1800°C for 15 min showing partially melted structures (indicated by arrow marks) and also reveals the presence of twin structures .....	57
Fig. 5.7 (a) Scanning Electron Micrographs of B <sub>4</sub> C processed at 1400°C shows open porosities and neck-like regions between the particles and (b) Micrograph of B <sub>4</sub> C processed at 1600°C indicates discrete densified regions with interconnected porosities.....	58
Fig. 5.8 Secondary electron micrographs of spark plasma sintered B <sub>4</sub> C-18 vol.%EuB <sub>6</sub> composite. Highlighted portion indicates the distribution of submicron pores within the matrix grains .....	60
Fig. 5.9 (a-e) Scanning transmission electron microstructures of B <sub>4</sub> C-EuB <sub>6</sub> composites showing EuB <sub>6</sub> particles at (a) intragranular and (e) intergranular locations as indicated by arrow marks. EDS Spectra (b) and (c) were recorded at centre and peripheral regions, respectively of intragranular EuB <sub>6</sub> particle. EDS Spectrum (d) was obtained at B <sub>4</sub> C matrix grain .....	61-63
Fig. 5.10 (a) Optical microstructures of fully dense B <sub>4</sub> C (15 min) and b) 96.6% dense B <sub>4</sub> C compact sintered at 1800°C (10 min) showing the presence of twin boundaries.....	64
Fig. 5.11 Scanning Electron Micrograph of 96.6% dense B <sub>4</sub> C fractured surface showing transgranular mode of fracture and also the presence of twin boundaries (indicated by arrow marks).....	65

Fig. 5.12 BF-TEM micrographs of B <sub>4</sub> C-18 vol.%EuB <sub>6</sub> composite indicating the presence of (a) threaded dislocations and (b) stacking fault regions .....	67
Fig. 5.13(a-c) FESEM microstructures of B <sub>4</sub> C-18vol.%EuB <sub>6</sub> composite shows the distribution of EuB <sub>6</sub> particles and submicron pores having different morphologies at the intragranular locations of B <sub>4</sub> C .....	68
Fig. 5.14 BF-TEM micrographs showing distribution of (a) spheroidal intragranular EuB <sub>6</sub> particles and (b) pores in twin-free regions.....	69-70
Fig. 5.15 BF-TEM micrographs showing distribution of lath shaped and aligned (a) intragranular EuB <sub>6</sub> particles (arrow marks) and (b) pores in twinned regions .....	71-72
Fig. 5.16 (a) STEM image and (b) BF-TEM image of B <sub>4</sub> C-18 vol.%EuB <sub>6</sub> composite showing the presence of twinned structures in matrix grains.(c) SAED pattern obtained from twin boundary region of B <sub>4</sub> C phase (highlighted as dotted rectangular region in (b) .....	75-76
Fig. 6.1 Elastic Modulus and Hardness of Spark Plasma Sintered B <sub>4</sub> C compacts plotted as a function of relative density .....	85
Fig. 6.2 Elastic Modulus and Hardness of B <sub>4</sub> C compact sintered at 1800°C with different holding periods (5,10 and 15 min.) is plotted with respect to its sample density obtained .....	86
Fig. 6.3 Typical load vs. displacement plot recorded while performing hardness test instrumented on hot pressed B <sub>4</sub> C-10% Eu <sub>2</sub> O <sub>3</sub> samples .....	88
Fig. 6.4 Optical micrographs showing the crack propagation patterns of fully dense B <sub>4</sub> C samples after indentation fracture.....	89
Fig. 6.5 Strength reliability analysis for monolithic B <sub>4</sub> C (0% Eu <sub>2</sub> O <sub>3</sub> ) and B <sub>4</sub> C (10% Eu <sub>2</sub> O <sub>3</sub> ) based on three point flexural strength and weakest link fracture statistics ( $\sigma$ in MPa) .....	93-94
Fig. 6.6 Macroscopic fracture surface of monolithic B <sub>4</sub> C showing fracture planes at 45° angles.....	95

Fig. 6.7(a-e) SEM images showing fracture surfaces of B <sub>4</sub> C-10 vol.% Eu <sub>2</sub> O <sub>3</sub> composite .....	96-97
Fig. 6.8(a-d) showing the crack propagation path experiencing crack deflections, crack branching and interface debonding .....	99-101
Fig. 6.9 Thermal conductivity of monolithic B <sub>4</sub> C and B <sub>4</sub> C-18 vol.% EuB <sub>6</sub> .....	103
Fig. 6.10 Variation of electrical conductivity with respect to temperature (a) monolithic B <sub>4</sub> C and (b) B <sub>4</sub> C-EuB <sub>6</sub> composite .....	105
Fig. 6.11(a-b) Arrhenius plot of electrical conductivity for (a) monolithic B <sub>4</sub> C and (b) B <sub>4</sub> C-EuB <sub>6</sub> composite .....	106

## LIST OF TABLES

Table 2.1 Comparison of different boron carbide synthesis methods.....	11
Table 3.1 Chemical assay of B <sub>4</sub> C powder used in the experiments.....	25
Table 3.2 Typical particle size distribution of starting materials used in the experiments .....	26
Table 4.1 Summary of phase assemblage in B <sub>4</sub> C-Eu <sub>2</sub> O <sub>3</sub> composite samples processed under different conditions.....	41
Table 4.2 Phase assemblage of Spark Plasma Sintered B <sub>4</sub> C-Eu <sub>2</sub> O <sub>3</sub> composite samples.....	43
Table 5.1(a) Processing conditions and Mechanical properties of spark plasma sintered monolithic boron carbide .....	49
Table 5.1(b) Influence of pulse rate on densification of boron carbide .....	50
Table 6.1 Density, Elastic modulus and Hardness of monolithic B <sub>4</sub> C sintered under different parameters.....	83
Table 6.2 Calculated shape factors of the pores developed under different processing condition of monolithic B <sub>4</sub> C .....	83
Table 6.3 Elastic Modulus and Hardness of sintered B <sub>4</sub> C and B <sub>4</sub> C-EuB <sub>6</sub> .....	87
Table 6.4 Indentation fracture toughness of B <sub>4</sub> C composites processed under different conditions .....	90
Table 6.5 Flexural strength of hot pressed B <sub>4</sub> C composites measured using 3 point bending test .....	94
Table 6.6 Thermal neutron absorption cross-section of B <sub>4</sub> C-EuB <sub>6</sub> composites.....	107

## LIST OF ABBREVIATIONS

SPS	Spark Plasma Sintering
HP	Hot Pressing
HIP	Hot Isostatic Pressing
PLS	Pressureless Sintering
PPC	Plasma Pressure Compaction
EPAC	Electric Pulse Assisted Consolidation
FAST	Field Assisted Sintering Technique
PECS	Pulsed Electric Current Sintering
DC	Direct Current
TG-DTA	Thermogravimetry – Differential Thermal Analysis
XRD	X-ray diffraction
SEM	Scanning Electron Microscope
TEM	Transmission Electron Microscope
FESEM	Field Emission Scanning Electron Microscope
STEM	Scanning Transmission Electron Microscope
SAED	Selected Area Electron Diffraction
EDS	Energy Dispersive Spectrometer
BF	Bright Field Image
BSE	Back Scattered Electron
SEI	Secondary Electron Imaging
CER-CER	Ceramic-Ceramic
CER-MET	Ceramic-Metal
EDM	Electric Discharge Machining
ASTM	American Society for Testing and Materials

---

# Chapter 1: Introduction

---

## 1.1 Background

Boron carbide, a covalently bonded monolithic ceramic is a potential candidate for high-performance engineering applications due to its unique combination of properties such as low density ( $2.52 \text{ g.cm}^{-3}$ ), high hardness (37 GPa), high melting temperature (2450 °C), high elastic modulus (450 GPa), chemical inertness, high neutron absorption cross-section (600 barns) and excellent thermoelectric properties. Boron carbide is the third hardest material after diamond and cubic boron nitride. It has found application in the form of powder, sintered product as well as thin films. In powder form, it's been used for lapping, polishing and water jet cutting of metals and ceramic materials. The combination of low specific weight, high hardness and impact resistance makes it a chosen material for ballistic armour applications. Being a high temperature ceramic, it caters to the demands of highly aggressive industrial and laboratory environments. As a strategic material, it finds application as control rod, shielding material and as neutron detector in nuclear reactors due to the presence of  $\text{B}^{10}$  strong neutron absorbing isotope. Boron carbide based composites having good thermal conductivity and thermal shock resistance are reported to be suitable first wall nuclear fusion reactor material as well as potential inert matrix material for nuclear waste disposal purposes (particularly actinide burning). P-type semiconducting property of boron carbide makes it qualifiable for high temperature tolerable electronic devices. The low density, low thermal expansion and high stiffness characteristics of  $\text{B}_4\text{C}$  make it a potential candidate to replace Be based components in aerospace industries.<sup>[1-3]</sup>

Although boron carbide ( $B_4C$ ) has attractive properties, its application is rather limited, due to the difficulties in densification, extreme brittleness and poor oxidation resistance beyond  $600^\circ C$ . The densification of  $B_4C$  is complicated due to its high melting temperature, low self-diffusion coefficient and presence of surface oxide layers. Prevalence of high degree of covalency in  $B_4C$  necessitates high sintering temperatures close to the melting point for achieving complete densification of  $B_4C$ .<sup>[1,4-6]</sup> This high sintering temperature in turn results in grain coarsening and residual porosities that deteriorate the material's performance.<sup>[4-6]</sup> Boron carbide with densities greater than 93% is reportedly achieved at temperatures above  $2000^\circ C$ , by grain boundary and volume diffusion assisted mechanisms. At temperatures greater than  $2000^\circ C$ , the dominance of surface diffusion and evaporation condensation processes synergistically results in mass transfer without densification and contributes for exaggerated grain growth and results in poor mechanical properties of  $B_4C$ .<sup>[6-8]</sup> In the field of sintered materials, performances are majorly influenced by high densities, absence of defects, and with the retention of fine grain microstructures. Pressureless sintering method to get high dense boron carbide had proved to be difficult. Under these circumstances, several attempts have been made to develop high dense compacts by pressure-assisted compaction techniques like hot-pressing (HP) or hot-isostatic pressing (HIP) with and without addition of sintering aids.<sup>[1-2, 9-18]</sup> The pressure was recognized to promote the densification by facilitating particle rearrangement, plastic deformation and pore elimination. Though the near theoretical dense compacts can be obtained by both HP and HIP techniques, their ability to retain fine grain microstructures is rather limited, owing to the necessity of longer densification period during which grain growth and densification kinetics competes with each other. Processing  $B_4C$  in the presence of sinter-aid additions are reported to lower the consolidation temperatures and thus helps in consolidating product with reduced grain coarsening effects, but at the expense of purity of final product. Purity is the primary concern specifically in nuclear industries.

Because any presence of secondary elements affects the neutron absorption characteristics of the material <sup>[1-2, 17]</sup> Thus, there is a need of new sintering techniques which would alleviate the sintering conditions for attaining high dense and fine grain B<sub>4</sub>C ceramics without the need of sinter additions. <sup>[19-24]</sup>

Continuous research on boron carbide-based ceramics has proven that suitable second phase addition helps in achieving improved sintering behavior and mechanical properties. The selection of suitable sinter additive is of primary importance for nuclear applications, where purity is a concern as stated in preceding para. <sup>[1-2]</sup> Additions of carbon and carbon based compounds (SiC, Be<sub>2</sub>C and TiC) activates sintering kinetics by deoxidizing the powder surface. <sup>[25-29]</sup> It is reported that increased boron content in B<sub>4</sub>C also facilitates the sintering with considerable improvement in fracture toughness. <sup>[30]</sup> Metallic additives (such as Fe and Cu) facilitate the liquid phase sintering and thus help in achieving dense bodies at lower sintering temperatures. <sup>[31-32]</sup> However, it is detrimental to the unique properties of the hard ceramics. Addition of AlN and BN to B<sub>4</sub>C imparts excellent impact resistance and machinability respectively. <sup>[33-34]</sup>

Oxide are particularly interesting as sintering aid additions due to the chemical instability nature of B<sub>4</sub>C with respect to different oxide systems. <sup>[35]</sup> Since the work by Skorokhod et al. <sup>[36]</sup>, there have been considerable research efforts are invested towards the use of different oxide systems as sinter additives to B<sub>4</sub>C. <sup>[1, 10, 12-15, 37-39]</sup> The resulting chemical reactions during sintering forms *in situ* non-volatile carbides/borides compounds as reinforcement phase in ceramic matrix, this results in CER-CER composites. <sup>[6]</sup> Attempts made on the development of B<sub>4</sub>C-MeB<sub>2</sub> composites through in situ reaction of B<sub>4</sub>C with MeO (Me= Ti, Zr, Cr, V, and Y) yielded high dense B<sub>4</sub>C composites with improved mechanical properties as compared with monolithic boron carbide. It is reported that TiO<sub>2</sub> addition to B<sub>4</sub>C for in situ synthesis of TiB<sub>2</sub> appears to be more effective than merely elemental Ti addition and the

difference is explained based on the formation of sub-stoichiometric  $B_4C$  with the former case. This sub-stoichiometric compound is believed to enhance the mobility of the constituents which result in higher sinterability. <sup>[10]</sup> Combined addition of  $TiO_2$  and carbon to  $B_4C$  resulted in in-situ formation of  $TiB_2$ , where carbon acted as a reducing agent for  $TiO_2$ . The addition of  $B_4C$  and C to  $ZrB_2$ , effectively removes surface oxide impurities ( $ZrO_2$  and  $B_2O_3$ ) and inhibits grain growth, thus contributes for enhanced densification. Such ceramics exhibit fine grain microstructures and superior mechanical properties, when compared to monolithic boron carbide. <sup>[39]</sup>

## 1.2 Gap Areas

Till date, most of the oxides, investigated as additives are based on transition metal oxides ( $TiO_2$ ,  $ZrO_2$ ,  $HfO_2$ ,  $V_2O_5$ ). <sup>[12-15, 17-18, 36-37, 40-42]</sup> It is worthwhile to mention that almost all the transition metal oxides, used as sinter additives to  $B_4C$ , result in enhanced densification. On the other hand, sintering experiments of boron carbide using rare earth oxide as sinter-aid are rather limited. Goldstein et al. <sup>[15]</sup> developed high dense  $B_4C$  compacts ( $>95\% \rho_{th}$ ) by pressureless sintering at  $2180^\circ C$  with the addition of transition metal oxides and rare earth metal oxides. The results indicated that the role of rare earth oxides ( $La_2O_3$  and  $Y_2O_3$ ) as sinter-aids is much more effective, when compared to transition metal oxides. On contrary, Wei et al. <sup>[43]</sup> reported the lack of densification with only rare earth metal oxide (especially  $Eu_2O_3$  and  $Sm_2O_3$ ) as sinter-aid to  $B_4C$ . However, when  $B_4C$  was added to the composite mixture of both rare earth oxide and phenolic resin, the resultant compact exhibited improved sinterability. <sup>[43]</sup> The reason for decreased sintering aptitude of  $B_4C$  in the presence of only rare earth oxide addition ( $Eu_2O_3$  and  $Sm_2O_3$ ) is not yet clearly understood.

In the above backdrop, it is worth to probe into the influence of rare earth oxide as sinter-aid to  $B_4C$ . In addition to the above-mentioned perspective on sinterability aspect, the

combination of rare earth containing compound(s) to boron carbide is expected to provide superior neutron absorption characteristics and have potential for application as high temperature neutron absorber material. High neutron absorption cross sections of boron (759 barns) and europium (4600 barns) and ability of  $\text{EuB}_6$  structure to accommodate helium atoms (forms as a result of neutron irradiation reaction) make this compound useful for control rod application in nuclear reactors. <sup>[1-2, 44-45]</sup> In addition, borides of rare earth metals have attracted attention due to their unique combination of physiochemical and thermo-mechanical properties especially at elevated temperatures. These borides are characterized by high melting point, hardness, electrical and thermal conductivities, excellent thermal stability, low vapor pressure and thermal expansion coefficient. <sup>[1-5, 45-49]</sup>

### **1.3 Objectives**

The following objectives have been set in the present study.

1. To study the effect of rare earth oxide ( $\text{Eu}_2\text{O}_3$ ) addition on phase evolution and final phase assemblage of the sintered product.
2. To study the mechanism of chemical reactions that take place during sintering.
3. To understand and establish the influence of spark plasma sintering process parameters on the densification behavior and microstructure development of boron carbide
4. To probe the role of rare earth oxide ( $\text{Eu}_2\text{O}_3$ ) as sinter-aid to boron carbide
5. Comparison between the sintering behaviour with tetravalent oxide addition and with rare earth oxide ( $\text{Eu}_2\text{O}_3$ ) addition.
6. To study the effect of rare earth oxide ( $\text{Eu}_2\text{O}_3$ ) addition on mechanical and thermo-physical properties of  $\text{B}_4\text{C}$ .

## 1.4 Structure of the thesis

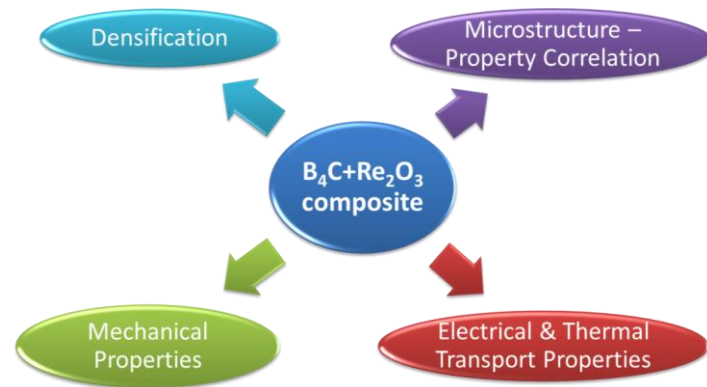


Fig. 1 Overall research structure of this thesis.

Following various objectives, some schematic illustration demonstrating the summary of thesis work is presented in Fig.1. The thesis has been divided into seven chapters, which are further classified into sub-chapters and sections, as and when appropriate. In the present Chapter of the thesis, a comprehensive introduction to the subject has been given. The Chapter outlines technological importance of the material, justification for carrying out the work, statement of the objectives and scope of the work.

In Chapter 2, a review on the existing literature relevant to the present work has been presented. This chapter contains the brief reviews on crystal structure and phase stability, sintering phenomenon. The experimental techniques and methodologies employed in the present study are described in Chapter 3. Results have been compiled in Chapter 4 to 6 and discussed. Chapter 4 has been subdivided into sub-sections explaining phase evolution and reaction mechanism between  $B_4C$  and  $Eu_2O_3$  mixture. Chapter 5 focused on densification behaviour of  $B_4C$  and  $B_4C$  added with  $Eu_2O_3$  by spark plasma sintering and its corresponding microstructure development. Chapter 6 describes the mechanical properties and thermo-physical properties of developed  $B_4C$  composites. Conclusions drawn from above studies are discussed in Chapter 7.

---

## Chapter 2: Literature Review

---

### 2.1 Crystal Structure and nature of bonding in Boron Carbide

Widely accepted crystal structure of boron carbide is rhombohedral, having 12-atom icosahedra located at the corners of the unit cell. The centres of these icosahedra are located on each of the corners of the rhombohedral lattice and connected by 3 atom chain along the diagonal of the rhombohedra, as seen in Fig.2.1. <sup>[1-3]</sup> A rhombohedron axes is a geometrical pattern with equal length and axial angles, while an icosahedron is a polyhedron having twenty faces, twelve equivalent vertices and various planes of symmetry. The twelve atoms of the icosahedra and the three interconnecting atoms together form a fifteen-atom cell belonging to  $D_{3d}-R\bar{3}m$  space group. <sup>[1-3]</sup>

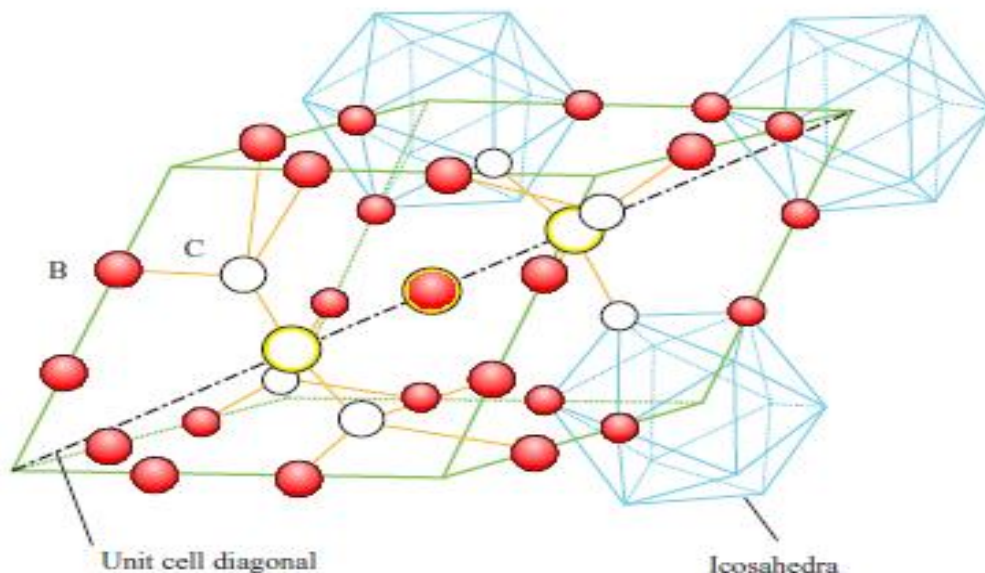


**Fig. 2.1: Rhombohedral unit cell structure of  $B_4C$**  <sup>[1,3]</sup>

Four types of atomic bonds identified for boron carbide in the  $R3m$  symmetry (Fig. 2.2): (i) the intrachain bond that connects the end atom and the centre atom in the 3-atom chain exhibits  $\pi$  character; (ii) the chain-icosahedron bond connecting the end atom in the 3-atom chain to an atom in equatorial site of the icosahedra; (iii) the intericosahedral bonds connects atoms in the polar sites of neighboring icosahedra and (iv) the intraicosahedral bonds connects atoms within the icosahedron.

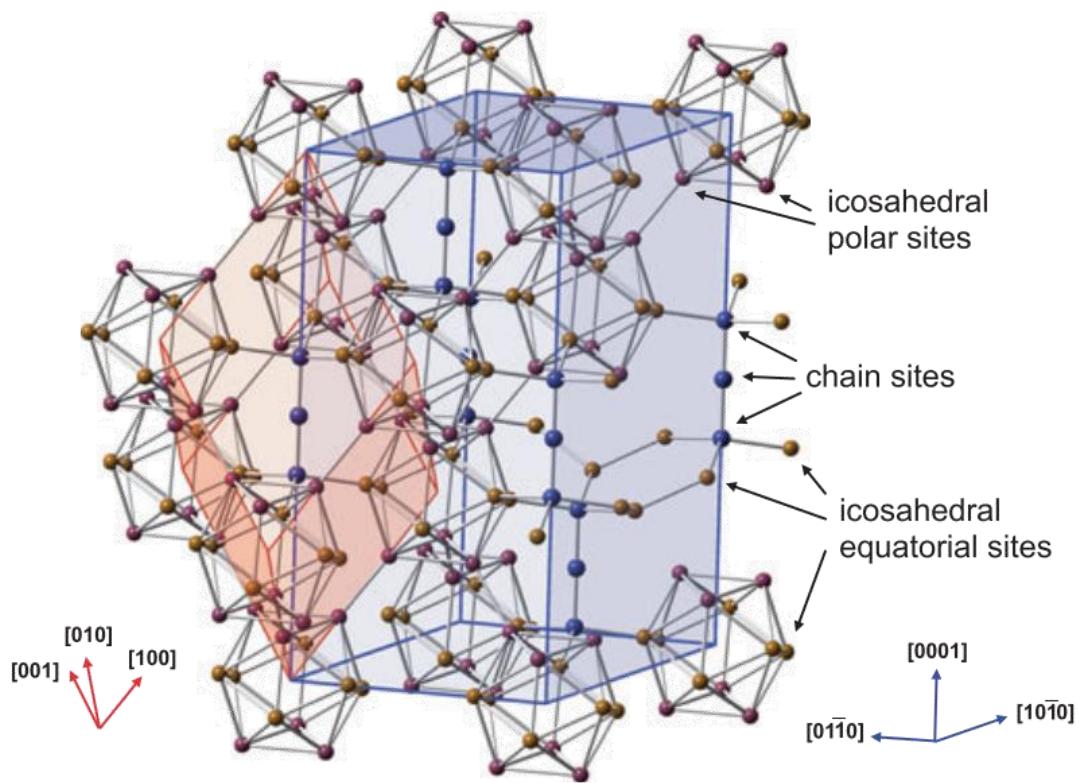


**Fig. 2.2: Boron carbide lattice showing correlation between the rhombohedral (red) and the hexagonal (blue) unit cells.<sup>[1-3]</sup>**

## 2.2 Phase Stability in the Boron – Carbon system

Boron carbide is a compositionally disordered material with rhombohedral structure in wide range of composition, which extends from  $B_{10.4}C$  (8.8at.%C) to  $B_4C$  (20 at.%C) (Fig 2.3). [1,3,50-55]  $B_4C$  is in equilibrium with free carbon and is the only boundary between  $B_nC$  and  $B_nC+C$  (where  $4 < n < 10$ ), synthesis of  $B_4C$  without free carbon is a great challenge. The percentage of carbon in boron carbide greatly influences the structure and properties of the compound and hence the exact information about B/C ratio of the phase is very important. The number of carbon atoms that are able to be incorporated into the icosahedra is limited to a maximum of two atoms due to bonding constraints.

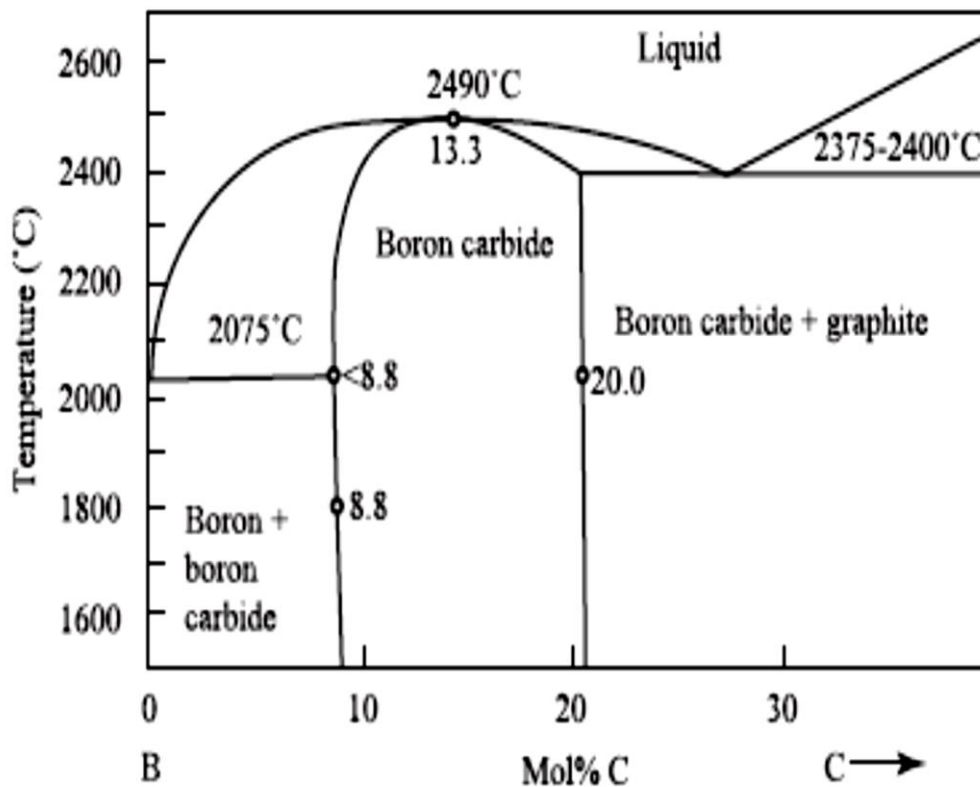


Fig. 2.3: Boron - Carbon Phase Diagram

Because of the ability of carbon atoms to hybridize into the  $sp^3$  orbital, a carbon atom occupies both ends of the three-atom inter-icosahedra chain with the central boron atom, arranging to form C-B-C chain. However, singly ionized carbon atoms have occasionally been detected at the centre. Depending on the carbon concentration, boron preferentially substitutes for carbon in the three-atom inter-icosahedra chains and resulting in conversion from C-B-C chains to C-B-B chains. The most widely accepted boron carbide crystal structural model possesses  $B_{11}C$  icosahedra with C-B-C inter-icosahedral chains. The boron icosahedron is deficient in electrons and requires addition of two more electrons for the crystal to acquire a thermodynamically favourable closed-shell structure. These additional electrons are provided by substitution of carbon atoms. The bonds between the boron and carbon atoms in  $B_4C$  are essentially covalent in nature. However, because of the differences in electro negativity for boron and carbon, a partial ionic bond also occurs. <sup>[1-3]</sup>

### **2.3 Boron Carbide synthesis**

Boron carbide was discovered as a by-product in nineteenth century for a reaction involving metal borides. Almost 75% pure boron carbide material was produced during initial investigations. In 1933, Ridgway <sup>[46]</sup> reported the production of crystalline  $B_4C$  of 90% purity by adopting carbothermic process. Lipp <sup>[57]</sup> has presented a review of boron carbide production, properties and applications in 1965. Spohn <sup>[58]</sup> has also mentioned the synthesis routes for boron carbide production and its uses in his article. Comparison of different methods of synthesizing boron carbide is tabulated (Table 2.1). <sup>[2, 59-99]</sup>

**Table 2.1 (Reprinted with permission from publisher) Comparison of different boron carbide synthesis methods** [2, 59-99]

Method	Boron source	Carbon source	Advantage	Disadvantage
Carbothermic reduction	H <sub>3</sub> BO <sub>3</sub> or B <sub>2</sub> O <sub>3</sub>	PC, graphite, activated carbon	Cheap raw material, suitable for commercial production	High boron losses, obtained in lump form, need grinding for powder, production [56-63]
Magnesiothermic reduction	B <sub>2</sub> O <sub>3</sub> or Na <sub>2</sub> B <sub>4</sub> O <sub>7</sub>	PC, graphite, activated carbon	Fine powder, exothermic reaction, suitable for SHS process	Product contaminated with Mg, MgB <sub>2</sub> [64-69]
Synthesis from elements	Boron	PC, graphite, activated carbon	No loss of boron, good control over purity and carbon content of product	High cost of elemental boron [70-74]
Vapour phase synthesis	BCl <sub>3</sub> , BBr <sub>3</sub> , BI <sub>3</sub> , B <sub>6</sub> H <sub>6</sub> , B <sub>2</sub> O <sub>3</sub>	CH <sub>4</sub> , C <sub>2</sub> H <sub>4</sub> , C <sub>2</sub> H <sub>6</sub> , C <sub>2</sub> H <sub>2</sub> , CCl <sub>4</sub>	Suitable for thin films, fine powder, fibers, whiskers	Difficult to produce B <sub>4</sub> C powder suitable for densification, not amenable for large scale production [75-83]
Synthesis from polymer precursors	Boric acid, B <sub>2</sub> O <sub>3</sub> , polyvinyl pentaborane, polyvinyl borate, ethyl decaborane	Polyvinyl alcohol, citric acid, hydroxyl benzyl alcohol, sugar, ethylene glycol	Low temperature process	High free carbon content still in laboratory stage [84-91]
Liquid phase reaction	BBr <sub>3</sub> , boron	CCl <sub>4</sub>	Low temperature process, suitable for nanoparticles	Need of reactive metal such as Na or Li, new method of synthesis [92-93]
Ion beam synthesis	Boron	Carbon	Suitable for B <sub>x</sub> C	Only for thin films, of academic interest only [94-95]
Vapour liquid solid growth	B <sub>2</sub> O <sub>3</sub>	Carbon black	Suitable for whisker	Need of molten metal catalyst, of academic interest only [96-99]

\*PC: petroleum coke; SHS: self-propagating high temperature synthesis.

Synthesis of boron carbide from its elements is considered uneconomical due to the high cost of elemental boron and hence employed for specialised applications [100] only, such as B<sup>10</sup> enriched or very pure boron carbide. For (B<sup>10</sup>) enriched boron carbide, carbothermic reduction is not a preferential method as it involves the loss of boron during the operation. Although formation of boron carbide from its elements is thermodynamically feasible at room temperature, the heat of reaction (-39 kJ mol<sup>-1</sup>) is not sufficient to conduct self-sustaining reaction. [101] Formation of boron carbide layer slows down further reaction, due to slow diffusion of reacting species through this layer, thus necessitating high temperature and longer duration for complete conversion of the elements into the compound. The elemental synthesis method involves the mixing of boron and carbon powders, which is then cold pressed and subsequently heat treated at temperatures above 1500°C in vacuum or inert atmospheres. The partially sintered pellet of boron carbide is then crushed and ground to get

fine B<sub>4</sub>C powder. To achieve a high purity product of B<sub>4</sub>C, high purity elemental boron powder produced by fused salt electrolytic process <sup>[102-103]</sup> is often used. Though the cost of production is high due to the high cost of elemental boron, for specialised applications such as in nuclear industry, this method is preferred.

## **2.4 Sintering of Boron Carbide and its composites**

Sintering is an art, having an origin dated back to thousands of years. Early development of bricks by heating clay bodies in an open pit fire is one of the finest examples of sintering practiced adopted by ancient civilizations of Mesopotamia (6000 BC). <sup>[104]</sup> The ancient Egyptians sintered metals and ceramics (3000 BC) and the Incas of South America fabricated gold-platinum jewellery using sintering.

The major products fabricated from sintering had their origins in empirical discoveries and grew to widespread use without a fundamental understanding. Sintering as a solid-state science gained traction in the late 1940s. The basic mass transport mechanism driving the densification process were subsequently investigated and documented by Frenkel, Kuczynski, Lenel, Coble, Kingery, German, and others. <sup>[105-109]</sup>

Parameters that influence the sintering process includes powder characteristics (morphology, dimension of the grains, purity, etc.), treatment (temperature, pressure, holding time) and atmosphere (vacuum, reducing, oxidizing or inert). The sintering process of the solid sample is considered to be thermodynamically irreversible. It is driven primarily by the reduction in the surface energy (free surface of the grains, then surfaces of the open and closed pores).

Three major events involved in the sintering process are as follows:

- Point contact between the particles which subsequently establishes the zone of connection between grains, causing bridge or neck like regions. This neck forms as a result of activation of sintering mechanisms such as evaporation-condensation, plastic deformation, etc., and process freezes, when the neck size reaches close to 50% of the grain radii.
- During intermediate step, residual pores gets eliminated, the size of which is directly related to the surface energy. Almost 90% compact density is achievable.
- The final step corresponds to near complete removal of the porosities contributing to near theoretical dense material.

The densification of boron carbide ceramic has always been a challenge due to the high melting point, high degree of covalency and low intrinsic self-diffusivity. <sup>[1-3]</sup> In addition, boride carbide particles tend to exhibit surface oxides ( $B_2O_3$ ) that hinders the densification process by preventing the direct contact between boron carbide particles. <sup>[2, 5-6]</sup> Moreover, these surface oxides facilitate the non-densifying mechanisms such as, surface diffusion and evaporation condensation mechanisms. Hence, the pressureless sintering operation necessitates higher sintering temperatures close to the melting temperature ( $>0.9T_{mp}$ ) of boron carbide in order to high dense compacts. Processing at such high temperatures results in exaggerated grain growth and entrapped porosities, which results in the deterioration of mechanical properties of the boron carbide. Densification of boron carbide is achieved only at temperatures  $>2000^\circ C$ , by the activation of grain boundary and volume diffusion mechanisms. <sup>[1-2, 4-8]</sup>

These setbacks have provided the driver for considerable research efforts to improve the sinterability of boron carbide by different strategies, like use of sub-micron sized starting powders, sinter additives, pressure assisted sintering techniques (like hot pressing, hot isostatic pressing) and by ultra-fast sintering techniques (like spark plasma sintering and flash

sintering). Among them, sinter-aid additions is reported to accelerate densification process or facilitate densification at relatively lower sintering temperatures by (i) forming liquid phase at sintering temperatures (liquid phase sintering), (ii) activating particle surfaces by reducing surface oxides and (iii) creation of structural defects in  $B_4C$  (reaction sintering). [2, 17] Different types of additives have been exploited to improve the sinterability and properties of these borides. Sinter additives can be broadly classified into metallic (e.g. Ni, Fe, Cu, Co, Ti) and non-metallic (oxides, silicides, carbides, nitrides and borides). The selection of sinter additive is also very important as these additives influences the high temperature properties of the material. In the following sections, some case studies on densification of boron carbide by various methods are presented.

#### **2.4.1 Pressure-less sintering**

Pressureless sintering is simple and economical operation to fabricate near net shapes components. This sintering process involves (1) fabrication of green compacts by cold compaction so as to have sufficient handling strength for ceramic samples and (2) heat treatment or sintering of green pellets at the set temperatures in controlled atmospheres. Heating can be done in an induction furnace or resistance heating furnace types. Pressureless sintering operation eliminates any machining operations as it directly results in near-finished components. However, it is extremely difficult to fabricate high dense shapes of boron carbide and other high temperature boride phases by pressureless sintering due to low self-diffusivity of these ceramics and other cited reason given in the above section 2.3.

Sintering of  $B_4C$  powder compacts is commonly performed in an inert gas or vacuum conditions. But the processing in vacuum condition helps in the evaporation of the surface oxide layer and also prevents further oxidation, there by promote the sintering mechanisms.

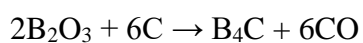
Removal of the oxide layer by heating in a reducing atmosphere before sintering also has a similar effect.

Dole et al. and others <sup>[4-8]</sup> reported highly coarsened microstructures in undoped B<sub>4</sub>C after sintering at 2000°C, whereas carbon-doped samples relatively exhibited reduced grain coarsening effects. B<sub>2</sub>O<sub>3</sub> in starting B<sub>4</sub>C powder is reported to act as a diffusion path along the surface and facilitated the particle coarsening. Lee et al. <sup>[7]</sup> have observed the onset of densification at 1800°C, rapid increase in densification 1870–2010°C and a slow-down in densification rate 2010–2140°C. The surge in densification 1870–2010°C is attributed to the presence of oxide layer which helps in precipitation of B<sub>4</sub>C through liquid B<sub>2</sub>O<sub>3</sub> or due to evaporation and condensation of rapidly evolving oxide gases (BO and CO). Slower densification at temperatures above 2010°C is attributed to evaporation and condensation of B<sub>4</sub>C. Subramanian et al. achieved only 93% density for boron carbide by sintering at 2275°C for 2h. <sup>[13]</sup> Such compacts were reported to have an average grain size in the range of 50µm possessing poor flexural strength.

#### **2.4.1.1 Carbon as sinter additive**

Various sinter additives have been reported to assist the densification process with controlled grain growth and improve mechanical properties of boron carbide. Addition of Carbon was found to be effective in promoting densification of B<sub>4</sub>C, by activating the particle surface through reduction of B<sub>2</sub>O<sub>3</sub> by Carbon. <sup>[25]</sup>

The basic chemical reaction occurs between carbon particle and surface oxide is



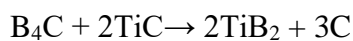
The removal of oxide layer allows direct contact between the B<sub>4</sub>C particles. Different forms of carbon such as petroleum coke, carbon black, graphite, glucose and phenolic resin have been tested as sintering aid. B<sub>4</sub>C was reported to exhibit sinter density of 98%TD with 2μm grain size by the addition of 3% C in the form of phenolic resin. Phenolic resin as carbon addition is found to be effective as compared with carbon black and glucose. <sup>[110]</sup>

#### **2.4.1.2 Role of carbide/boride additives**

Addition of carbides and borides to B<sub>4</sub>C was reported to enhance the sinter density of boron carbide. In addition, the presence of borides and carbides contributes for improving the flexural strength and fracture toughness of the material. These borides / carbides shall be reinforced directly into B<sub>4</sub>C matrix or generated by the in-situ chemical reaction of second phase additive with B<sub>4</sub>C. Levin et al. <sup>[10]</sup> reported the in-situ formation of TiB<sub>2</sub> phase in B<sub>4</sub>C matrix by the addition of TiO<sub>2</sub> as per the following reaction.



The formation of sub-stoichiometric boron carbide is mentioned to be the responsible for enhancing the sintering aptitude of the material. Addition of 40wt.% TiO<sub>2</sub> to B<sub>4</sub>C resulted in compact with 95%TD at 2160°C for 1h. In another study <sup>[28]</sup>, addition of TiC was found to be react with B<sub>4</sub>C resulting in the formation of TiB<sub>2</sub> and free carbon (in the form of graphite).



Goldstein et al. <sup>[12, 15]</sup> have investigated the sinterability of boron carbide with different metal oxides as sinter aids (TiO<sub>2</sub>, ZrO<sub>2</sub>, V<sub>2</sub>O<sub>5</sub>, Cr<sub>2</sub>O<sub>3</sub>, Y<sub>2</sub>O<sub>3</sub> and La<sub>2</sub>O<sub>3</sub>). The major solid reaction products were found to be borides. Such composites exhibited better densification aptitude in comparison with monolithic B<sub>4</sub>C.

#### **2.4.1.3 Silicon as sinter aid**

Silicon (melting point: 1410°C), when added as sinter additive, reacts with boron carbide and form silicon carbide, thus facilitate sintering at lower temperatures. In addition, the formation of SiC phase contributes for strengthening the B<sub>4</sub>C matrix. Silicon carbide has attractive properties, similar to that of boron carbide such as high hardness (28GPa), low specific gravity (3.1 g cm<sup>-3</sup>) and good wear resistance. Taylor et al. <sup>[111]</sup> and Mallick et al. <sup>[112]</sup> demonstrated the process of developing non-porous boron carbide structure by infiltrating Silicon into the porous B<sub>4</sub>C body. Any presence of unreacted free silicon lowers the mechanical properties of reaction bonded B<sub>4</sub>C.

#### **2.4.1.4 Other additives**

Boron carbide having density >98% was achieved at 2030°C upon addition of 20 mol.% CrB<sub>2</sub>. <sup>[113]</sup> The formation of eutectic phase in B<sub>4</sub>C-CrB<sub>2</sub> system was attributed to the enhanced densification. The resultant product exhibited high flexural strength of 525MPa and indentation fracture toughness of 3.7 MPa m<sup>1/2</sup>. Similar to CrB<sub>2</sub>, addition of 3 wt.% alumina (Al<sub>2</sub>O<sub>3</sub>) <sup>[35]</sup> was found to be beneficial in the sintering of B<sub>4</sub>C by the formation of liquid phase Al-B-C compound i.e., AlB<sub>12</sub>C<sub>2</sub>.

#### **2.4.2 Hot Pressing**

Pressureless sintering of boron carbide without sinter additive is extremely difficult to get the full dense products as cited above. Hot pressing is the commonly used method for fabricating dense monolithic borides and its composites. In hot pressing, temperature and pressure are

simultaneously applied to the powder compact using die. The sintering of powder in the presence of mechanical pressure causes increased stress at the particle to particle contact points and establishes stress gradient across the particle and thus, contributes for enhanced densification. Fine B<sub>4</sub>C powder is filled into the graphite die and then heated to the set sintering temperatures in vacuum or argon atmospheres. Uniaxial pressure of around 30-50 MPa applied during the dwell or soaking time at the sintering temperatures. The properties and microstructure of the densified components are influenced by the processing parameters such as hot pressing temperature, pressure, heating rate, atmosphere and holding time. However, hot pressing method is only able to fabricate simple shapes and complex geometry cannot be fabricated using this technique. [2]

Monolithic B<sub>4</sub>C was sintered to full density at >2100°C with an applied load of 30MPa. The density of B<sub>4</sub>C hot pressed at 2150°C for 10min was 91.6%TD and 99.7%TD when used B<sub>4</sub>C of particle sizes 3.8µm and 0.35µm respectively. [5, 114]

#### **2.4.2.1 Role of sinter additives**

Addition 1 to 5 wt.% B to B<sub>4</sub>C is reported to improve both the sinterability and mechanical strength of B<sub>4</sub>C. [30] High density B<sub>4</sub>C/Cu CER-MET (70vol.% B<sub>4</sub>C) exhibiting high thermal conductivity was prepared by hot pressing of Cu coated B<sub>4</sub>C powder for the nuclear reactor application. Skorokhod et al. [36] have developed B<sub>4</sub>C-15vol.% TiB<sub>2</sub> composite by hot pressing at 2000°C with 20MPa pressure for 1h in argon atmospheres. The resultant composite exhibited flexural strength of 621MPa and indentation fracture toughness of 6 MPa.m<sup>1/2</sup>. US Patent was filed on the process of preparing high strength (870MPa) B<sub>4</sub>C composites containing 5 to 30 mol.% TiB<sub>2</sub>. [115] Addition of 0.5% Fe was found to be playing a beneficial role by increasing the sinter densities of B<sub>4</sub>C-TiB<sub>2</sub> composite, due to the formation of Fe-Ti based liquid phase at the grain junctions. [116] Reaction sintering of B<sub>4</sub>C with

(W,Ti)C at 1850°C for 0.5h resulted in fine grain distribution of TiB<sub>2</sub> and W<sub>2</sub>B<sub>5</sub> as reinforced phases in B<sub>4</sub>C matrix. [29] Li et al. prepared a composite containing B<sub>4</sub>C, SiC, TiB<sub>2</sub> and BN phases by reaction hot pressing of B<sub>4</sub>C, Si<sub>3</sub>N<sub>4</sub>, SiC and TiC powders. [117] Hot pressed B<sub>4</sub>C containing VB<sub>2</sub> and C phases was reported to exhibit high hardness and flexural strength suitable for wear and shock resistance applications. Hot pressing of B<sub>4</sub>C with the addition of oxides/carbides/nitrides has been successfully demonstrated to achieve high dense B<sub>4</sub>C composites at lower the sintering temperatures in comparison with monolithic B<sub>4</sub>C by activating reaction sintering mechanisms. Hot pressing a mixture of Si, B and C was reported to prepare a composite containing B<sub>4</sub>C and SiC (referred as combustion hot pressing). The developed composite exhibited interlocked microstructure with low porosities. [118] Machinable ceramic, B<sub>4</sub>C with 20wt.%BN composition was developed by hot-pressing technique. [34] TiC along with Cobalt was also tested as sinter additives to B<sub>4</sub>C at temperatures <1500°C and high pressure of 5-6GPa. [119]

### **2.4.3 Hot Isostatic Pressing (HIP)**

The HIP process, is also referred as gas pressure bonding, uses the combination of high pressures and temperature to densify the powder materials. The sample is pressurized inside the pressure vessel. An inert gas is usually the pressure transmitting medium to the powder to be compacted. Encapsulation or pre-sintering treatment of powder compact is the pre-requisite for the HIP processing. A resistance heated furnace inside the vessel is the temperature source. The high pressure provides a driving force for material transport during sintering which allows the densification to proceed at considerably lower temperature in comparison to that of conventional sintering (PLS and HP). The pressure applied in the HIP process is in the range of 100-300MPa, whereas 30-50MPa is applied during HP process. Larson et al. [120] reported the effect of addition of B, Si, SiC to B<sub>4</sub>C, during hot isostatic

pressing at 1850°C for 1h under a pressure of 160MPa. Combination of Pressureless sintering and post-HIP results in achieving 100%TD B<sub>4</sub>C, at 2150°C for 125min with a mechanical pressure of 310MPa. [121]

#### **2.4.4 Spark Plasma Sintering**

The use of pulsed electric field has a rich history of achieving rapid consolidation and at the same time preserving particle size in the densified micro/nanostructure. It's origin dates back to the patent issued in 1930s on a method describing electric discharge or current for aiding sintering of powders or sinter-joining of metals. [122-123] Subsequently, the work on “spark sintering” was reported by Lenel (PRI, 1950s), Scientists at LMSC, California and Inoue, Japan in the 1960s and 1970s, respectively. [124-126] The objective of rapid consolidation technique is to suppress particle coarsening and enhance particle sintering. The acronyms for the processes which use electric fields to achieve quick sintering have underwent many incarnations during the last two decades. Some of them include plasma pressure compaction (PPC), electric pulse assisted consolidation (EPAC), field-assisted / activated sintering technique (FAST), pulsed electric current sintering (PECS), and the most popular of all: Spark Plasma Sintering (SPS). [20, 127]

Spark plasma sintering (SPS) is a process that combines simultaneous application of mechanical pressure and electric current directly on the sample. The main difference between SPS and other sintering methods is that both die and powder are directly heated by the passage of pulsed dc current. This implies that the die assembly acts as a heating source. The sintering unit consists of a uniaxial pressure device, where water-cooled punches serves as electrodes, reaction chamber that shall be evacuated, direct current (pulsed dc) generator and regulating systems (for position and temperature). Specific advantages of SPS over

conventional sintering techniques are (1) faster heating rate, which avoids those mass transport mechanisms that do not contribute to densification, (2) shorter dwell time, that retains finer microstructures and (3) DC pulse voltage that contributes for enhanced mass transport through electro-migration. [20-24]

It is well known that oxygen contamination, in the form of  $B_2O_3$  present over the surface of  $B_4C$  particles, hinders the densification of  $B_4C$  as explained in preceding sections. During SPS, generation of spark discharges is reported to cleanse the surface oxides and promotes the densification. Gosh et al. [128] densified submicron sized particles of  $B_4C$  to 99%TD at  $1750^\circ C$  in 5min duration with a mechanical pressure of 88MPa using SPS. The mean grain size of SPS processed  $B_4C$  was reported to be  $\sim 2\mu m$ . Koderá et al. [129] investigated the processing of B-C mixtures in SPS, which results in the simultaneous synthesis and densification of  $B_4C$  at  $1900^\circ C$ . 98%TD  $B_4C$  was prepared using the reaction spark plasma sintering.

In an SPS experiment, a weighed amount of powder is filled into the die and plunger assembly. The die is made up of high temperature resistant materials such as carbon, WC, refractory alloys, etc.

Some of the earliest work on difficult-to-sinter additive-free AlN ceramics was done at UC Davis in the early 1990s by Risbud and his colleagues using a commercial PAS machine (from Sodick Corporation in Japan). Since then, many studies have demonstrated that SPS is capable of producing dense compacts with finer grain sizes, at lower sintering temperatures and dwell times. SPS has emerged as one of the most significant and effective sintering techniques in a generation. The success of the process has been highlighted by noteworthy achievements such enhanced superplasticity in ceramics, higher permittivity in ferroelectrics, improved magnetic properties, improved bonding quality, improved thermoelectric properties

and reduced impurity segregation at grain boundaries. Furthermore, through prior mechanical activation (high energy ball-milling) of reactant powders, the SPS process has been used to simultaneously synthesize and densify nanostructured ceramic, intermetallic and composite materials in bulk form. It has also been used to microalloy ceramics for ductility improvement, and to form functionally-graded materials. The above cited references serve only as examples of a large number of investigations published on the use of the SPS method.

[20, 127, 130-131]

#### **2.4.4.1 SPS Mechanism – An unresolved mystery**

The success of the SPS method in sintering studies <sup>[20, 127]</sup> has been attributed to the role of plasma that is generated between particles, which explains for the term spark plasma sintering. The action of this plasma discharge assists in the removal of any surface oxides / contaminations from the particle surface and activates the surface which is believed to be the reason for enhanced sintering. However, the presence of plasma in spark plasma sintering system is still unproven as there is no direct evidence reported its existence. Thus, the role of the pulsed current remains not adequately understood and the underlying mechanism(s) responsible for rapid densification still remains unanswered.

#### **2.4.4.2 Advantages of SPS**

Specific advantages of SPS over conventional sintering techniques are (1) faster heating rate, which avoids those mass transport mechanisms that do not contribute to densification, (2) shorter dwell time, that retains finer microstructures and (3) DC pulse voltage that contributes for enhanced mass transport through electro-migration. <sup>[20-24]</sup>

## 2.5 Summary of literature review and proposed investigation

Though the near theoretical dense compacts can be obtained by both HP and HIP techniques, their ability to retain fine grain microstructures is rather limited, owing to the necessity of longer densification period during which grain growth and densification kinetics competes with each other. Processing B<sub>4</sub>C in the presence of sinter-aid additions are reported to lower the consolidation temperatures and thus helps in consolidating product with reduced grain coarsening effects, but at the expense of purity of final product. Purity is of prime concern for applications in nuclear industries. <sup>[1-2]</sup> Thus, there is a need of new sintering techniques which would alleviate the sintering conditions for attaining high dense and fine grain B<sub>4</sub>C ceramics without the need of sinter additions. The first part of the thesis probes the influence of direct contribution of spark plasma sintering parameters (time, temperature and Pulsed DC) on the densification of boron carbide and its corresponding impact on microstructure development and mechanical properties.

Till date, most of the oxides, investigated as additives are based on transition metal oxides (TiO<sub>2</sub>, ZrO<sub>2</sub>, HfO<sub>2</sub>, V<sub>2</sub>O<sub>5</sub>). <sup>[12-15, 17-18, 36-37, 40-42]</sup> It is worthwhile to mention that almost all the transition metal oxides, used as sinter additives to B<sub>4</sub>C, result in enhanced densification. On the other hand, sintering experiments of boron carbide using rare earth oxide as sinter-aid are rather limited. Goldstein et al. <sup>[15]</sup> developed high dense B<sub>4</sub>C compacts (>95%pth) by pressureless sintering at 2180°C with the addition of transition metal oxides and rare earth metal oxides. The results indicated that the role of rare earth oxides (La<sub>2</sub>O<sub>3</sub> and Y<sub>2</sub>O<sub>3</sub>) as sinter-aids is much more effective, when compared to transition metal oxides. On contrary, Wei et al. <sup>[43]</sup> reported the lack of densification with only rare earth metal oxide (especially Eu<sub>2</sub>O<sub>3</sub> and Sm<sub>2</sub>O<sub>3</sub>) as sinter-aid to B<sub>4</sub>C. However, when B<sub>4</sub>C was added to the composite mixture of both rare earth oxide and phenolic resin, the resultant compact exhibited improved

sinterability. <sup>[43]</sup> The reason for decreased sintering aptitude of B<sub>4</sub>C in the presence of only rare earth oxide addition (Eu<sub>2</sub>O<sub>3</sub> and Sm<sub>2</sub>O<sub>3</sub>) is not yet clearly understood. In the above backdrop, it is worth to probe into the influence of rare earth oxide as sinter-aid to B<sub>4</sub>C, which comprises the second part of this thesis. In addition to the above-mentioned perspective on sinterability aspect, the combination of rare earth containing compound(s) to boron carbide is expected to superior neutron absorption characteristics and have potential for application as high temperature neutron absorber material.

**In Summary:**

The first part of the thesis is to take into consideration a direct contribution of spark plasma sintering parameters on the densification of boron carbide. Subsequently, second part of the thesis deals with the sinterability and properties of boron carbide in the presence of sinter-aid (Eu<sub>2</sub>O<sub>3</sub>) using SPS.

---

## Chapter 3: Experimental Work

---

The experimental techniques and methodologies employed in the present study to meet the objectives are described in this chapter. The chapter includes details of starting powders, powder processing under different parametric conditions, densification techniques, phase and microstructural characterisation of sintered samples, evaluation of mechanical and thermo-physical properties.

### 3.1 Starting materials

**Boron Carbide powder:** The chemical assays of B<sub>4</sub>C powder used in the experiments are given in Table 1. The B<sub>4</sub>C powders are compliant with ASTM C 750 Type 1 specifications. The detail of synthesis procedure is reported elsewhere.<sup>[132]</sup>

**Europium oxide powder:** Eu<sub>2</sub>O<sub>3</sub> powder of purity better than 99% pure was sourced from Indian Rare Earths Limited, India.

**Table 3.1: Chemical assay of B<sub>4</sub>C powder used in the experiments**

Constituent	B <sub>4</sub> C
Total Boron (wt.%)	77.7
Total Carbon (wt.%)	22.0
Oxygen (wt.%)	<0.2
Metallic impurities(wt.%)	< 0.3
Total Boron + Carbon (wt.%)	99.7

## 3.2 Characterization of starting powders

### 3.2.1 Particle size analysis

Particle size analyses of starting powders were carried out using a laser diffraction particle size analyser (1064 liquid, Cilas, France). The technique is based on the combination of Fraunhofer diffraction and Mie's scattering theories. For particle size analysis the powder is dispersed in a recirculating de-ionized water system by ultrasonic agitation for 60 seconds. The laser beam interacts with the dispersed particle while these pass through the sample cell. For particles that are large compared to the wavelength of beam, the laser beam incident on the particles is scattered through angles that are inversely proportional to particle size. Multiple detectors are located at different angles in order to measure the number of counts. Scanning of the angular distribution of scattered light flux provides information on particle size and size distribution. Typical particle size distribution of different powders used in the experiments are given in Table 3.2.

**Table 3.2: Typical particle size distribution of starting materials used in the experiments**

<b>Constituent</b>	<b>D<sub>10</sub>, μm</b>	<b>D<sub>50</sub>, μm</b>	<b>D<sub>90</sub>, μm</b>
B <sub>4</sub> C powder	0.42	2.40	8.83
Eu <sub>2</sub> O <sub>3</sub> powder	1.94	4.18	10.69

### **3.2.2 Phase confirmation of powder by XRD analysis**

In order to confirm the phase purity, the starting powders were characterized by X-ray diffraction technique (XRG3000, INEL, France and RIGAKU, Japan) using  $\text{CuK}\alpha$  radiation. Powder samples were kept over the glass holders (plate) and exposed to the X-ray beam. The samples were scanned at a  $2\theta$  angle range of 20 to  $80^\circ$  with a scan rate of  $0.02^\circ/\text{s}$  using  $\text{CuK}\alpha$  radiation. The XRD patterns were used to identify the phases with reference to the standard JCPDS powder diffraction files.

### **3.3 Preparation of powder mixtures used in the study**

$\text{B}_4\text{C}$  powder was mixed with  $\text{Eu}_2\text{O}_3$  of varying proportions (0, 5 and 10 vol.%  $\text{Eu}_2\text{O}_3$ ) for carrying out the experiments. The amounts correspond to 0, 13.4 and 25.4 wt.%  $\text{Eu}_2\text{O}_3$ . Powders were taken in desired weight ratio and mixed in planetary ball mill (Fristch, Germany) for 2 hours duration at 150 rpm, using ethyl alcohol as wet medium. WC-lined pots and 10 mm diameter WC balls were used for mixing/milling in planetary ball mill. The ball to charge weight ratio was kept as 1:1.5. The powder mixture was dried in a vacuum oven at  $80^\circ\text{C}$  for 3 hours.

### **3.4 Study of reaction mechanism**

#### **3.4.1 Thermogravimetric analysis of powder mixture**

In order to understand the phase evolution behaviour, thermogravimetry (TG) - differential thermal analysis (DTA) (SETARAM, SETSYS Evolution 2400) of the  $\text{B}_4\text{C}$ -10 vol%  $\text{Eu}_2\text{O}_3$  mixture was conducted to identify the onset temperatures for sintering.  $\text{B}_4\text{C}$ -10 vol%  $\text{Eu}_2\text{O}_3$  composite mixture was loaded into the graphitic crucible and heat treated up to  $1700^\circ\text{C}$  under dynamic vacuum conditions. Experiments were conducted with a constant heating rate of 10

°C/min. A derivative weight loss curve was used to identify the onset temperatures of reactions involving weight loss.

### **3.4.2 Powder compaction and pyro-vacuum treatment**

The homogenized powder mixture ( $B_4C$ -10vol%  $Eu_2O_3$ ) was compacted into green pellets (20 mm dia.) under pressure (280 MPa) using semi-hydraulic press. The green pellets were loaded into the graphite crucible and subjected to heat treatment at different temperatures (1100, 1500 and 1900°C) in dynamic vacuum conditions in order to understand the phase evolution. The temperatures were chosen based on TG-DTA results. In the present study, 40 kW capacity vacuum induction furnace was used for the heat treatment of starting materials. Experiments were conducted with a constant heating rate of 10°C/min. Temperature of the charge was monitored using a two-colour pyrometer with an accuracy of  $\pm 15^\circ\text{C}$ . The furnace was programmed to cool immediately upon reaching the desired set temperatures without giving any dwell time period so as to understand the phases present at the investigated temperatures ranges.

### **3.4.3 XRD phase analysis of pyro-vacuum treated material**

The pyro-vacuum treated material was crushed into fine powder form to make sample for XRD analysis. The details of the XRD experimental technique is given in Section 3.2.2.

## **3.5 Densification techniques**

### **3.5.1 Spark plasma sintering**

A schematic of Spark Plasma Sintering (SPS) unit is shown in Fig 3.2. Specific advantages of SPS over conventional sintering techniques are: (i) faster heating rate which avoids those

mass transport mechanisms that do not contribute to densification (ii) shorter dwell time that helps in retaining finer microstructures and (iii) DC pulse voltage that contributes to enhanced mass transport through electro-migration [17-22].

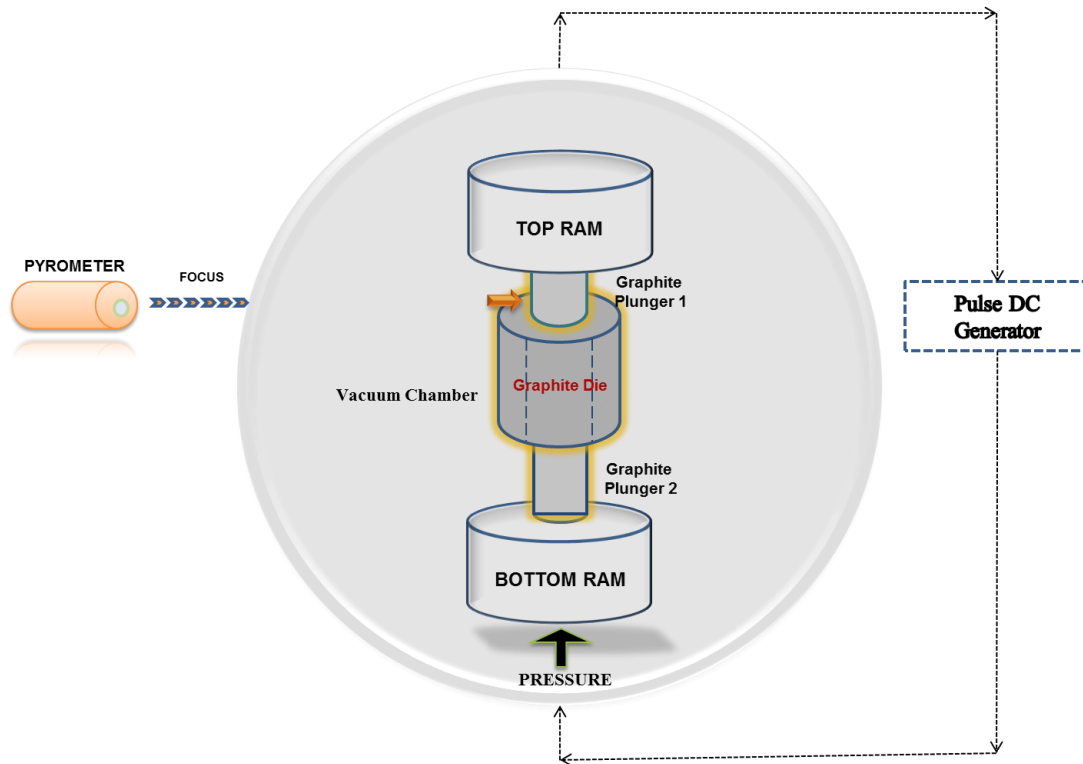


Fig. 3.1 Schematic of Spark Plasma Sintering (SPS) Facility showing the location of temperature measurement by optical pyrometer

High-density graphite die of 17mm diameter  $\times$  50mm height was used for consolidation through spark plasma sintering (Dr.Sinter, SPS-515S, SPS Syntex Inc., Japan). A piece of grafoil® sheet (0.45 to 1.0 mm thick) was lined internally in the graphite die and also placed in between powder and plunger in order to avoid the interaction of the charge material with the graphite die components. The powder was charged in the high density graphite die. The die set filled with powder was then placed inside the SPS processing chamber and evacuated to a vacuum level of  $10^{-3}$  mbar. Standard DC pulse ON–OFF sequence (5 ms–5ms) was chosen for all the experiments and the pulse was considered as square waveform type (Fig. 3.3).

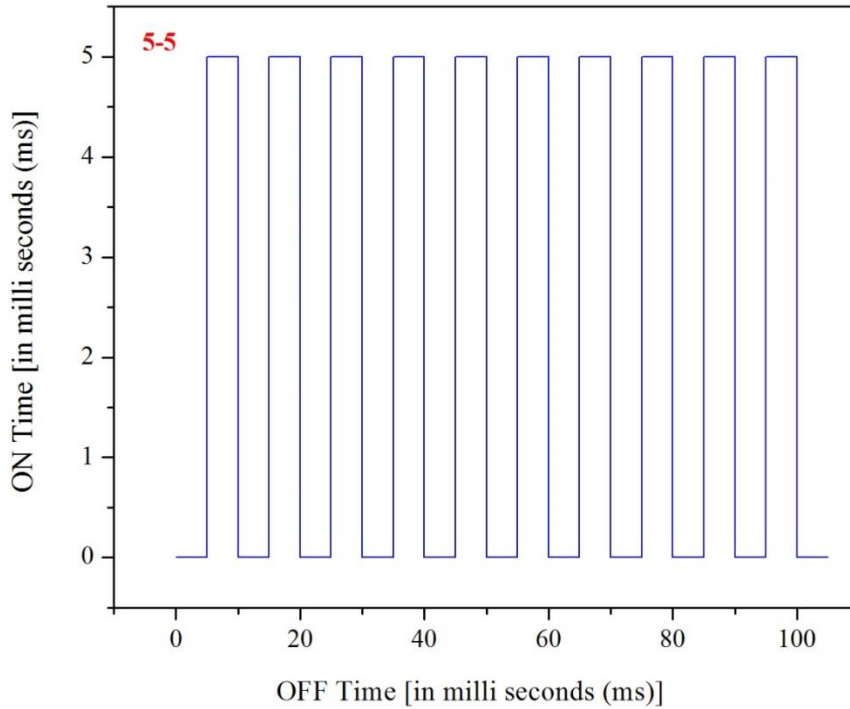


Fig. 3.2 Schematic of Pulsed DC waveform showing 5-5 (ms-ms) pulse sequence during the holding period.

Ram displacement of SPS was tracked throughout the experiment, which also indicates three stages of displacement which is in correlation with that of densification plot (Fig. 5.1). As the top ram is static, any relative displacement of bottom ram along positive or negative direction from its initial position corresponds to contraction or expansion of the material, respectively. The net displacement observed during processing of B<sub>4</sub>C samples includes shrinkage from loaded powders and expansion of graphite plunger due to heating. The calibration experiment was performed under identical processing conditions using full dense B<sub>4</sub>C pellet instead of

powder. The true shrinkage behaviour of B<sub>4</sub>C samples was determined by alleviating the effects that arising from the thermal expansion of graphite plungers.

Spark plasma sintering experiments were conducted with monolithic B<sub>4</sub>C at different temperatures in the range of 1100 – 1900°C under 45MPa applied pressure and 15min holding time at the set temperature. A minimum load of 2kN was applied at the start, in order to ensure firm contact of electrodes with the plunger/sample/die set up. The heating rate above 1000°C was maintained as 100°C/min. Sintering temperature was measured by focusing the optical pyrometer at the graphite plunger which is in direct contact with the powder compact as shown in Fig. 3.2. A maximum load of 12.5 kN (50 MPa) was applied at a rate of 0.25 kN/s when the temperature reached the set point. Holding time was maintained for 5, 10 and 15 min at that set temperatures. After completion of experiment, furnace was allowed to cool down to room temperature and the pellets were ejected from the die. The ejected pellets were cleaned on both the edges and circumference by removing the grafoil®. The influence of process parameters on the densification behavior was studied. Based on this initial set of experiments, B<sub>4</sub>C powder added with 5 and 10 vol% Eu<sub>2</sub>O<sub>3</sub> were also consolidated in vacuum at 1900°C for 15 min duration under the mechanical pressure of 45 MPa. The heating rate was programmed at 100°C/min.

### **3.5.2 Densification by hot pressing**

In order to fabricate the larger specimens for the evaluation of mechanical properties particularly the flexural strength, monolithic B<sub>4</sub>C and B<sub>4</sub>C-Eu<sub>2</sub>O<sub>3</sub> composite mixtures were manufactured using conventional hot-pressing procedures (since, the existing SPS facility has a limitation of fabricating larger sample dimensions). The calculated amount of powders was

loaded into the high-density graphite die having cavity dimension of 100 mm (in diameter). The hot pressing was carried out at a set temperature of 1950°C for 2h duration under a mechanical pressure of 45 MPa. Prior to hot-pressing, the furnace chamber was evacuated to a vacuum of the order of  $10^{-4}$  mbar and the furnace heating rate was set to be 10°C/min. After completion of experiment, furnace was allowed to cool down to room temperature and the pellets were ejected from the die.

### **3.6 Density, Phase and Microstructural analysis of Sintered Pellets**

#### **3.6.1 Measurement of pellet dimensions and density**

Dimensions of the pellets were measured using a micrometer (Mitutoyo, Japan) having a least count of 1.0  $\mu\text{m}$ . Measurements were taken at three different positions and average value was taken. Before dimensional measurement two faces were polished in an automatic polishing machine (Struers, Denmark) to make the faces parallel to each other. It may be mentioned here that this polishing is also necessary for the samples to be used for electrical measurement. The densities of the sintered compacts were measured by water displacement method as well as from dimensional measurement.

#### **3.6.2 Phase analysis of sintered pellets**

The phase analysis of sintered compacts was carried out by X-ray diffraction. X-ray diffraction patterns of the sintered pellets were obtained using X-ray Diffractometer (XRG3000, INEL, France and RIGAKU, Japan) having  $\text{CuK}\alpha$  radiation. Scan rate as described in Section 3.2.2 was used for all the samples.

### **3.6.3 Optical Microscopy**

Samples used for microstructural characterisations were polished down to 1 $\mu$ m finish using series of diamond suspensions ranging from 15 $\mu$ m-1 $\mu$ m grades (Struers, Denmark). After mechanical polishing, compacts were chemically etched using a modified Murakami's solution (15gm K<sub>3</sub>FeCN<sub>6</sub> and 15 g KOH in 60 ml of water) at 100°C for about 30 min. Microstructural features of the etched sintered samples were examined by an inverted type optical microscope (DMI 5000, Leica, Germany).

### **3.6.4 Scanning electron microscopy**

Sintered surfaces and fracture surfaces were characterized using scanning electron microscopes (SEM; MB 2300 CT/100, CAMSCAN, UK and FESEM, Carl Zeiss). The samples were coated with gold (using d.c. sputtering unit), before examination in SEM.

### **3.6.5 Transmission electron microscopy**

Thin TEM samples were sliced out of sintered composite pellets using wire EDM and subsequently thinned down to electron transparency with ion milling unit. TEM and STEM observations were carried out using FEI-Tecnai T20 and JEOL 3010, respectively, operated at 200 KeV.

## **3.7 Evaluation of Mechanical Properties Sintered Compacts**

### **3.7.1 Measurement of elastic modulus**

Elastic modulus (E) of the sintered compacts was measured by ultrasonic pulse-echo technique (UT 340 pulser receiver system, UTEX Scientific Instrument Inc., Canada) using 15 MHz normal beam probe.

$$E = \frac{V_L^2 \rho (1 + \nu)(1 - 2\nu)}{(1 - \nu)}$$

where,  $V_L$  – Longitudinal velocity,  $\rho$  – density and  $\nu$  - Poisson ratio of the material, which is considered to be 0.18.

### 3.7.2 Microhardness measurement

Before hardness measurement samples were polished down to 1 $\mu$ m finish using series of diamond suspensions ranging from 15 $\mu$ m – 1 $\mu$ m grades (Struers, Denmark). Hardness and fracture toughness were measured based on Vickers indentation technique using different loads for a specified period of time (in sec) (Duramin 2, Struers, Denmark). The hardness value was calculated from indentation size using,

$$H_v = 1.854 \frac{P}{d^2}$$

where, P is indentation load and d is mean length of indent diagonal.

### 3.7.3 Measurement of fracture toughness by indentation method

The indentation fracture toughness of sintered compacts was evaluated by measuring the crack lengths formed around the corners of Vickers indents. Anstis methodology <sup>[24]</sup> was adopted for fracture toughness calculations.

$$K_{IC} = 0.016 \sqrt{\frac{E P}{H \frac{3}{c^2}}}$$

where, E - Elastic modulus, H - Hardness, P - Indentation load and c - Average length of the cracks obtained in the tips of the Vickers marks. Measured elastic modulus values were incorporated in the indentation fracture toughness calculations.

### 3.7.4 Measurement of Flexural Strength

Flexural strength of monolithic B<sub>4</sub>C and B<sub>4</sub>C-Eu<sub>2</sub>O<sub>3</sub> (5 vol.% and 10 vol.%) composites were determined by three-point bend test. The rectangular samples of uniform dimensions of 4×5×25 mm are machined out of hot pressed blocks. Universal testing machine (Zwick-Roell Z005) was used to conduct the three-point bending test. The samples to be tested are polished well and the edges are chamfered. The samples are placed on a span of 20mm and a point load is applied at the center at a rate of 0.5mm/min. The dimensions of each and every sample are accurately measured before testing and the failure load was noted down. 40 different samples of each composition have been tested and the flexural strength has been calculated. The flexural strength ( $\sigma$ ) of the samples is calculated using the following formula,

$$\sigma = \frac{3PL}{2bd^2}$$

where, P- Failure load, L- Span length, b- Width of the sample, d- Depth of the sample.

The flexural strength ( $\sigma$ ) values were ranked from the minimum to the maximum value and for each strength value a probability of failure  $P(\sigma)$  is assigned based on its ranking  $i$ , with  $i$  ranging from 1 to N, where N is the number of measurements of flexural strength for samples of a particular material. The cumulative probability of failure  $P(\sigma)$  is calculated using the following equation.

$$P(\sigma) = \frac{i-1/2}{N}$$

Following Weibull distribution function, the generalized strength distributions law can adopt the following expression.

$$P(\sigma) = 1 - \exp\left[-\frac{V}{V_o}\left(\frac{\sigma}{\sigma_o}\right)^m\right]$$

where, V is the volume of the material tested, V<sub>o</sub> is the reference volume, σ<sub>o</sub> is the characteristic flexural strength of the material at which probability of failure is 0.63.

The above equation can be re-written as:

$$\ln[-\ln(1 - P(\sigma))] = \ln\frac{V}{V_o} + m \ln\left(\frac{\sigma}{\sigma_o}\right)$$

Characteristics flexural strength and Weibull modulus (m) have been obtained from the linear fitted plot of ln[-ln(1 - P(σ))] versus ln(σ).

### **3.8 Evaluation of thermal conductivity of sintered samples**

Thermal diffusivity was measured using laser flash technique. The samples of 10 mm diameter and 2 - 3 mm thickness were made for thermal conductivity measurement. The laser flash method is a well-known technique for the measurement of the thermophysical properties (thermal diffusivity, specific heat and thermal conductivity) of solid materials. Easy sample preparation, fast measurement times and high accuracy are only some of the advantages of this non-contact, non-destructive testing technique. The method involves uniform irradiation of a small, disc-shaped sample over its front face with a very short pulse of energy. The time-temperature history of the rear face is recorded through high-speed data acquisition from a solid-state optical sensor with very fast thermal response. An

instantaneous light source is used to uniformly heat up the sample's front side and a detector (infrared radiation thermometer) measures the time-dependent temperature rise at the rear side. Heat conduction is assumed to be one-dimensional (i.e. no lateral heat loss). The test sample is usually prepared by spraying a thin layer of colloidal graphite on both sides to increase the absorption and radiation of thermal energy. It is worth mentioning here that the stringent requirements of specimen dimensions (10mm diameter and 2.5mm thickness) were met by electron discharge machining of the ceramic sample. The literature reported heat capacity values of B<sub>4</sub>C and EuB<sub>6</sub> compositions have been considered for the calculation of thermal conductivities of developed composite materials.

### **3.9 Measurement of electrical conductivity of sintered samples**

Circular disc samples of 10mm dia. x 3mm thick were used for electrical resistivity measurement in the temperature range from ambient to 300 °C. Silver paste was used to coat both the faces of sintered pellets. After coating the paste was allowed to dry. The continuity of the platinum layer was checked using a multimeter. A high impedance current source is used to supply current and a voltmeter measures the voltage across the sample. The resistivity of the samples was determined using the following formula,

$$\rho = R \frac{A}{l}$$

where,  $\rho$  is the resistivity of the sample, R is the resistance of the sample, A is cross sectional area and  $l$  is the distance between two probes.

---

## **Chapter 4: Results and Discussion**

### **(Phase Evolution and Reaction Mechanism)**

---

Thermal analysis (TG-DTA) and X-ray diffraction techniques have been primarily used to study the phase evolution and reaction mechanism in  $\text{Eu}_2\text{O}_3$  added  $\text{B}_4\text{C}$  system.  $\text{B}_4\text{C}$ -10vol.%  $\text{Eu}_2\text{O}_3$  composition has been chosen as a representative sample. Commercial  $\text{B}_4\text{C}$  ( $d_{50} \sim 5\mu\text{m}$ , 99% purity) and  $\text{Eu}_2\text{O}_3$  ( $d_{50} \sim 0.7\mu\text{m}$ , 99% purity) powders were used as the starting materials in the present study.

#### **4.1 Thermal Analysis of $\text{B}_4\text{C}$ - $\text{Eu}_2\text{O}_3$ System**

Thermal analysis (TG-DTA) of  $\text{B}_4\text{C}$ -10vol%  $\text{Eu}_2\text{O}_3$  composite mixture was conducted up to  $1700^\circ\text{C}$  under dynamic vacuum condition. TG-DTA plots and derivative plots of the TG-DTA data are shown in Figure 4.1. Based on the slope changes observed at  $970^\circ\text{C}$  and  $1580^\circ\text{C}$  in thermo-gravimetric plot, it could be appropriate to speculate the occurrence of the reaction between  $\text{B}_4\text{C}$  and  $\text{Eu}_2\text{O}_3$  in multiple steps. First slope change noticed at  $970^\circ\text{C}$  could be the onset temperature for reaction between  $\text{B}_4\text{C}$  and  $\text{Eu}_2\text{O}_3$  mixtures. Second change in TG plot at  $1580^\circ\text{C}$  indicates the occurrence of another possible chemical reaction, resulting in weight loss of the reaction mixture.

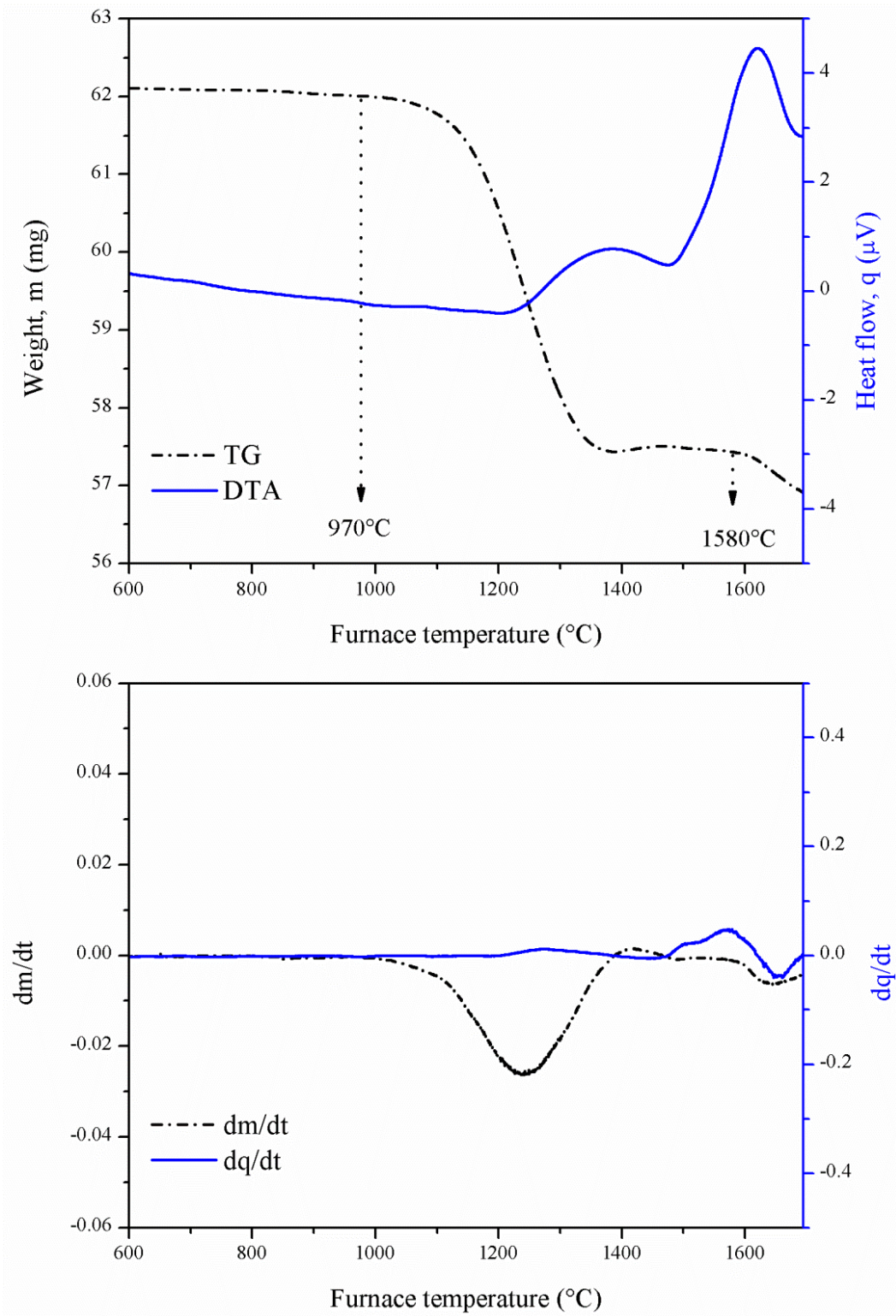


**Fig. 4.1: (a) TG-DTA plots obtained for B<sub>4</sub>C-10vol.% Eu<sub>2</sub>O<sub>3</sub> composite mixture, (b) derivative plots of the TG-DTA data**

In order to understand phase evolution, the  $B_4C$ - $Eu_2O_3$  composite mixture was subjected to segmented heat treatments at 1100, 1500 and 1900°C under vacuum. X-ray diffraction patterns of  $B_4C$ -10vol%  $Eu_2O_3$  composite mixture after heat treatment at three different temperatures are shown in Figure 4.2. The X-ray diffraction pattern of commercial  $B_4C$  powder used in the experiments is also shown in the same figure for comparison. The XRD pattern of  $B_4C$  powder confirmed phase purity within the detection limit of XRD technique.

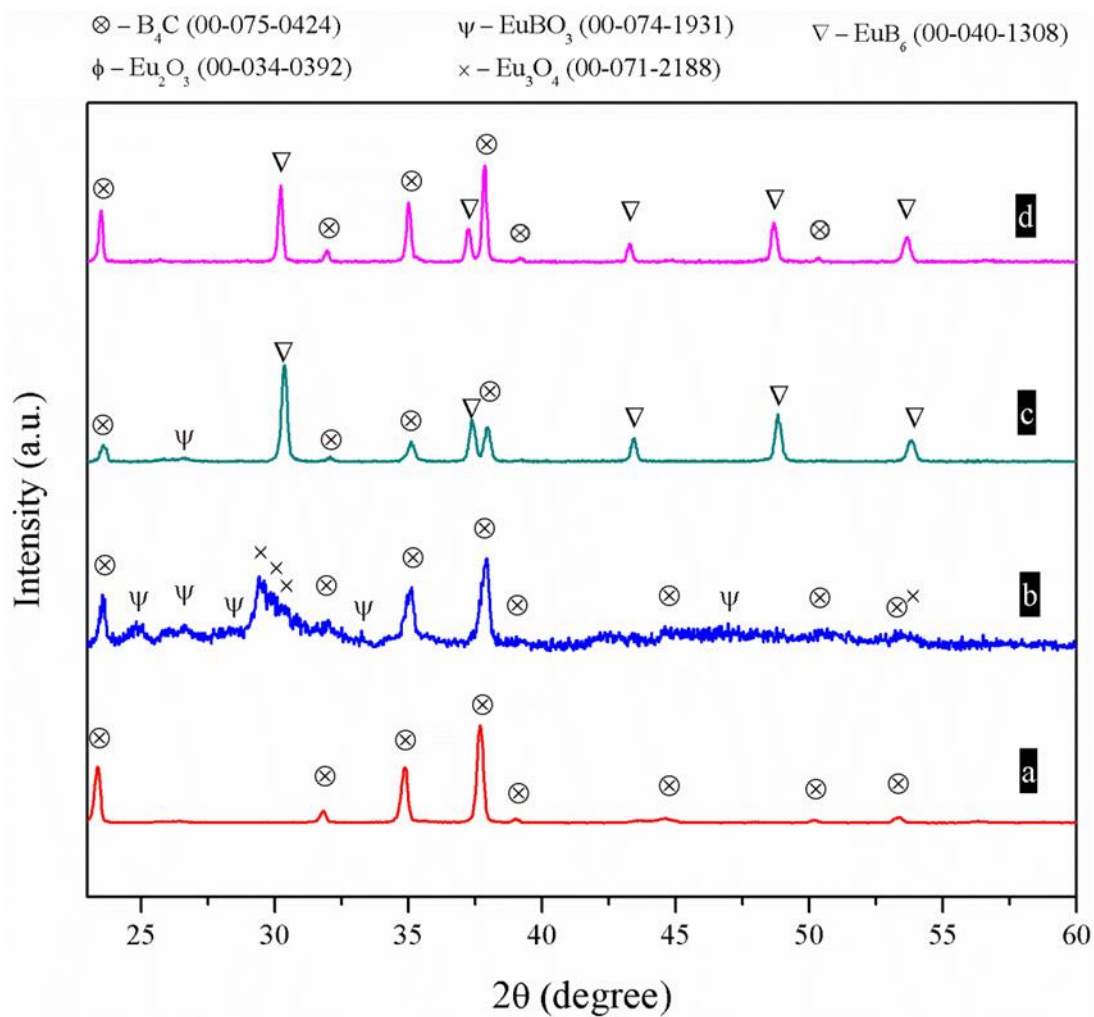


**Fig. 4.2: X-ray diffraction patterns of (a)  $B_4C$  powder (for comparison) and  $B_4C$ -10vol.%  $Eu_2O_3$  composite mixture heat treated under vacuum at different temperatures (b) 1100°C, (c) 1500°C, (d) 1900°C (with no dwell time)**

B<sub>4</sub>C-Eu<sub>2</sub>O<sub>3</sub> sample processed at 1100°C indicates the presence of B<sub>4</sub>C, Eu<sub>3</sub>O<sub>4</sub> and EuBO<sub>3</sub> as the major phases. The sample after pyro-vacuum treatment at 1500°C exhibited B<sub>4</sub>C and EuB<sub>6</sub> as major phases. Also, the minor peak at 26.77°(2θ) in XRD pattern indicates the presence of EuBO<sub>3</sub> phase. B<sub>4</sub>C and EuB<sub>6</sub> are the only phases that were recorded in the XRD pattern of the sample treated at 1900°C. Phases obtained in the composite samples processed under different conditions are summarized in Table 4.1.

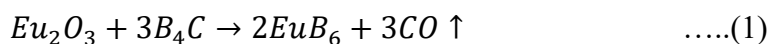
**TABLE 4.1: Phase assemblage in samples obtained after pyro-vacuum treatment of B<sub>4</sub>C-10 vol% Eu<sub>2</sub>O<sub>3</sub> powder mixture**

Processing temperature (°C)	Dwell time (min)	Phases identified
1100	0	B <sub>4</sub> C [00-075-0424], Eu <sub>3</sub> O <sub>4</sub> [00-071-2188] and EuBO <sub>3</sub> [00-074-1931]
1500	0	B <sub>4</sub> C, EuB <sub>6</sub> [00-040-1308] and EuBO <sub>3</sub>
1900	0	B <sub>4</sub> C and EuB <sub>6</sub>

\* In brackets: JCPDS reference given

## 4.2 Phase Assemblage of Sintered B<sub>4</sub>C-Eu<sub>2</sub>O<sub>3</sub>

X-ray diffraction patterns of the starting powders and sintered compacts are shown in Figure 4.3(i). The peaks present in XRD pattern of the sintered composite samples can be indexed with B<sub>4</sub>C and EuB<sub>6</sub> phases (Table 4.2). The following chemical reaction (1) is considered to occur between B<sub>4</sub>C and Eu<sub>2</sub>O<sub>3</sub> during the sintering process to form EuB<sub>6</sub>.



The absence of  $\text{Eu}_2\text{O}_3$  phase, within the detection limit of XRD, indicates the possibility of complete conversion of  $\text{Eu}_2\text{O}_3$  phase into  $\text{EuB}_6$  due to the above reaction.

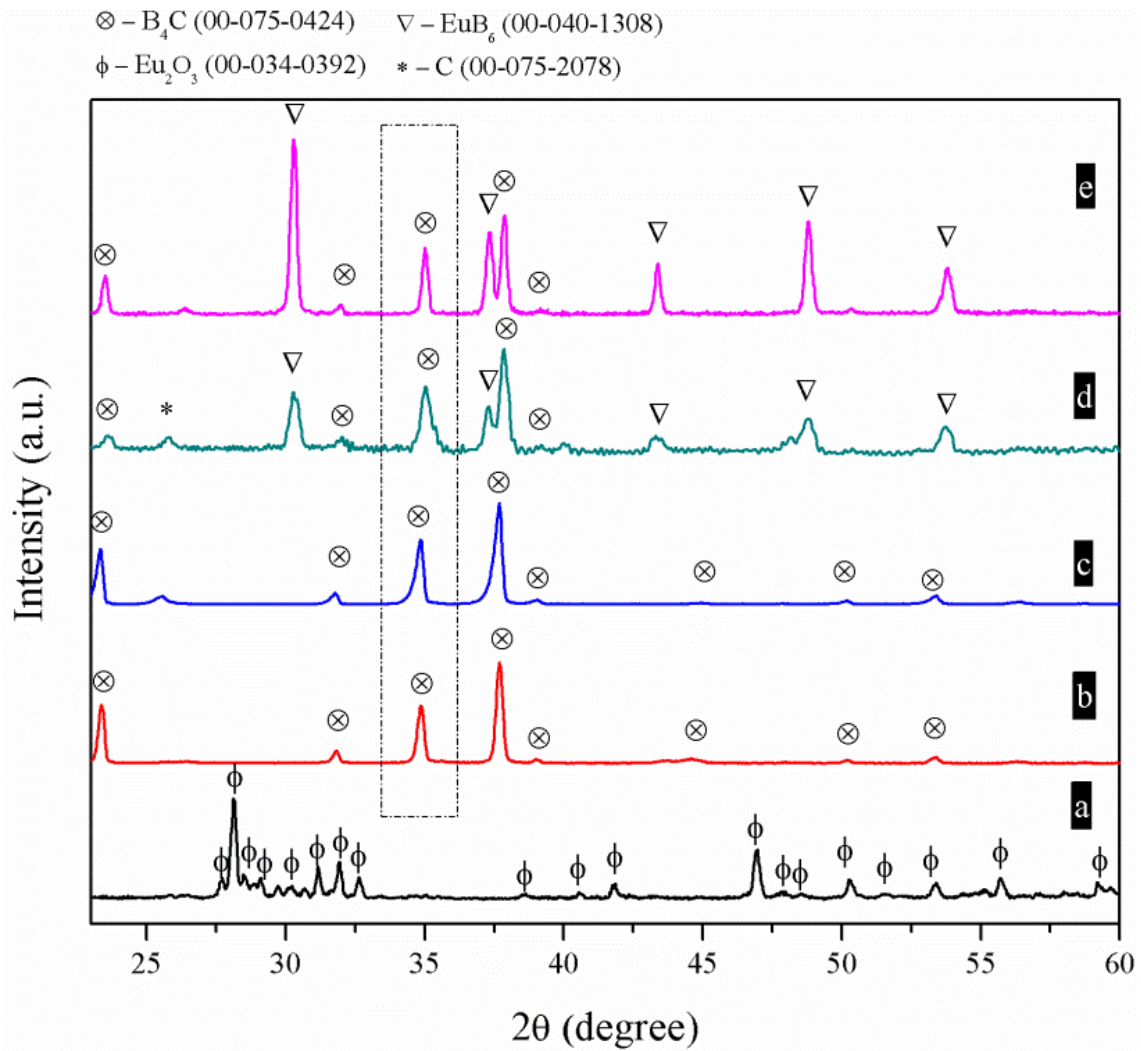


**Fig. 4.3: (i) X-ray diffraction patterns of (a)  $\text{Eu}_2\text{O}_3$  powder, (b)  $\text{B}_4\text{C}$  powder, (c) sintered monolithic  $\text{B}_4\text{C}$ , (d) sintered  $\text{B}_4\text{C}$ -5vol.% $\text{Eu}_2\text{O}_3$  composite and (e) sintered  $\text{B}_4\text{C}$ -10vol.%  $\text{Eu}_2\text{O}_3$  composite. All the samples are sintered in vacuum at  $1900^\circ\text{C}$  for 15 minutes using SPS route**

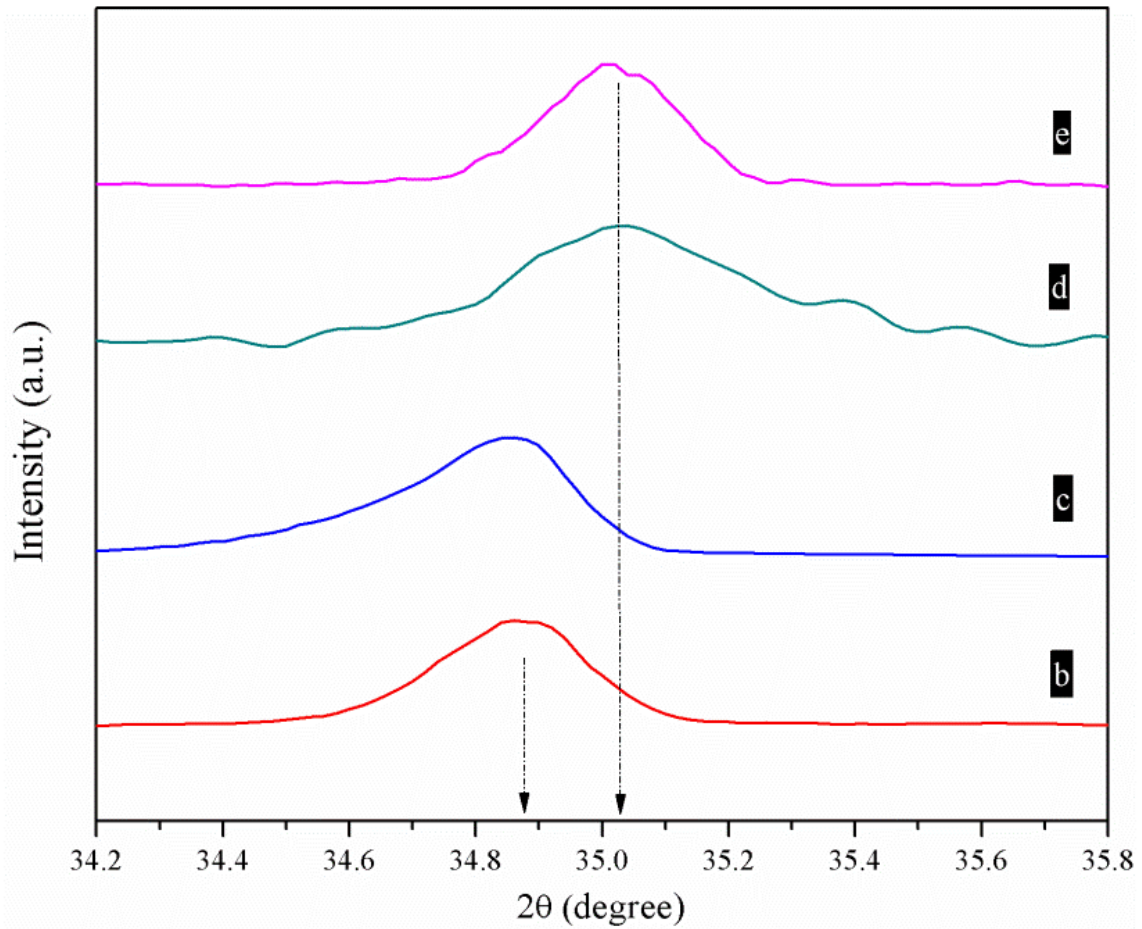


**Fig. 4.3: (ii) X-ray diffraction peaks corresponds to (104) plane of B<sub>4</sub>C phase to illustrate peak shift in B<sub>4</sub>C-5vol.% Eu<sub>2</sub>O<sub>3</sub> and B<sub>4</sub>C-10vol.% Eu<sub>2</sub>O<sub>3</sub> composite towards higher angle with respect to the monolithic B<sub>4</sub>C**

**TABLE 4.2: Phase assemblage of Spark Plasma Sintered B<sub>4</sub>C-Eu<sub>2</sub>O<sub>3</sub> composite samples**

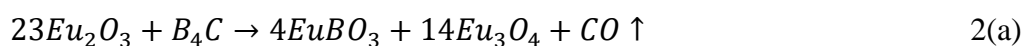
Starting composition	Processing temperature (°C)	Dwell time (min)	Phases identified
B <sub>4</sub> C+5vol.%Eu <sub>2</sub> O <sub>3</sub>	1900	15	B <sub>4</sub> C and EuB <sub>6</sub>
B <sub>4</sub> C+10vol.%Eu <sub>2</sub> O <sub>3</sub>	1900	15	B <sub>4</sub> C and EuB <sub>6</sub>

Theoretical analysis shows that the complete conversion as per reaction (1) can lead to final sintered composition as B<sub>4</sub>C-9 vol% EuB<sub>6</sub> and B<sub>4</sub>C-18 vol% EuB<sub>6</sub>, corresponding to B<sub>4</sub>C-5 vol% Eu<sub>2</sub>O<sub>3</sub> and B<sub>4</sub>C-10vol% Eu<sub>2</sub>O<sub>3</sub> powder mixtures. This was re-confirmed using Image-J analysis of random microstructures of sintered compacts.

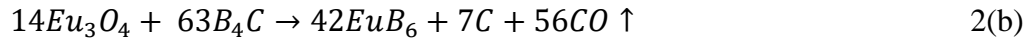
Figure 4.3(ii) shows the X-ray diffraction peaks corresponding to (104) plane of B<sub>4</sub>C phase, illustrating variation of peak position in different compositions. In comparison to monolithic B<sub>4</sub>C, X-ray diffraction peak corresponding to B<sub>4</sub>C phase in sintered B<sub>4</sub>C-Eu<sub>2</sub>O<sub>3</sub> composite exhibited a peak shift towards higher angle, which signifies the deviations in the chemistry of stoichiometric B<sub>4</sub>C phase. The peak shift corresponding to (104) plane was measured to be 0.16°(2θ) in B<sub>4</sub>C-10 vol% Eu<sub>2</sub>O<sub>3</sub> composite.

### 4.3 EuB<sub>6</sub> Formation: Reaction Mechanism

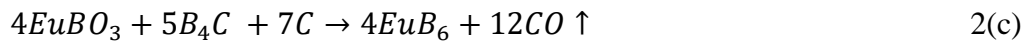
Based on weight loss measurement data (TG-DTA) and the reaction products identified in samples processed under different conditions, it is logical to attribute chemical reaction (1) to occur in different steps. The formation of EuB<sub>6</sub> in sintered microstructure can be explained via two independent reaction pathways. It is quite likely that both the pathways can take place concurrently during sintering of B<sub>4</sub>C-Eu<sub>2</sub>O<sub>3</sub> powder compacts. In the backdrop of Figure 4.2, it is appropriate to explain the formation of EuBO<sub>3</sub> and Eu<sub>3</sub>O<sub>4</sub> as intermediate reaction products. It is to consider that Eu<sub>3</sub>O<sub>4</sub> and EuBO<sub>3</sub> formation can be rationalized using the reaction between Eu<sub>2</sub>O<sub>3</sub> and B<sub>4</sub>C (reaction 2a).



In the reaction pathway involving  $\text{Eu}_3\text{O}_4$ , the next possible sintering reaction would involve  $\text{Eu}_3\text{O}_4$  and  $\text{B}_4\text{C}$ , which would lead to  $\text{EuB}_6$  and free carbon formation with the release of  $\text{CO}$  (reaction 2b).



$\text{EuBO}_3$  can independently react with  $\text{B}_4\text{C}$  and free carbon to form  $\text{EuB}_6$  as per the reaction (2c).



The presence of oxide layers is commonly reported for other non-oxide powders and their presence expectedly influences the nature of sintering reactions. Alternative to reaction 2(a), the formation of  $\text{EuBO}_3$  can be explained by considering the presence of thin oxide layer ( $\text{B}_2\text{O}_3$ ) on  $\text{B}_4\text{C}$  powders as per the following reaction



In view of the non-availability of the thermodynamic data for  $\text{EuBO}_3/\text{EuB}_6$ , the energetics of the above reactions could not be further assessed. It is worth to mention here that unlike transition metal oxides, rare earth oxide ( $\text{Eu}_2\text{O}_3$ ) reacts with  $\text{B}_4\text{C}$  in multiple stages as mentioned in reactions 2(a)-(c). At high temperatures, reaction between  $\text{B}_4\text{C}$  and transition metal oxides (e.g.  $\text{TiO}_2$ ,  $\text{ZrO}_2$ ) is reported to occur in single step with the formation of

transition metal boride.<sup>[17]</sup> For example the following reaction is considered for the formation of HfB<sub>2</sub> phase.



---

## Chapter 5: Results and Discussions

### (Sintering and Microstructure)

---

Boron carbide and europium oxide added (5 and 10 vol.%) boron carbide powders have been consolidated by spark plasma sintering. The influence of spark plasma sintering parameters on densification of pure B<sub>4</sub>C has been studied and sintering parameters have been established to get near theoretical dense monolithic B<sub>4</sub>C. Thereafter, B<sub>4</sub>C-5 vol.%Eu<sub>2</sub>O<sub>3</sub> and B<sub>4</sub>C-10 vol.%Eu<sub>2</sub>O<sub>3</sub> composite powders have been sintered under identical conditions. As discussed in previous chapter the sintered products will be B<sub>4</sub>C-EuB<sub>6</sub> composite. Theoretical calculations show that the composites obtained by sintering B<sub>4</sub>C-5 vol.%Eu<sub>2</sub>O<sub>3</sub> and B<sub>4</sub>C-10 vol.%Eu<sub>2</sub>O<sub>3</sub> composite powders will have 9 and 18 vol% EuB<sub>6</sub> phase respectively. Microstructure development in B<sub>4</sub>C-18 vol% EuB<sub>6</sub> composite has been discussed in detail.

#### 5.1. Effect of Temperature on densification of B<sub>4</sub>C

Fig. 5.1 represents the plot of shrinkage measured in spark plasma sintered B<sub>4</sub>C samples as a function of processing temperature. The sinterability of boron carbide increases with increase in temperature and reaches near theoretical density at 1800°C. Three different stages were observed in the densification within the temperature range 1100°C-1800°C (Fig. 5.1).

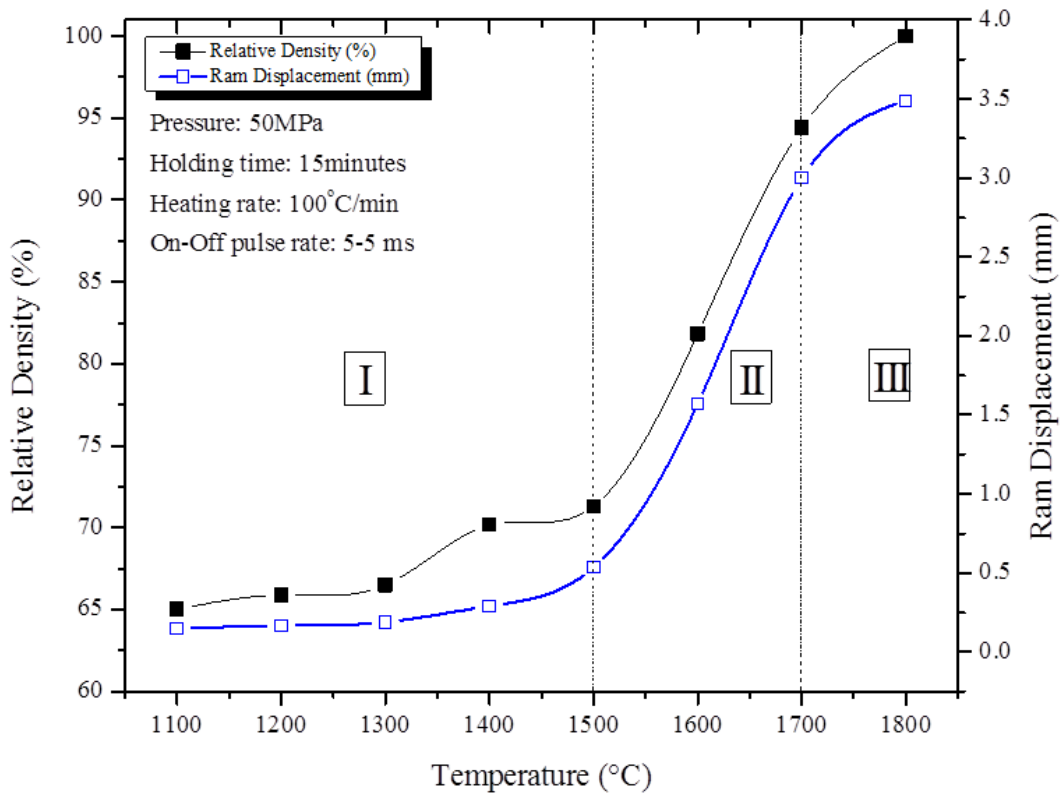


**Fig.5.1 Relative density and Shrinkage of Spark Plasma Sintered B<sub>4</sub>C samples as a function of Processing Temperatures.**

Densification behaviour of B<sub>4</sub>C was found to be sluggish up to 1500°C which represents the first stage of sintering. A sudden increase in density at 1500°C implies the onset temperature for rapid densification of B<sub>4</sub>C which is in good agreement with the reported literature data. <sup>[19]</sup> The second stage (1500°C-1700°C) was found to play a dominant role in the densification of B<sub>4</sub>C as the slope of densification plot is steeper which infers higher shrinkage. 94.4%  $\rho_{th}$  density was obtained at 1700°C. Third or final stage of densification was associated with the elimination of residual porosities and reaches full density at 1800°C but at a rate slower than that observed in the second stage.

Passing of high current of the order of 800-1500A causes direct heating of the powders based on Joule's heating. <sup>[19, 23]</sup> The contact points between the particles offer high resistance to the current flow and contribute for increased heating. The temperatures at those localized heating zones would exceed the melting temperature of the material and the cumulative effect from all such zones results in increased densification at comparatively lower sintering temperatures and shorter duration than conventional sintering techniques. Table 5.1(a)-(b) shows the summary of relative densities of various monolithic B<sub>4</sub>C samples obtained by spark plasma sintering.

**Table 5.1(a). Processing conditions and Mechanical properties of spark plasma sintered monolithic boron carbide.**

<b>Temperature (°C)</b>	<b>Holding time (minutes)</b>	<b>Pressure (MPa)</b>	<b>ON-OFF Pulse Sequence (milliseconds)</b>	<b>Relative Density (%)</b>
<b>1600</b>	<b>15</b>	<b>50</b>	<b>100-1</b>	<b>81</b>
<b>1600</b>			<b>50-1</b>	<b>81.5</b>
<b>1600</b>			<b>10-1</b>	<b>82.7</b>
<b>1600</b>			<b>5-5</b>	<b>81.8</b>

**Table 5.1(b). Relative densities of B<sub>4</sub>C samples obtained by spark plasma sintering at different temperatures**

Temperature (°C)	Applied pressure (MPa)	Holding time (minutes)	ON-OFF Pulse Sequence (milliseconds)	Relative Density (%)
1100	50	15	5-5	65.0 ± 1
1200				65.8 ± 1.5
1300				66.5 ± 0.5
1400				70.5 ± 0.5
1500				71.8 ± 0.4
1600				81.8 ± 0.4
1700				94.4 ± 0.4
1800				> 99.9

Ram displacement of SPS was monitored and tracked during the sintering experiments, which also indicates three stages of displacement which is in correlation with that of densification plot (Fig. 5.1). As the top ram is static, any relative displacement of bottom ram along positive or negative direction from its initial position corresponds to contraction or expansion of the material, respectively. The net displacement observed during processing of B<sub>4</sub>C samples includes shrinkage from loaded powders and expansion of graphite plunger due to heating. The calibration experiment was performed under identical processing conditions using full dense B<sub>4</sub>C pellet instead of powder. The true shrinkage behaviour of B<sub>4</sub>C samples was determined by alleviating the effects that arising from the thermal expansion of graphite plungers.

Fig.5.2 shows representative ram displacements corresponding to the SPS operation sequence for the temperatures 1400°C, 1600°C and 1800°C. The operation sequence was classified as (a) holding and (b) cooling period. The B<sub>4</sub>C powder sample sintered at 1800°C reveals the linear ram displacement in positive direction that represents continuous shrinkage behavior

during the soaking period. The net relative displacement at 1800°C was 3.49 mm that represents the shrinkage observed for fully dense B<sub>4</sub>C sample. The net shrinkage observed for B<sub>4</sub>C sample sintered at 1400°C was found to be very small, which is 0.25 mm that corresponds to the sample of relative density 70.5%  $\rho_{th}$ .

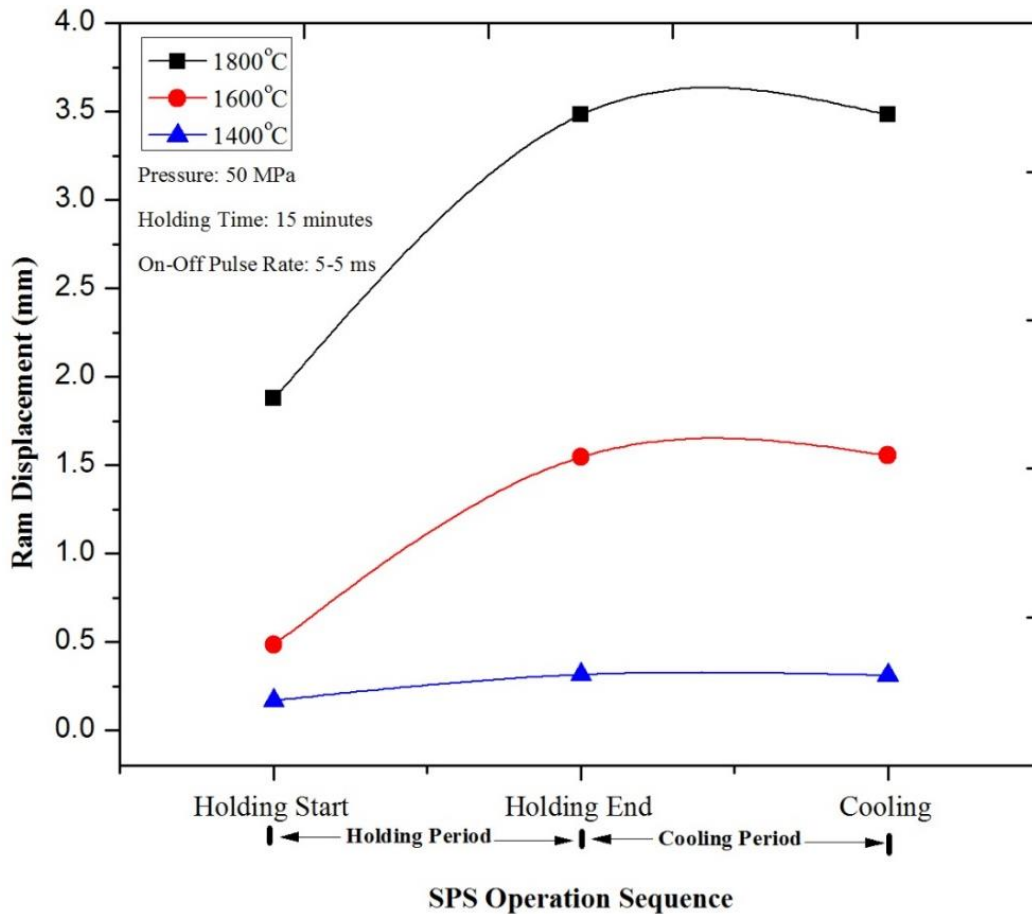


**Fig.5.2 Ram displacement observed at different processing temperatures is plotted as a function of SPS operation sequence (Holding Period and Cooling). \*Note that these curves do not represent the path of displacement; it is plotted by considering the initial and end position of Ram at different temperatures with respect to operation sequence.**

## 5.2 Effect of Holding Time on densification of B<sub>4</sub>C

Fig. 5.3 represents the evolution of B<sub>4</sub>C densification at 1800°C with respect to holding time (5, 10 and 15 min). The density was found to increase rapidly upon extending the holding or dwell time of sintering operation. It was observed that within 5 min duration, the density increased to 91% $\rho_{th}$  from 80% $\rho_{th}$  (Table 5.1a). This increase in sinterability is due to faster sintering kinetics under the influence of electric field. The electro-migration of ions was attributed to be the primary driving mode behind accelerating the kinetics of the diffusion process. <sup>[133]</sup> On further holding to 10 min, density was found to reach upto 96.6% $\rho_{th}$  but at a slower rate, as it involves the closure of intergranular porosities. Fully dense B<sub>4</sub>C was attained at the end of 15 min holding at 1800°C by spark plasma sintering. The density variation with respect to time at 1800°C is in good agreement with the net sample displacement observed (Fig. 9).D. Jianxin et.al.has obtained B<sub>4</sub>C of relative density 95.5% $\rho_{th}$  at 2150°C by hot-pressing for 1hr. <sup>[134]</sup> C. Subramanian et al carried out pressureless sintering of monolithic B<sub>4</sub>C and achieved a density close to 93% $\rho_{th}$  at 2375°C after 2 h. <sup>[13]</sup>

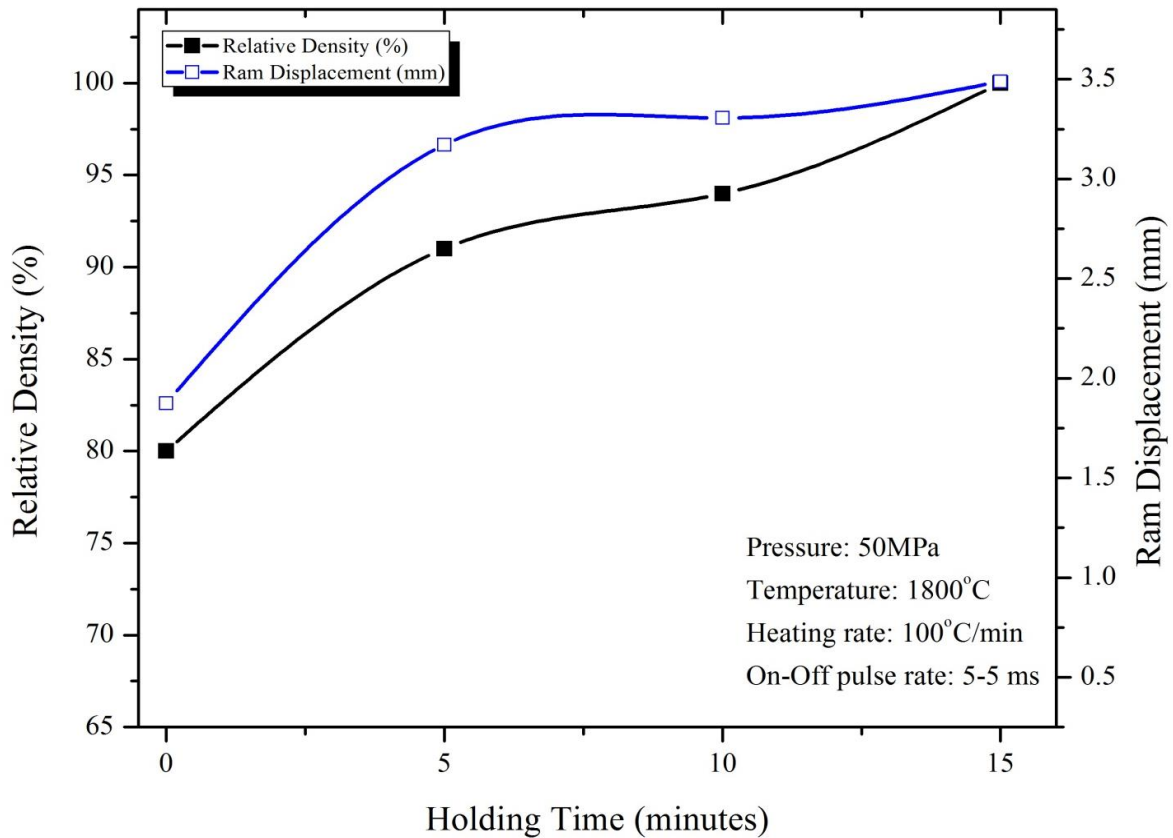


**Fig.5.3 Relative density and shrinkage of B<sub>4</sub>C sintered at 1800°C at different holding period (5, 10 and 15 min)**

### 5.3 Effect of Pulse rate on densification of B<sub>4</sub>C

The specific advantage of spark plasma sintering over conventional sintering techniques could be realized by the application of pulsed DC current during powder processing. ON-OFF pulse sequence was varied from 100-1, 50-1 and 10-1 (ms-ms) for B<sub>4</sub>C sample processed at 1600°C. The sample density prepared under 100-1 ms pulse sequence was found to be 81%  $\rho_{th}$  which increased to 82.7%  $\rho_{th}$  with 10-1 ms sequence (Fig. 5.4). This increase in densification with respect to pulse sequence could be explained based on pulse width and number of pulses per minute. Shorter the pulse width, larger the number of pulses that strikes, which in turn accelerates the diffusion of ions that are generated by discharge at the gap between the particles

surrounding the contact points. However, B<sub>4</sub>C sintered at 1600°C with 5-5 ms pulse sequence shows a density of 81.8% $\rho_{th}$ , which is slightly less than the density that was obtained with 10-1 pulse. This is due to longer OFF time (5 ms) implying (a) longer cooling period and (b) lower spark-impact effect which would not accelerate the sintering process. In the present study, the density obtained as a function of DC pulse rate is only marginally different and hence, it is difficult to draw a definite conclusion on the sintering mechanism based on the DC pulse rate operation. Further detailed investigation is needed on DC pulse rate effect on densification and should be addressed in future.

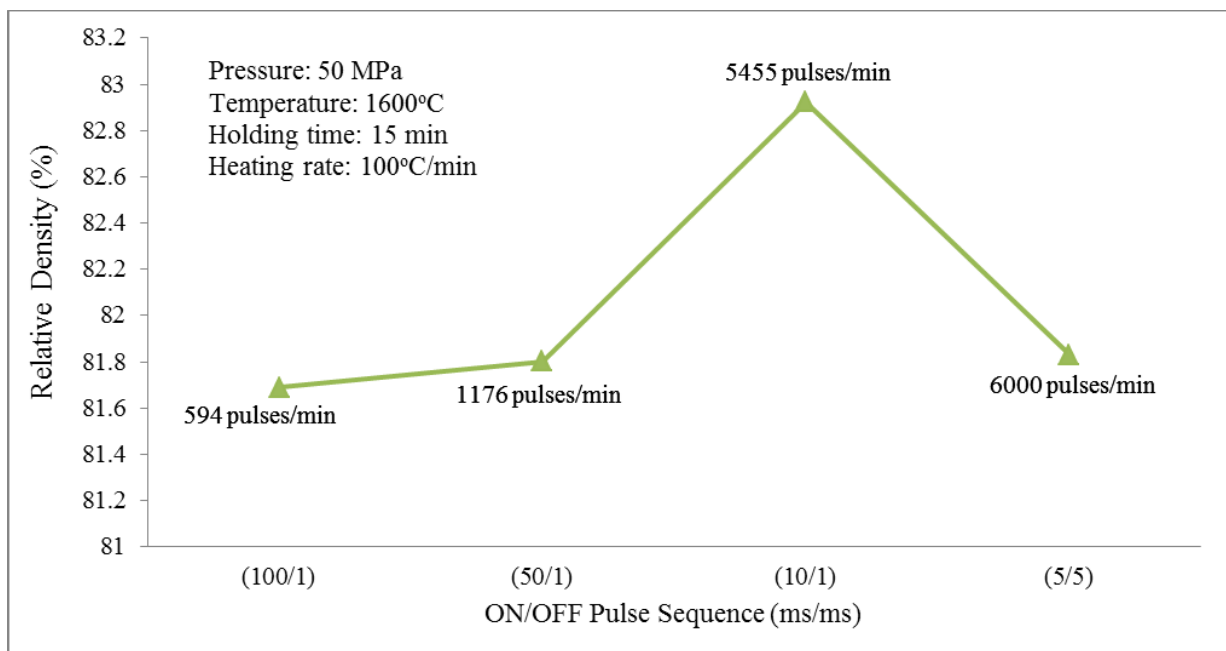


**Fig.5.4** Variation of Relative Density of Sintered B<sub>4</sub>C compacts at 1600°C as a function of DC Pulse Rate

## **5.4 Effect of Sinter-Aid (Eu<sub>2</sub>O<sub>3</sub>) addition on densification of B<sub>4</sub>C**

### **5.4.1 SPS Operation**

B<sub>4</sub>C powder was mixed with Eu<sub>2</sub>O<sub>3</sub> (0, 5 and 10 vol%) and the powder mixtures were milled in WC-lined planetary ball mill (Fristch, Germany) for 2h duration at 150 rpm using ethyl alcohol as wet medium. The heating rate was programmed at 100°C/min and all the samples were consolidated in vacuum at 1900°C for 15 min duration under the mechanical pressure of 45MPa. Spark plasma sintered compacts were ejected from the graphite die and graphite layers were removed from the surfaces.

### **5.4.2 Densification of B<sub>4</sub>C in the presence of Eu<sub>2</sub>O<sub>3</sub>**

Monolithic B<sub>4</sub>C, sintered at a temperature of 1900°C for 15 min, has a sinter density of 2.49 g.cm<sup>-3</sup> (~99.4%ρ<sub>th</sub>). Recently, A. Mukhopadhyay et al., has reported the formation of second phase TiB in spark plasma sintered TiB<sub>2</sub> ceramics. The reason for phase instability was explained based on accelerated reaction kinetics attained by the electric field in SPS. [135] We did not observe any such phase instability effect in B<sub>4</sub>C. XRD results (Fig. 5.5) confirmed the presence of only B<sub>4</sub>C peaks in both powder and final compacts. The relative density obtained for B<sub>4</sub>C is in good agreement with the previously reported density values under similar processing conditions. [24]

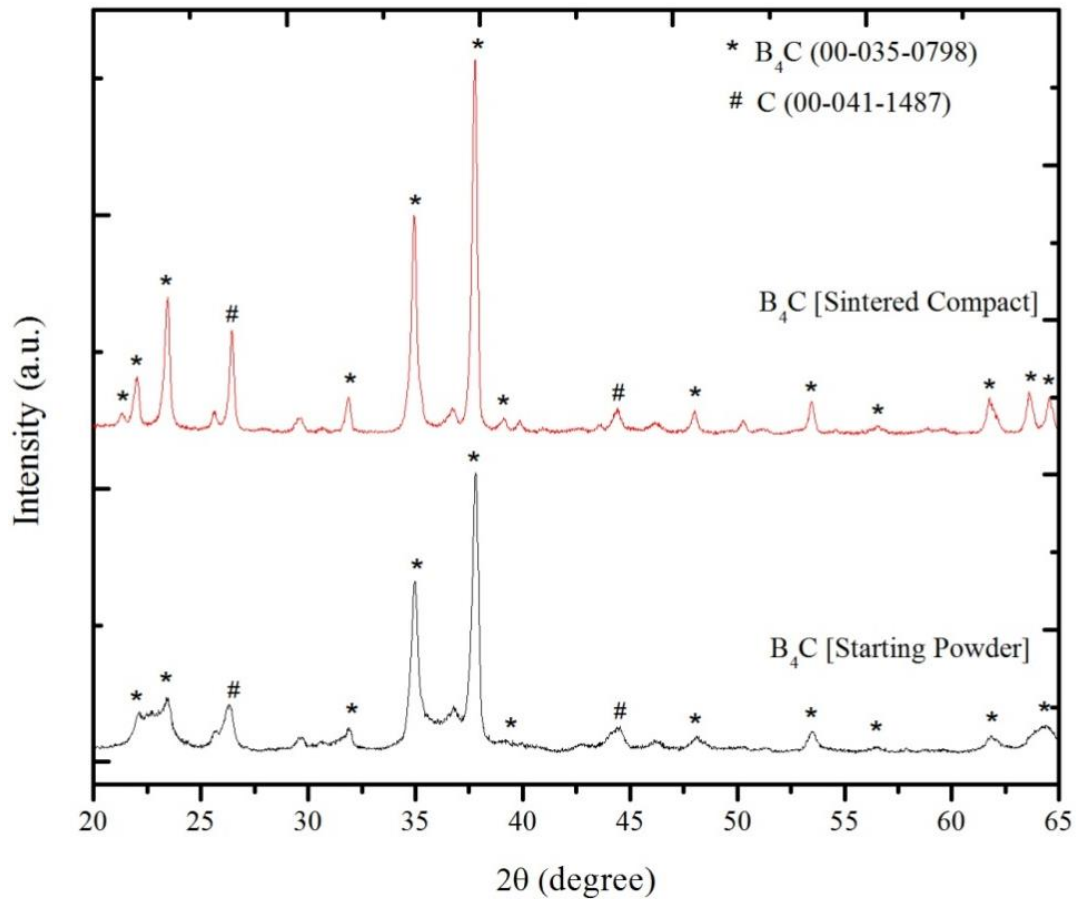


**Fig.5.5 XRD of starting  $B_4C$  powder and SPS processed full dense  $B_4C$  pellet**

The relative densities of  $B_4C$  sintered with 5 and 10 vol%  $Eu_2O_3$  were measured to be  $95\% \rho_{th}$  and  $94.1\% \rho_{th}$  respectively. Theoretical densities of composite mixtures were calculated based on considering the above-mentioned volume fractions of  $B_4C$  and  $EuB_6$  phases. The above trend in sinter density reflects the decrease in sintering aptitude of  $B_4C$  on increased addition of  $Eu_2O_3$ . Wei et al. has observed similar behaviour while sintering  $B_4C$  with  $Eu_2O_3$  addition.

[43]

### 5.4.3 Microstructural development during Spark Plasma Sintering of Monolithic B<sub>4</sub>C

Microstructural analysis (Fig. 5.6) of fully sintered B<sub>4</sub>C reveal the partially melted structures which is a direct evidence for localized heating mechanism that governs and dominates during spark plasma sintering process. Kalyanaraman et.al and Dipankar et.al. referred about the assistance of rapid localized heating towards lowering the sintering temperature in the plasma pressure compaction technique [136-137], which is in good agreement with the present observations.

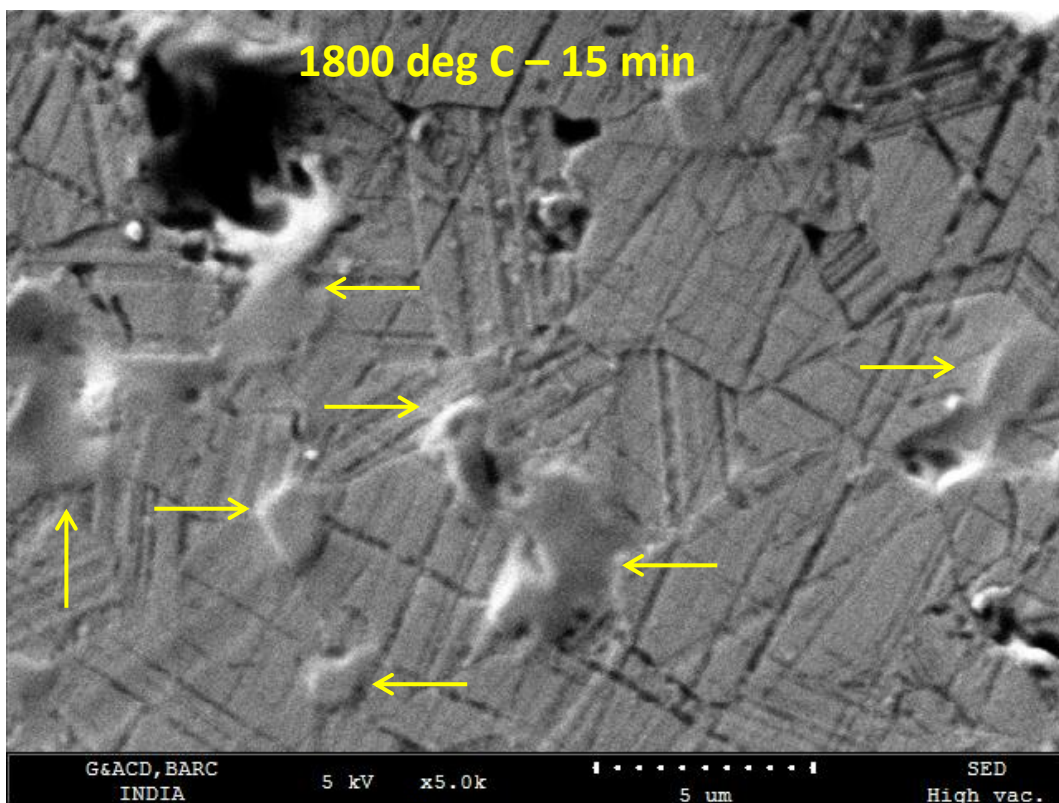


**Fig.5.6 Scanning Electron Micrograph of fully dense B<sub>4</sub>C compact processed at 1800°C for 15 min showing partially melted structures (indicated by arrow marks) and also reveals the presence of twin structures.**

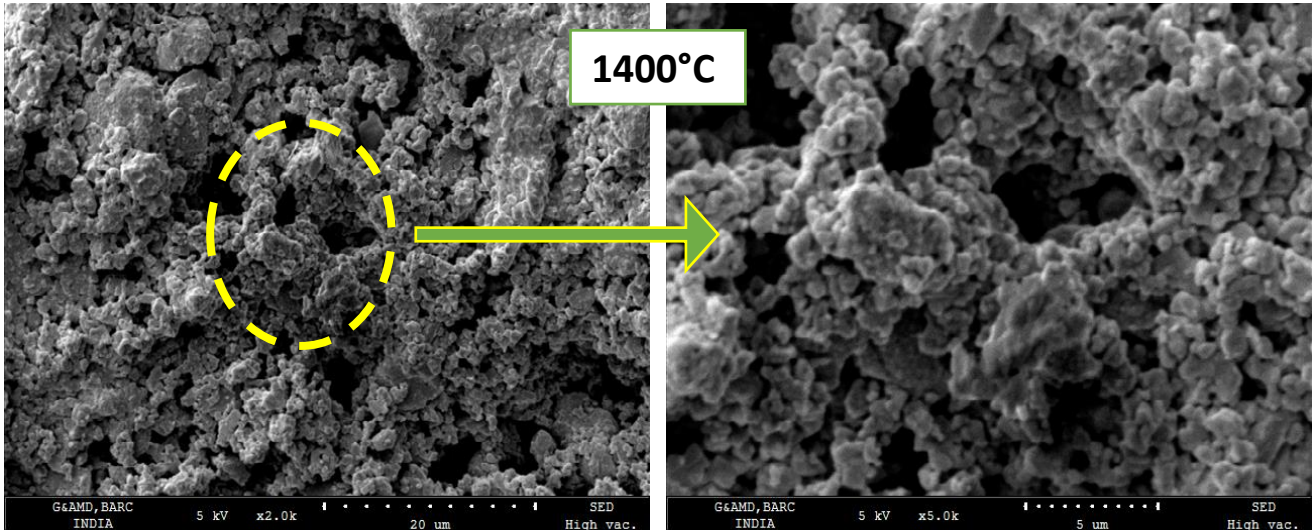


**Fig. 5.7a**

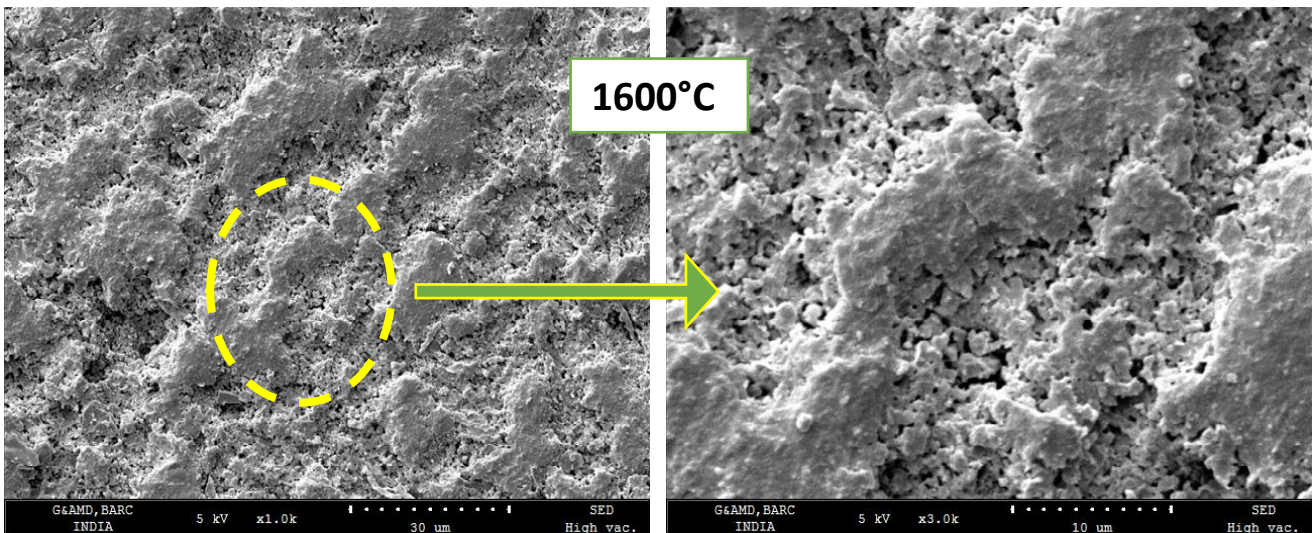


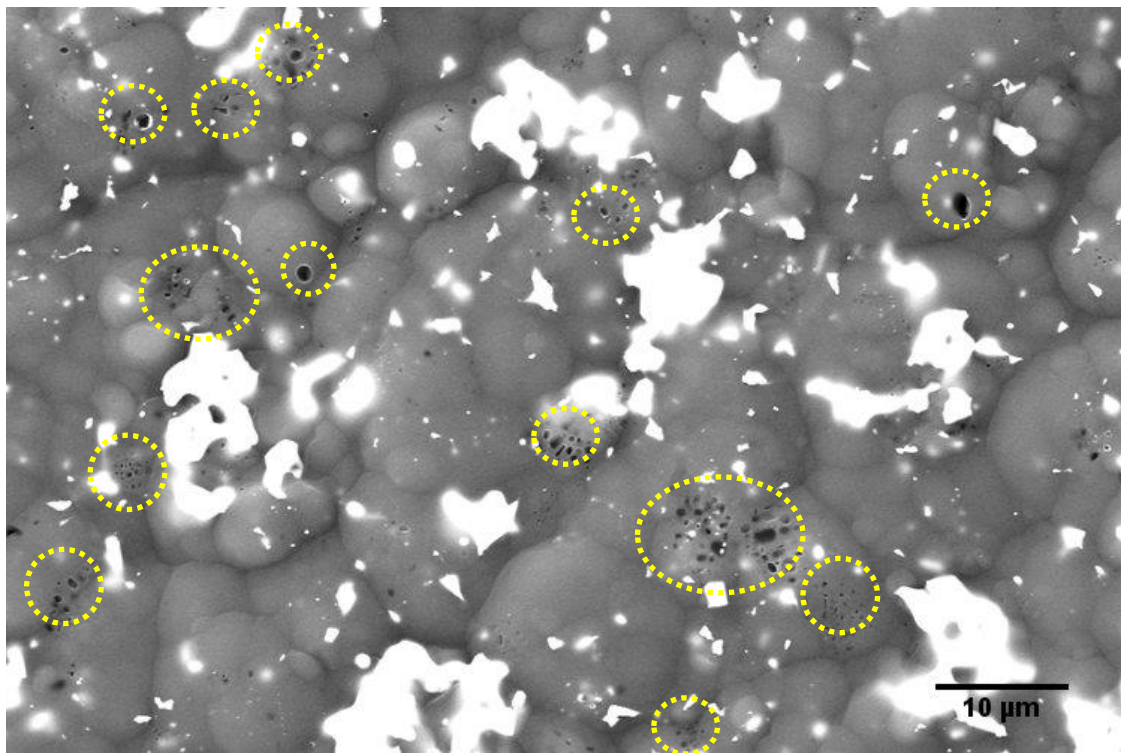
**Fig. 5.7b**

**Fig.5.7 (a)-(b) (a) Scanning Electron Micrographs of B<sub>4</sub>C processed at 1400°C shows open porosities and neck-like regions between the particles and (b) Micrograph of B<sub>4</sub>C processed at 1600°C indicates discrete densified regions with interconnected porosities.**

Fig.5.7 (a)-(b) shows the representative scanning electron microstructures of B<sub>4</sub>C sintered at 1400°C and 1600°C. SEM micrograph of B<sub>4</sub>C sintered at 1400°C clearly indicates the predominance of open porosities and the neck-like regions between particles. Formation of neck regions indicates the beginning of densification process that comprises the first stage of sintering. Microstructure of B<sub>4</sub>C processed at 1600°C show the patch of densified regions bounded with interconnected porosities. As discussed, Joules heating results in rapid rise in temperatures at localized regions that would contribute towards the formation of patches of densified regions. This fact represents the methodology or evolution of densification process in spark plasma sintering.

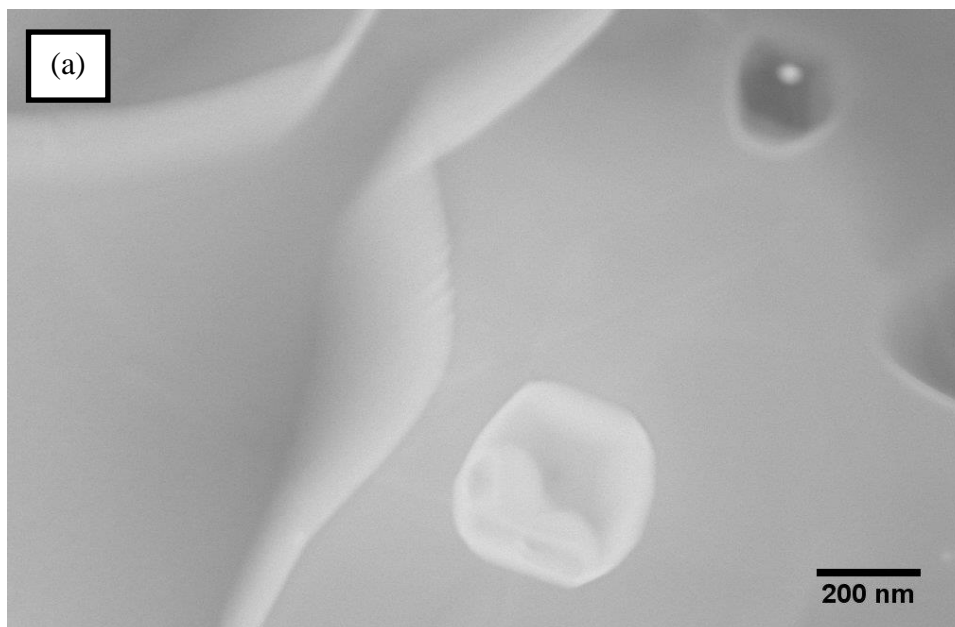
### 5.5 Microstructural characterization of B<sub>4</sub>C doped with Eu<sub>2</sub>O<sub>3</sub>

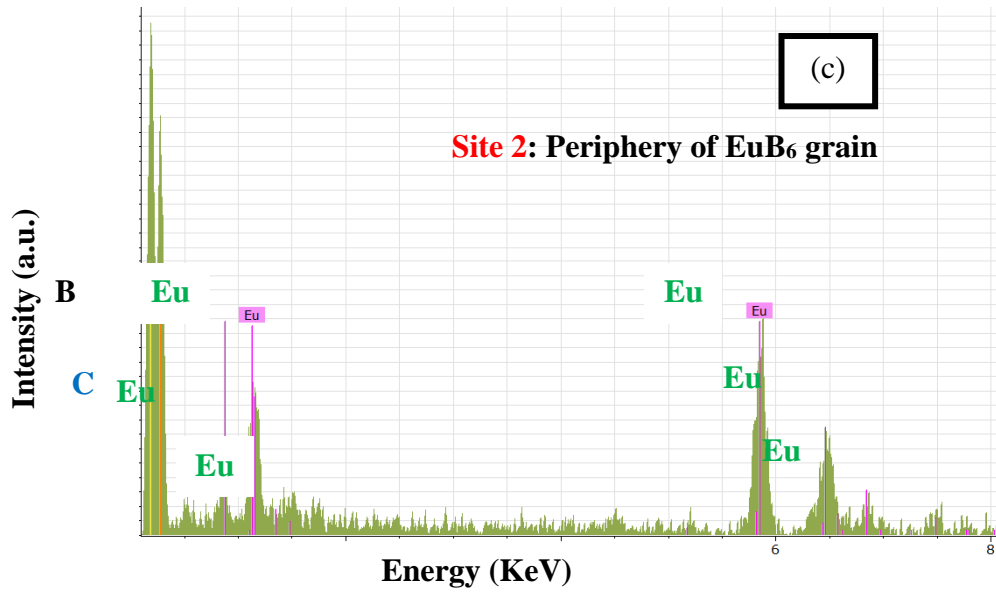
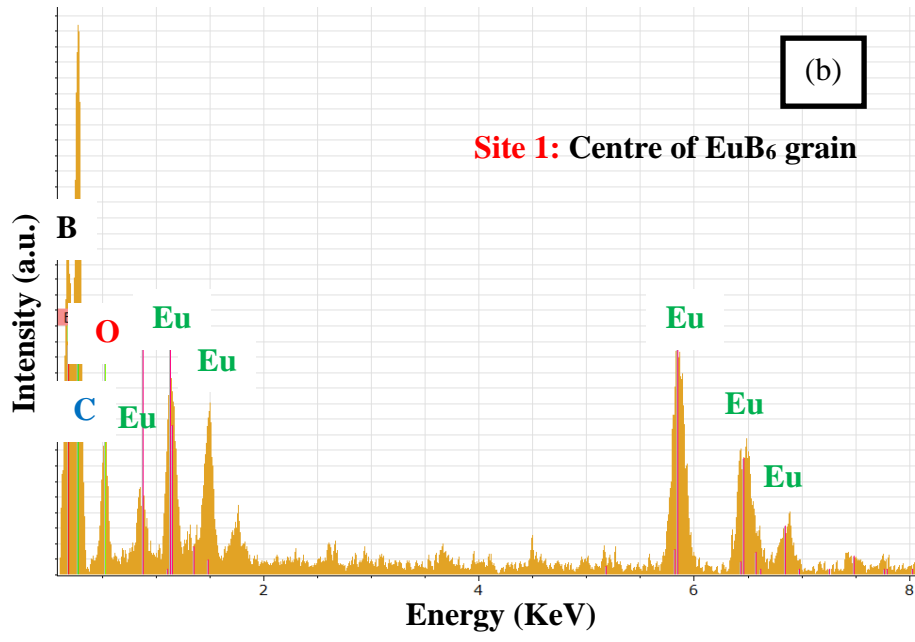
Secondary electron image (Figure 5.8) recorded with spark plasma sintered B<sub>4</sub>C-18vol%EuB<sub>6</sub> composite shows the presence of dark and bright regions, which correspond to B<sub>4</sub>C (matrix) and EuB<sub>6</sub> (reinforced phase), respectively. The encircled portions highlight the distribution of submicron pores within the matrix grains.

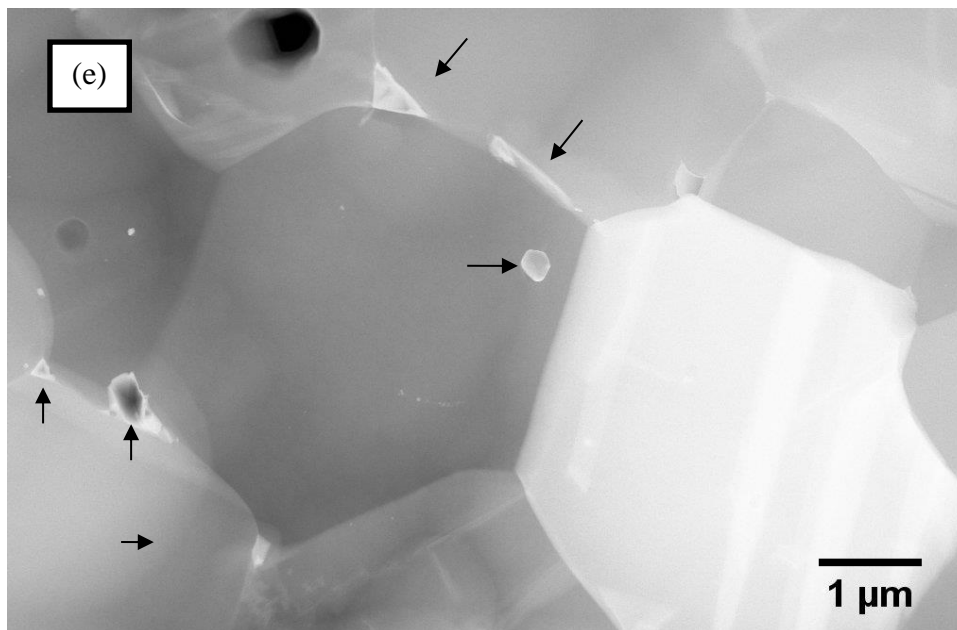
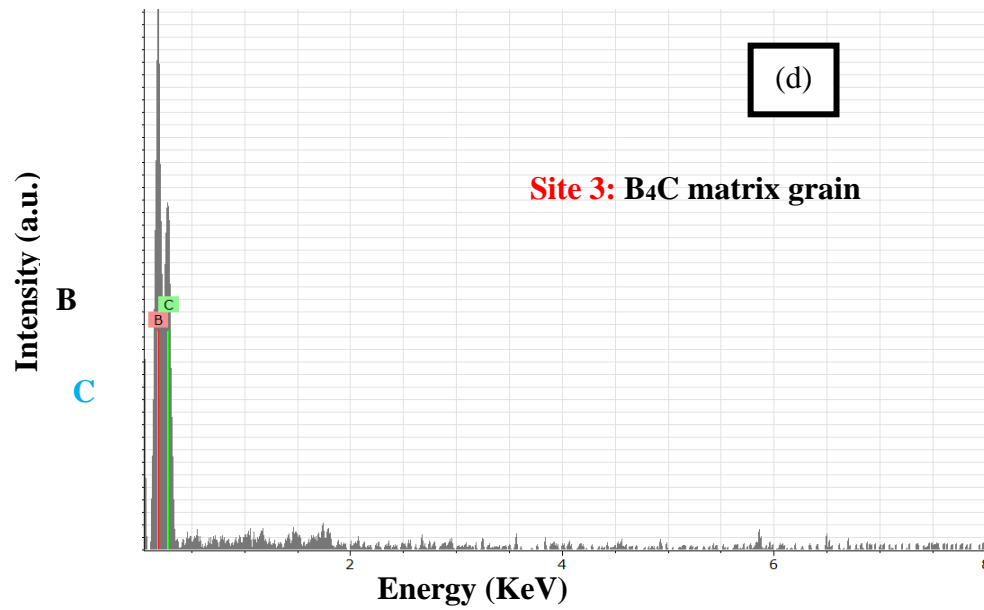


**Fig. 5.8** Secondary electron micrographs of spark plasma sintered B<sub>4</sub>C-18 vol.%EuB<sub>6</sub> composite. Highlighted portion indicates the distribution of submicron pores within the matrix grains.

Figure 5.9(a-b) shows the scanning transmission electron microstructures of  $B_4C$ - $EuB_6$  composites that indicate  $EuB_6$  particles at intra- and inter-granular locations. Intergranular  $EuB_6$  particles and fine size intragranular  $EuB_6$  particles were analyzed (EDS) to contain Eu and B. In case of slightly coarser intragranular  $EuB_6$  particles, the peripheral regions contain Eu and B and at its particle centre, it possessed Eu, B, C and O. The presence of oxygen at the centre of intragranular particle indicates the partial completion of reduction reaction (reaction 1, refer chapter 4). Also, in certain regions, intergranular phases contained carbon, in addition to Eu and B elements.  $EuB_6$  phase is reported to have some C solubility in its lattice structure. <sup>[44]</sup> Carbon solubility in  $EuB_6$  is localized and non-uniform, thus it becomes unnoticed in X-ray phase assemblage.

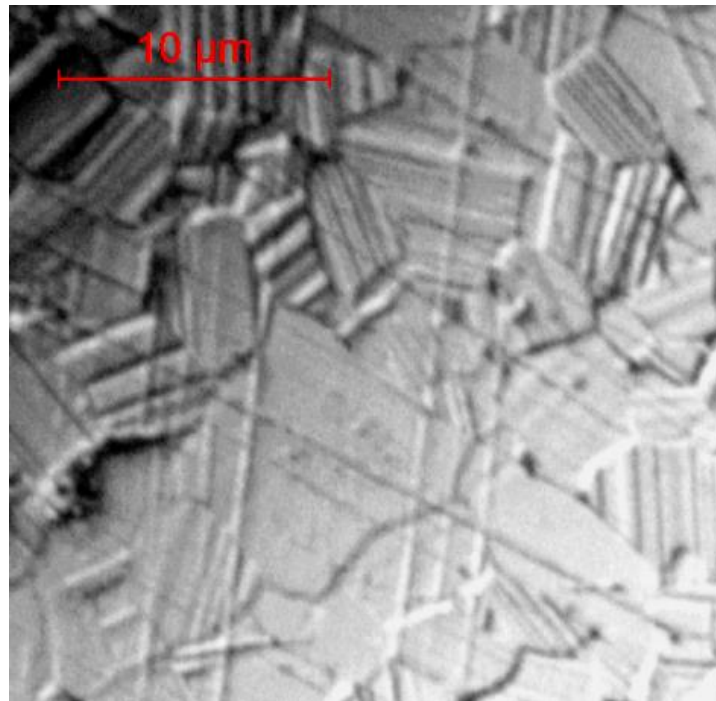




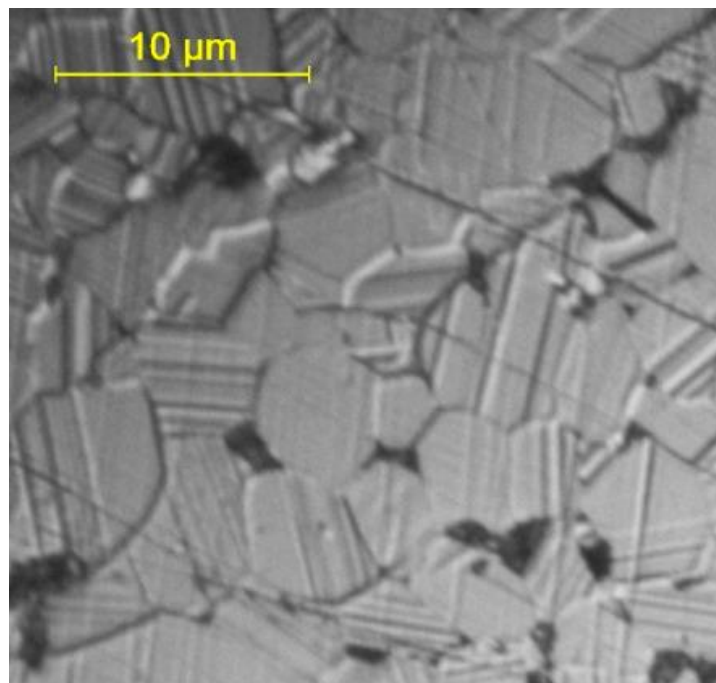


**Fig 5.9(a-e) Scanning transmission electron microstructures of B<sub>4</sub>C-EuB<sub>6</sub> composites showing EuB<sub>6</sub> particles at (a) intragranular and (e) intergranular locations as indicated by arrow marks. EDS Spectra (b) and (c) were recorded at centre and peripheral regions, respectively of intragranular EuB<sub>6</sub> particle. EDS Spectrum (d) was obtained at B<sub>4</sub>C matrix grain.**

## 5.6 Development of Twinned Microstructures during Spark Plasma Sintering of B<sub>4</sub>C



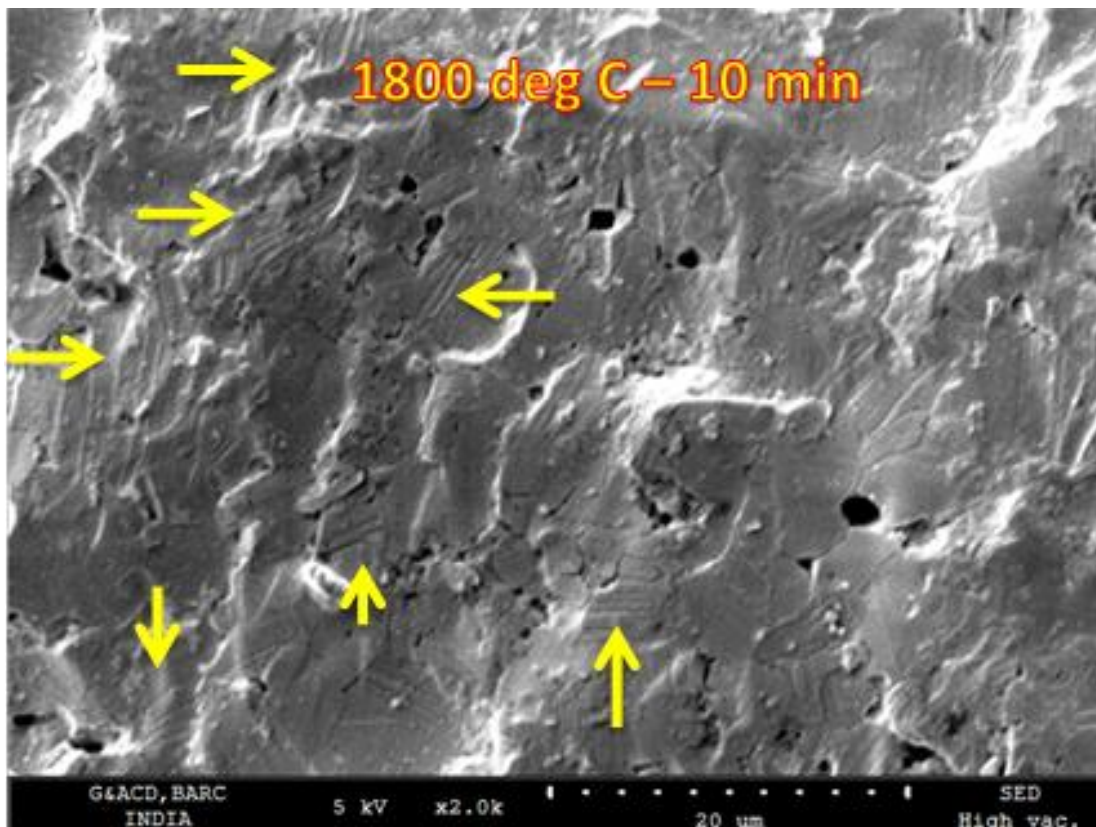
**Fig.5.10a**



**Fig.5.10b**

**Fig.5.10 (a) Optical microstructures of fully dense B<sub>4</sub>C (15 min) and b) 96.6% dense B<sub>4</sub>C compact sintered at 1800°C (10 min) showing the presence of twin boundaries.**

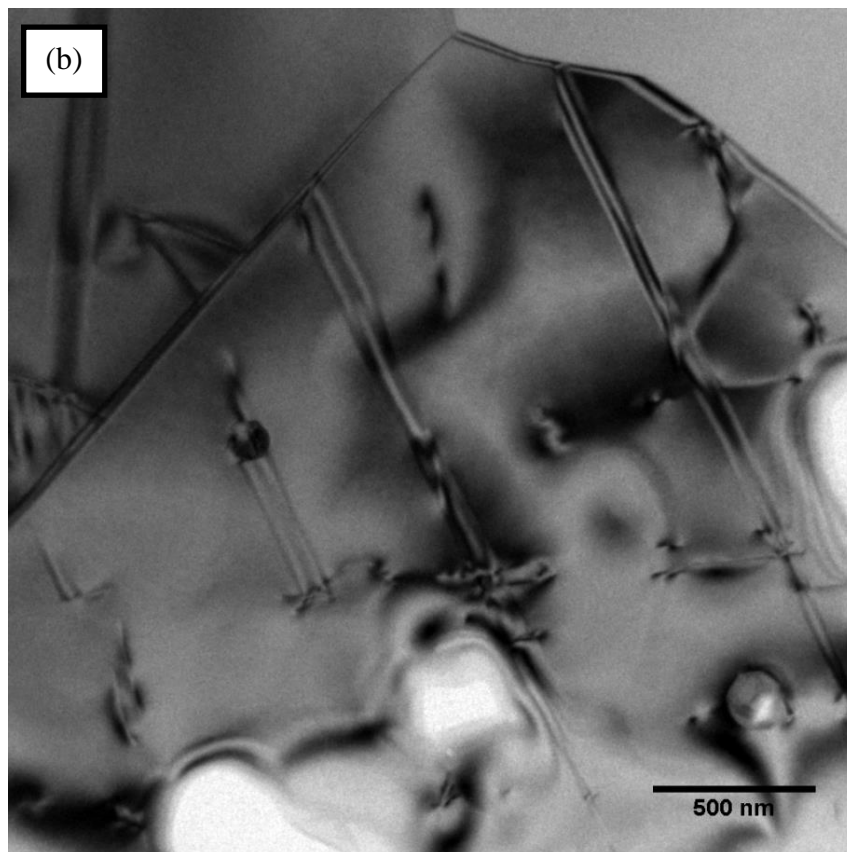
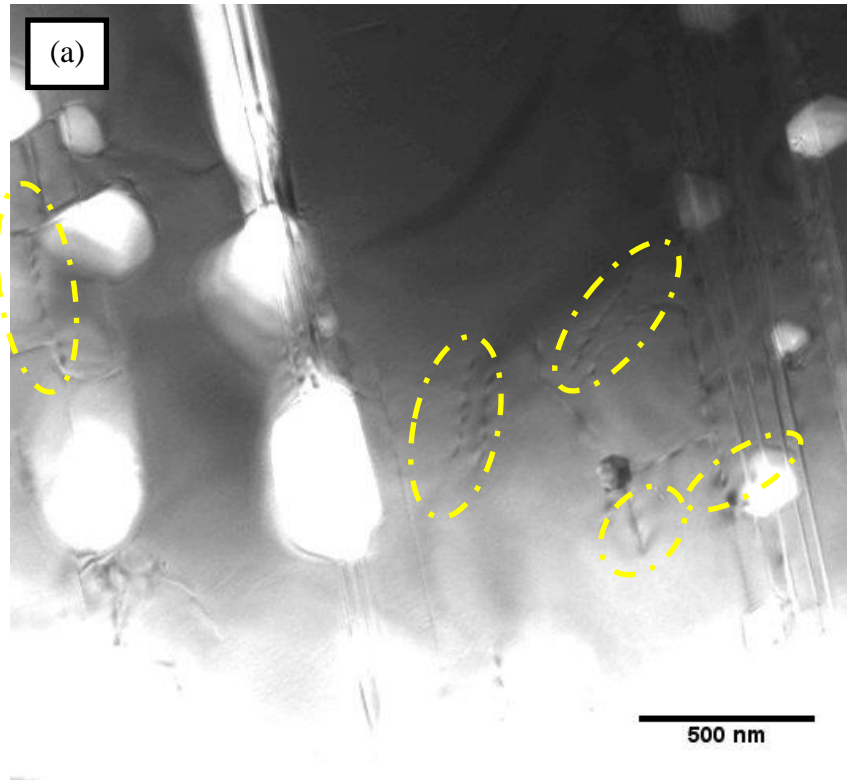
Fig. 5.10(a)-(b) shows the optical microstructures of etched  $B_4C$  show the average grain size of the order of 2-6  $\mu m$  which is close to mean particle size diameter (2.4  $\mu m$ ) of the starting powders. This clearly indicates that there is no grain coarsening during spark plasma sintering. Close observation of optical and scanning electron micrographs indicates the presence and predominance of twin structures (deformation twins) that are dividing the grains of  $B_4C$  (Fig. 5.6 and 5.10). Scanning electron microscopic image of fractured  $B_4C$  surface indicate the transgranular mode of fracture and also confirms the presence of deformation twins (Fig.5.11).



**Fig.5.11 Scanning Electron Micrograph of 96.6% dense  $B_4C$  fractured surface showing transgranular mode of fracture and also the presence of twin boundaries (indicated by arrow marks).**

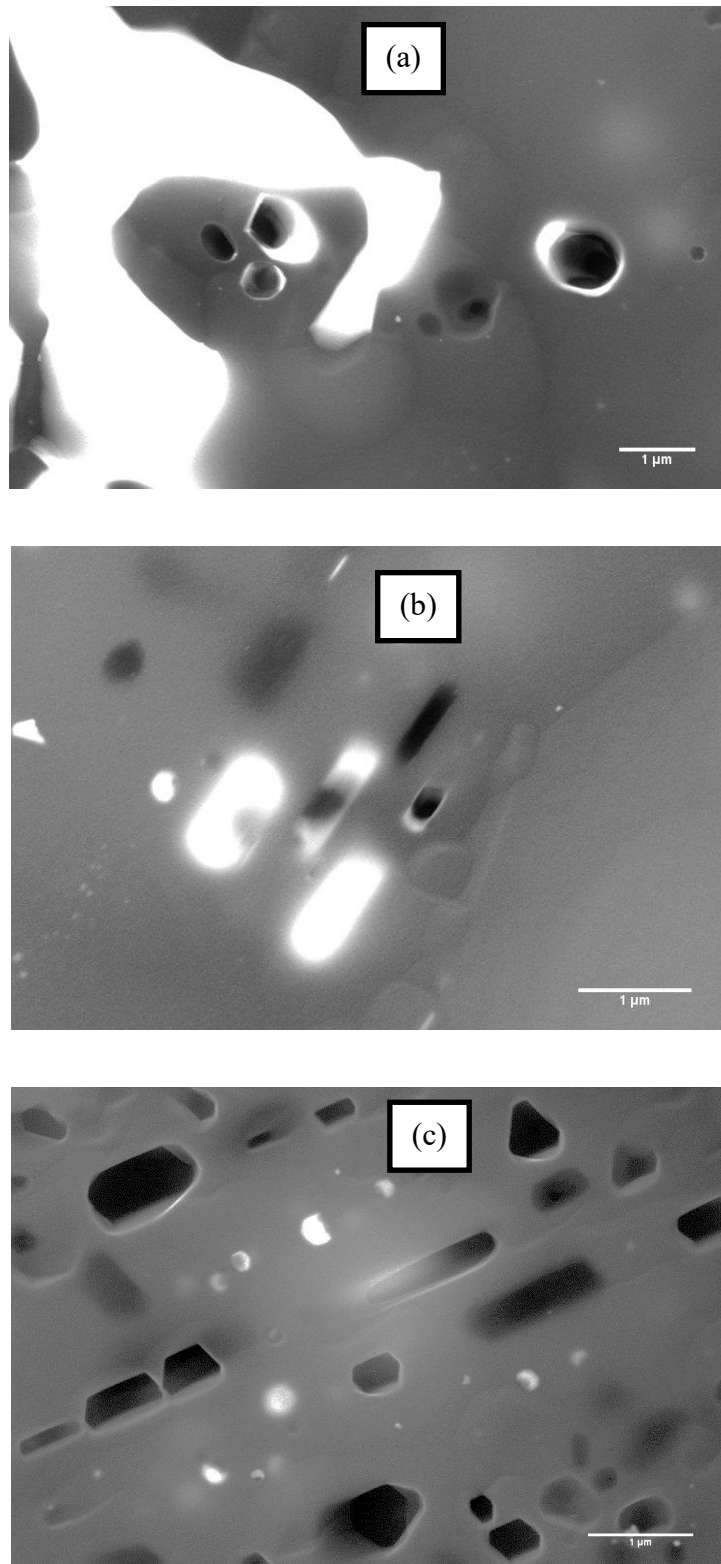
Twining in  $B_4C$  is reported to occur along rhombohedral planes of the type  $\{1011\}$  and  $\{1015\}$ .<sup>[138-139]</sup> In the present study, almost 70% of grains found to exhibit twin structures, which is significantly high compared to hot pressed  $B_4C$ .<sup>[114]</sup>

In addition to twin structures, BF-TEM images also indicate the presence of stacking fault regions and threaded dislocations in the  $B_4C$  matrix network (Figure 5.12(a-b)).



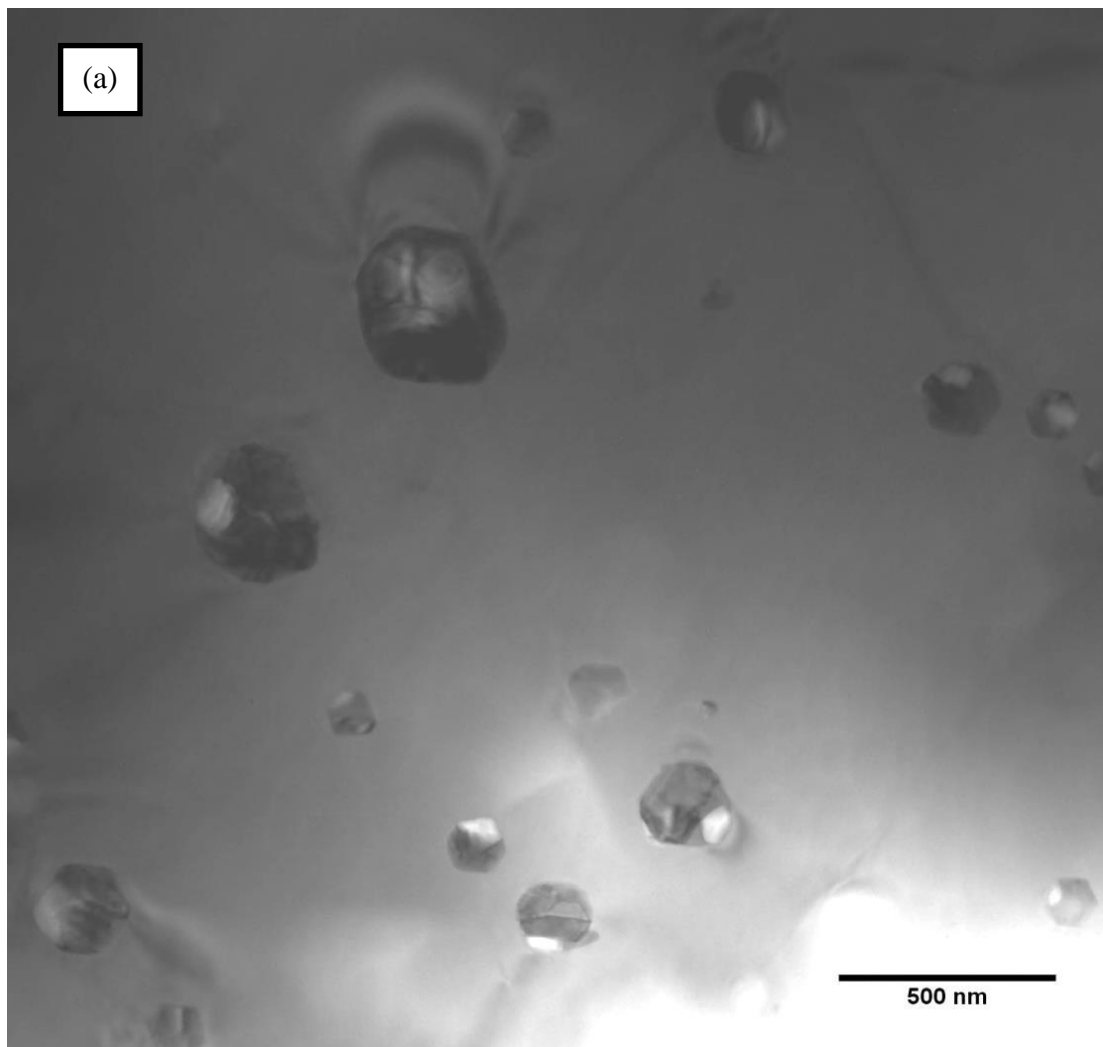
**Fig. 5.12 BF-TEM micrographs of  $B_4C$ -18 vol.% $EuB_6$  composite indicating the presence of (a) threaded dislocations and (b) stacking fault regions.**

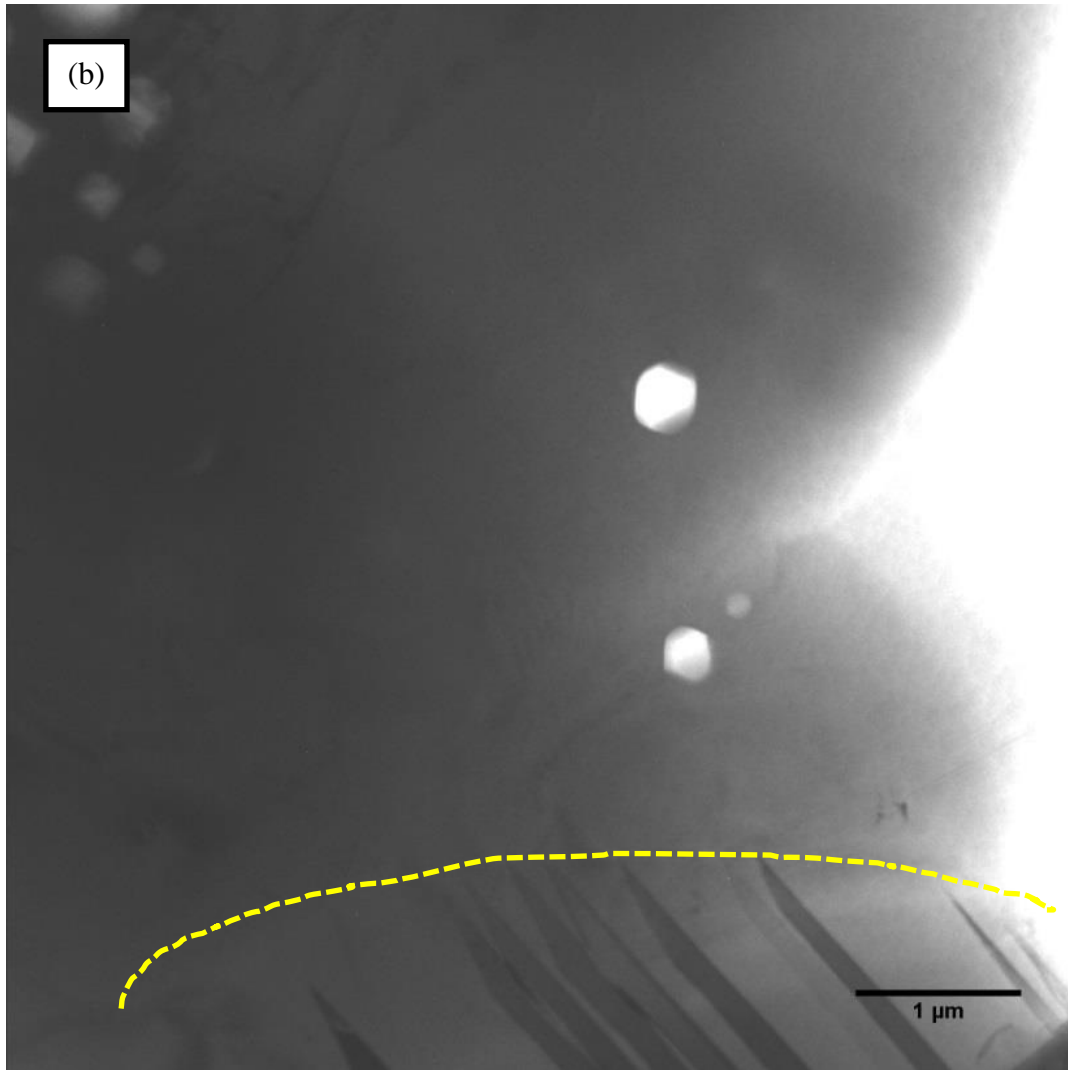
## 5.7 Role of Twin boundaries on Pores and Second Phase Morphology



**Fig. 5.13(a)-(c) FESEM microstructures of  $B_4C$ -18vol.% $EuB_6$  composite shows the distribution of  $EuB_6$  particles and submicron pores having different morphologies at the intragranular locations of  $B_4C$ .**

EuB<sub>6</sub> phases are found to be at intra and inter-granular locations of B<sub>4</sub>C grains. Both the pores and EuB<sub>6</sub> particles located at the intra-granular locations are found to vary in shape from spheroid to lath (Figure 5.13(a-c)). On closer inspection of microstructures, grains in B<sub>4</sub>C-18vol% EuB<sub>6</sub> composites can be classified into two factions (1) twin-free and (2) twinned regions. Note to readers: TEM diffraction patterns from the particles were obtained at different zone axis and by tilting the sample holder at angles  $\alpha$  (-40° to +40°) and  $\beta$  (-30° to +30°). During the TEM investigation, twin boundaries could not be detected in some B<sub>4</sub>C grains and those grains have been referred as “twin free” grains.

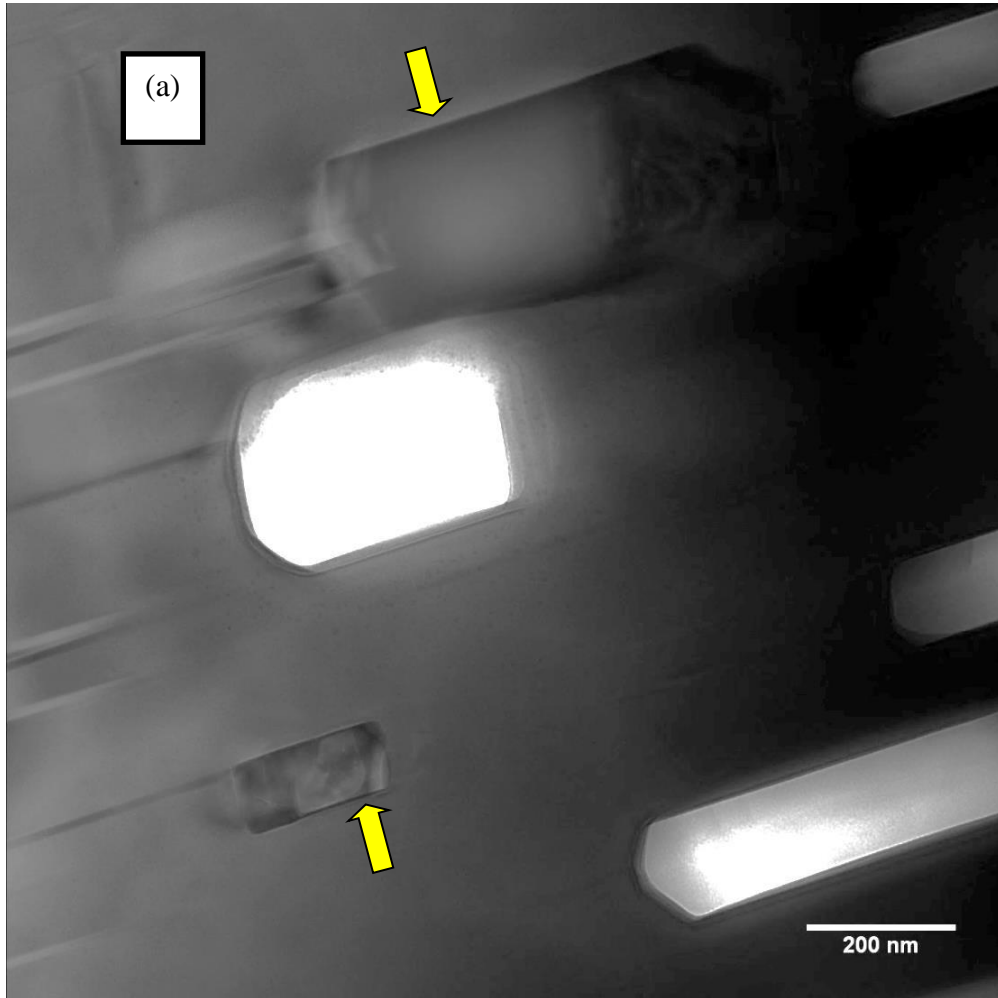




**Fig. 5.14 BF-TEM micrographs showing distribution of (a) spheroidal intragranular EuB<sub>6</sub> particles and (b) pores in twin-free regions.**

In twin-free grains (Figure 5.14(a-b)), the intra-granular pores and EuB<sub>6</sub> particles tend to exhibit mostly spheroid shapes; whereas in twinned grains (Figure 5.15(a-b)), they exhibited lath shaped morphologies. The average length-to-diameter ratio of lath-shaped pores and EuB<sub>6</sub> particles in twinned grains were evaluated to be 4 and 2.4, respectively. Similarly, the average diameter of pores and EuB<sub>6</sub> particles in twin-free grains is measured to be 4 μm and 2 μm, respectively. The pores in the twinned grain are identified to exhibit multi-angle faceting and

prism shaped decahedron. In twinned grains, apart from morphological features, the pores and  $\text{EuB}_6$  particles were tending to align parallel to the twin boundary direction in an ordered manner. In contrast, whereas the pores and  $\text{EuB}_6$  particles in twin-free grains do not exhibit such orientation characteristics.



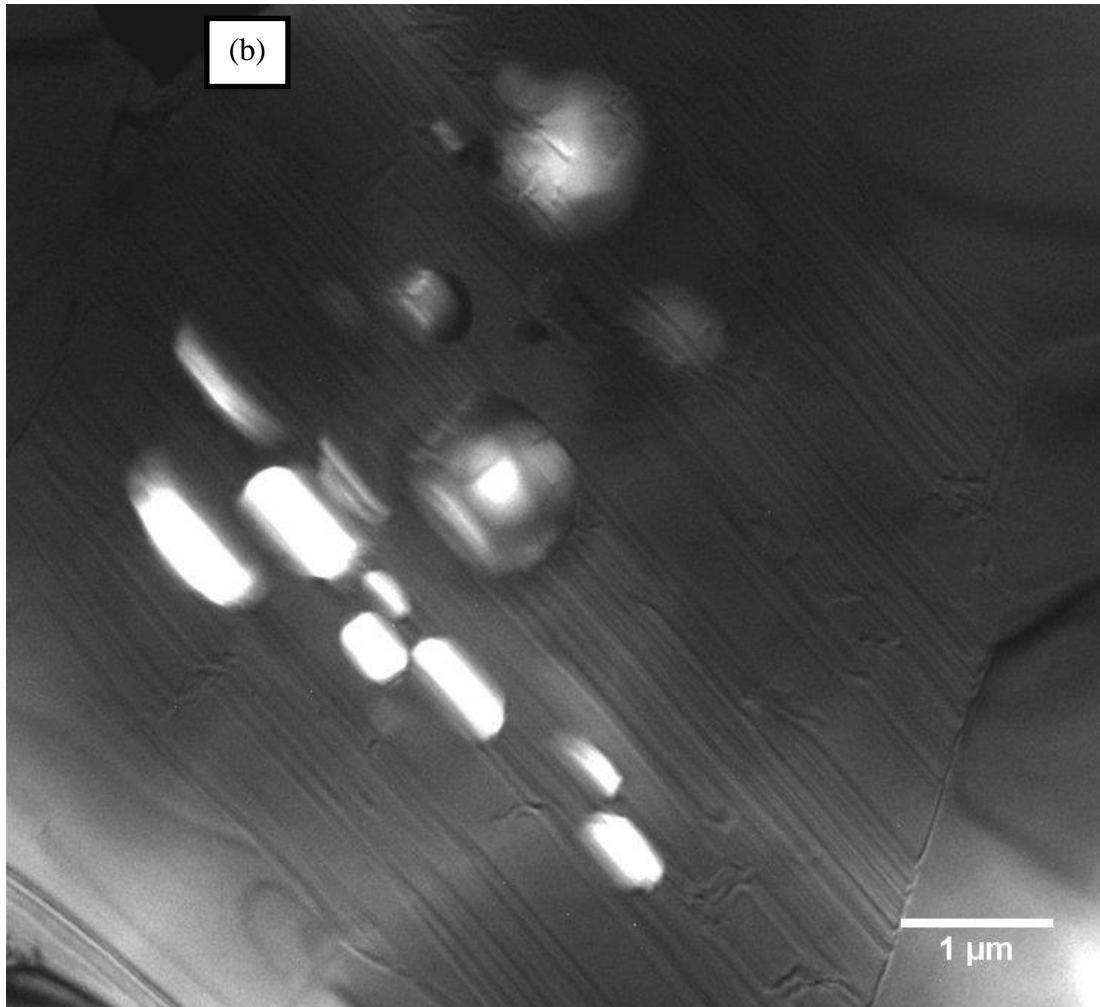


**Fig. 5.15 BF-TEM micrographs showing distribution of lath shaped and aligned (a) intragranular  $\text{EuB}_6$  particles (arrow marks) and (b) pores in twinned regions.**

In  $\text{B}_4\text{C}$ - $\text{EuB}_6$  composites, (twin-free)  $\text{B}_4\text{C}$  grains are devoid of twins both intra granular pores and  $\text{EuB}_6$  particles exhibit shape near to spheroids, based on least energy requirement. Whereas, in the presence of twin boundaries, the intragranular pores and  $\text{EuB}_6$  particles are characterised by regular faceted shapes having an aspect ratio of between 2 and 3. The pores having regular shapes with faceted sides are reported to indicate crystallographically controlled shapes. In addition to the explanation related to crystallographic control on pore shapes, it is

also reported as an indication of achieving equilibrium state between twins and pores. The presence of reinforced particles inside the matrix grain increases the interfacial energy of the grain. This excess energy could be minimized in the presence of twins, by orienting along the twin directions and by exhibiting defined shapes.

## **5.8 Correlation between Twin boundary development and SPS conditions**

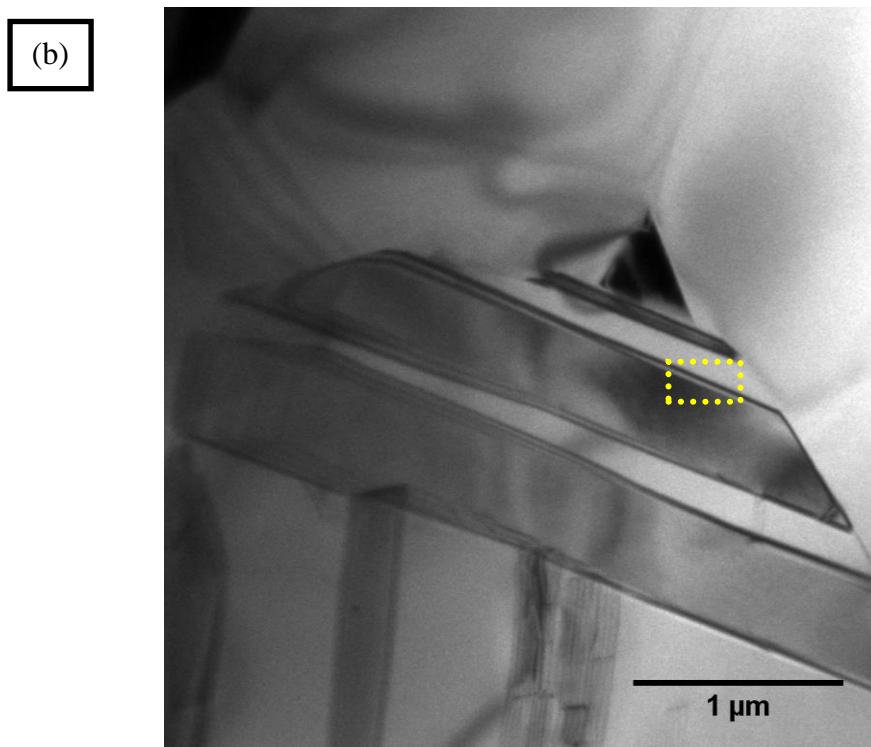
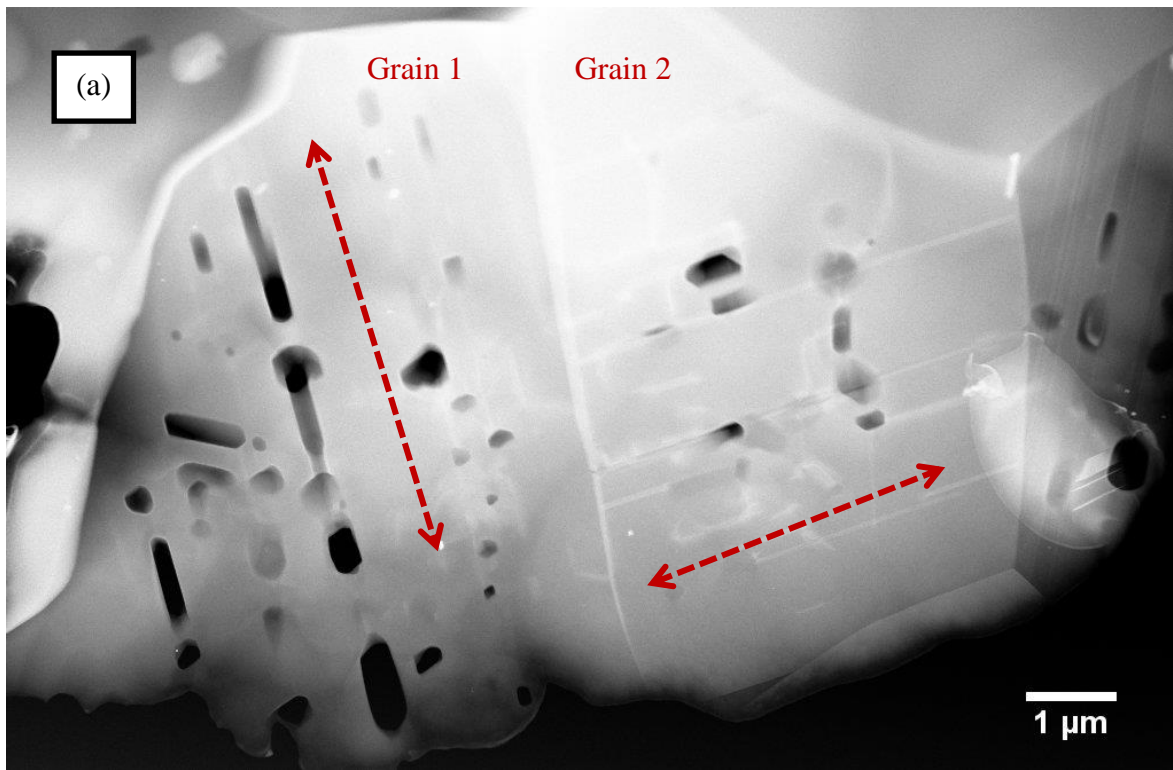
### **(Formation of Twin boundaries during SPS):**

The reason for increased twin density in the present study is explained by considering the spark plasma sintering operation. In SPS, the electric field accelerates the densification process and the simultaneous application of load during holding period, causes particle rearrangement and deformation. Deformation is a function of processing time, temperature and load. As the load increases, the stress at the particle contact points also increases, which enhances the sinterability of B<sub>4</sub>C by activating mass transport sintering mechanism <sup>[120]</sup> and also result in deformation. In order to minimize the excess energy available with the system, the energy in the form of external load would have focused largely on deformation of the particles apart from sintering. This deformation causes the displacement of atoms from its initial positions and contributes towards the formation of deformation twins. B<sub>4</sub>C sintered by SPS at 1800°C for 10 and 15 min found to exhibit deformation twins in it, whereas no noticeable twins were observed on B<sub>4</sub>C sample processed for 5 min at 1800°C. During the initial period (5 min) of sintering, the energy imparted to the system was consumed for densification process rather than on deformation, but further increase of holding period (10 and 15 min) causes the deformation. This infers the effect of processing time on the evolution of twin structures. In the present study, the samples with relative density greater than 94% $\rho_{th}$  show twin boundaries.

## 5.9 Effect of second phase on the nature of twin structures

Matrix grains of sintered  $B_4C$ -18 vol% $EuB_6$  composite were identified to contain predominance of twinned structures. The distribution of twin boundaries is random, where some grains contain few micro-twin bands and other contains both micro- and nano-twin structures together in the same grain (Figure 5.16(a-c)). Figure 5.16(c) shows the SAED pattern at the twin region observed in  $B_4C$ . The SAED pattern could be indexed with  $[0\bar{1}0]$  and  $[010]$  zone axis. On a closer observation of SAED pattern, the inclination angle between (101) and (003) planes differs by a value of  $\sim 1.8^\circ$  on either side of the boundary. This indicates that the lattices did not mirror perfectly with each other and based on the nature of planar defect, it was referred as asymmetric twins. <sup>[140]</sup> Asymmetric twin boundaries are reported to be influenced by  $B_4C$  stoichiometry and its atomic configurations. <sup>[141]</sup>

In the present study, during the course of reaction sintering, the formation of structural vacancies and the diffusion of constituent elements would alter the local atomic arrangements and thereby causes deviation from the stoichiometry of  $B_4C$  phase. The recorded peak shift in X-ray diffraction pattern is the signature of alteration in boron to carbon content in  $B_4C$  phase of  $B_4C$ - $EuB_6$  composite, which would have led to the formation of asymmetric twin boundaries (Chapter 4: Figure 4.3(ii)). Average thickness of twin bands was evaluated to be in the range of 0.5-1 $\mu$ m.



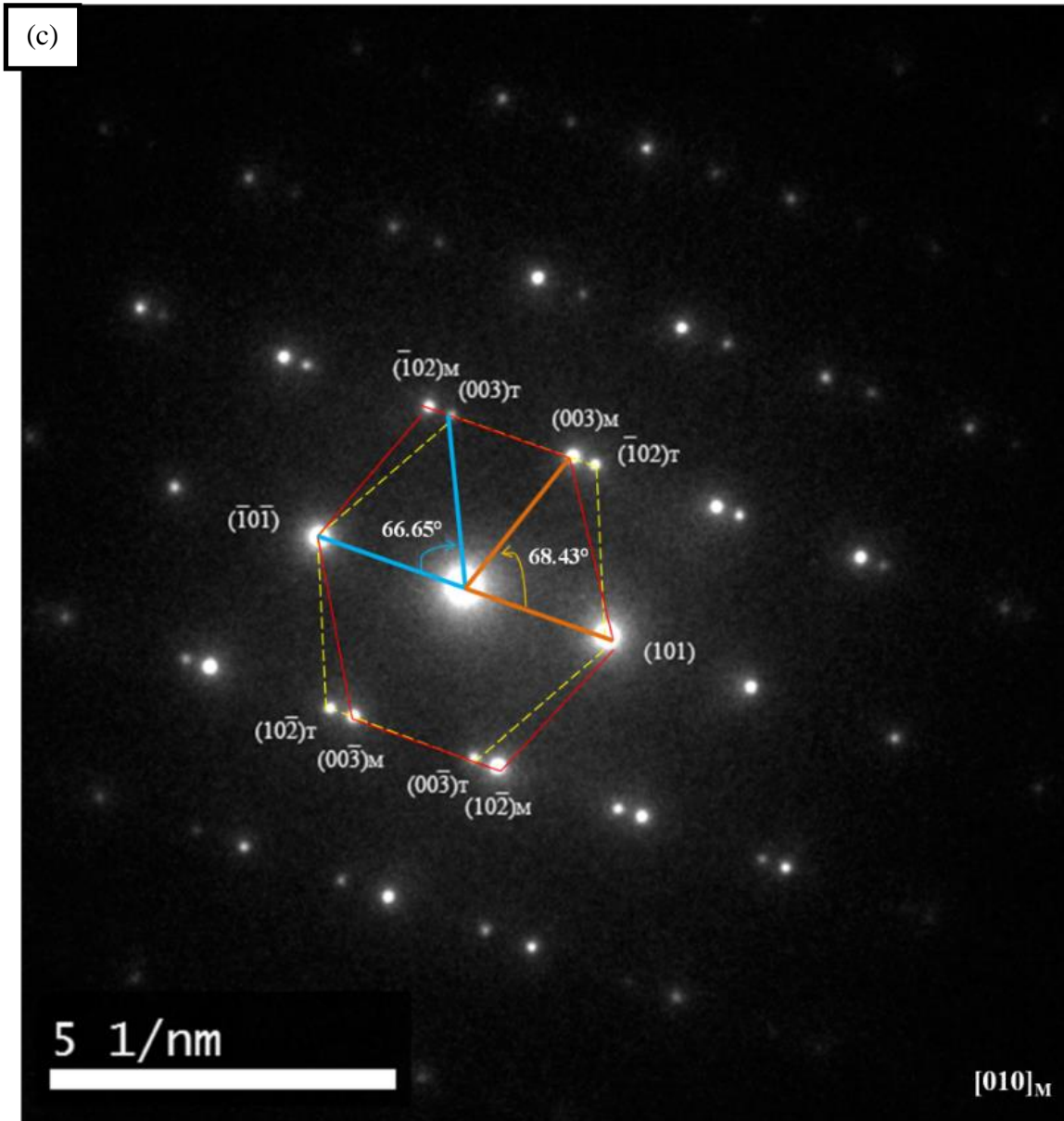


**Fig. 5.16(a) STEM image and (b) BF-TEM image of B<sub>4</sub>C-18 vol.%EuB<sub>6</sub> composite showing the presence of twinned structures in matrix grains.(c) SAED pattern obtained from twin boundary region of B<sub>4</sub>C phase (highlighted as dotted rectangular region in (b)).**

## **5.10 Implication of Twin boundaries on strengthening**

Twin boundaries possess comparatively lower energy interface than the grain boundaries and were believed to act as an effective obstacle to the crack displacement. It was reported that the twins in pore free hot-pressed B<sub>4</sub>C acting as an effective barrier for the development of cleavage cracks and contributes for material strengthening.<sup>[142]</sup> The absence or limited twin density observed in hot-pressed B<sub>4</sub>C could be mainly due to the annealing effect arising during longer holding period.

## **5.11 DISCUSSION ON ROLE OF OXIDES AS SINTER-ADDITIVE TO B<sub>4</sub>C**

In the previous section, the densification and phase evolution were comprehensively analysed using a host of microscopy techniques and critical examination of XRD results. A major emphasize was placed to discuss the role of Eu<sub>2</sub>O<sub>3</sub> on solid state sintering based densification mechanism as well as to analyse the origin of twinning in B<sub>4</sub>C. In this section, an attempt has been made to analyse the competition between the densification and microstructure development during spark plasma sintering of B<sub>4</sub>C with Eu<sub>2</sub>O<sub>3</sub> as a sinter-aid.

### **5.11.1 Anomaly in the densification trend of B<sub>4</sub>C: with Eu<sub>2</sub>O<sub>3</sub> additions**

Experimental observations suggest that unlike most transition metal oxides (TiO<sub>2</sub>, ZrO<sub>2</sub>, HfO<sub>2</sub> etc.) as sinter additive, the addition of Eu<sub>2</sub>O<sub>3</sub> (rare earth metal oxide) to B<sub>4</sub>C was noticed to decrease the sintering aptitude of B<sub>4</sub>C. As discussed in the introductory part, the use of oxides as sinter additive was found to be one of the attractive approaches to densify B<sub>4</sub>C ceramics. Significant efforts are invested to understand the positive/beneficial effects of oxides additions to B<sub>4</sub>C.<sup>[9-18, 36-37, 40-41]</sup> The chemical reaction between the oxides and B<sub>4</sub>C was often cited to be the reason for accelerated sintering, which provides additional driving force to the mass transfer

process. The chemical instability of oxide with respect to  $B_4C$  results in carbide / boride phase formation, which tend to create additional vacancies in lattice structures. The vacant lattice sites would cause lattice to shrink and result in strained lattice structures. Strained lattice structures and vacant atomic sites provide additional driving force for mass transfer process during sintering. The enhanced mass transport process would cause accelerated sintering and results in achieving higher sinter densities at lower sintering temperature compared to monolithic  $B_4C$ . [9-16, 17-18]

The present investigation of adding  $Eu_2O_3$  to  $B_4C$  was also aimed to achieve better sinterability. But the densification results suggest otherwise. In fact, the observation in the present study is in good agreement with the study by Wei et al. [43] study, but contradictory to report by Goldstein et al. [15] Though Goldstein et al. have not investigated the role of  $Eu_2O_3$  as sinter additive; his observations were based on other rare earth oxides ( $La_2O_3$  and  $Y_2O_3$ ). Critical remarks on such decreased sinterability were missing in that article. In the present study, the following argument is postulated as a reason for having such negative effect on densification of  $B_4C$ -rare earth oxide composite mixtures.

Unlike transition metal oxides ( $TrO_2$ ), rare earth oxide ( $Eu_2O_3$ ) reacts with  $B_4C$  in multiple stages as mentioned in reactions 2(a)-(c) (refer chapter 4), which is not the case with  $B_4C$ - $TrO_2$  mixtures. At high temperatures, reaction between  $B_4C$  and  $TrO_2$  is reported to occur in single step. Thus, the entire metal oxide in a single step will convert into its respective transition metal boride ( $TrB_2$ ) form. The heat treatment of  $B_4C$  in the presence of transition metal oxides is not reported to form borates. Thus, its conversion to borides is much simpler and quicker in comparison with rare earth oxide's conversion to borates and then to borides. In the first phase of reaction,  $Eu_2O_3$  reacts with  $B_4C$  to form  $Eu_3O_4$  and  $EuBO_3$ . In later stage, both  $EuBO_3$  and  $Eu_3O_4$  react with  $B_4C$  to form  $EuB_6$ .

The onset temperature for densification of monolithic B<sub>4</sub>C (SPS processed) is reported to be 1500°C. During initial stage of sintering, the Eu<sub>2</sub>O<sub>3</sub> addition resulted in the formation of europium borate (EuBO<sub>3</sub>) phase in addition to B<sub>4</sub>C and EuB<sub>6</sub> phases (Chapter 4: Figure 4.2). At the temperatures between 1500°C and 1900°C, monolithic B<sub>4</sub>C is reported to undergo stage II of densification (closure of porosities) (Refer Fig.5.1); whereas B<sub>4</sub>C containing Eu in EuBO<sub>3</sub> form would still be undergoing reduction process to form EuB<sub>6</sub> phase and CO (gas). In a B<sub>4</sub>C-Eu<sub>2</sub>O<sub>3</sub> composite mixture, the release of carbon monoxide (CO) gas would result in the creation of additional porosities in the densifying matrix. This could cause an additional burden to the densification process. It was reported that the relative density of ~90% could be achieved for monolithic B<sub>4</sub>C in the first 5 minutes of processing using SPS (Fig.5.3). Further, in order to achieve dense compacts of B<sub>4</sub>C, holding period was extended upto 15min duration. The closure of residual porosities, that are associated at the grain boundaries, necessitated longer holding period. In such a scenario, while B<sub>4</sub>C matrix undergoes densification, the presence of EuBO<sub>3</sub> could result in the formation of CO gas that creates additional porosities in the densifying matrix. FESEM micrographs (Figure 5.8) indicates the patches of pores in the microstructures of sintered B<sub>4</sub>C-EuB<sub>6</sub> composite and such pore related structures was not reported in case of transition metal oxide additions with B<sub>4</sub>C. This appears to be the plausible reason for achieving decreased sinterability for B<sub>4</sub>C-Eu<sub>2</sub>O<sub>3</sub> densification.

At temperature greater than 1500°C, the activation of both densifying (pore closure process) and non-densifying (CO gas release and its entrapment) processes could be one of the possible scenario for achieving lower sinter densities with B<sub>4</sub>C-Eu<sub>2</sub>O<sub>3</sub> composite compared to monolithic B<sub>4</sub>C. Since SPS route involves direct heating methodology and considering the conversion of EuBO<sub>3</sub> to EuB<sub>6</sub> as a rate limiting step, there is a clear trade-off between pore closure (densifying in SPS) and pore formation (two step conversion and CO release at latter stage of sintering). This aspect dictates the final densities of the sample. The processing under

slow heating rate coupled with extended dwell time operation could be a follow-up approach in achieving much closed to theoretical density in B<sub>4</sub>C-Eu<sub>2</sub>O<sub>3</sub> compacts system.

Transition metal oxide as sinter additive to B <sub>4</sub> C	Rare earth metal oxide as sinter additive to B <sub>4</sub> C
Some of the investigated transition metal oxides as additives: TiO <sub>2</sub> <sup>[10]</sup> , HfO <sub>2</sub> <sup>[17]</sup> , ZrO <sub>2</sub> <sup>[11]</sup> , VO <sub>2</sub> <sup>[14]</sup>	Investigated oxides: Eu <sub>2</sub> O <sub>3</sub> (present work), Sm <sub>2</sub> O <sub>3</sub> <sup>[43]</sup> , Y <sub>2</sub> O <sub>3</sub> <sup>[15]</sup>
Increases sintering aptitude of B <sub>4</sub> C	Decreases sintering aptitude of B <sub>4</sub> C (present work)
Increasing oxide content increases the sinter density	Increasing oxide content further deteriorates the sinter density
Final phases identified after sintering: TiB <sub>2</sub> , ZrB <sub>2</sub> , HfB <sub>2</sub> etc. in general MeB <sub>2</sub> (Metal diboride) form	Phases identified after sintering: EuB <sub>6</sub> in general MeB <sub>6</sub> (Metal hexaboride) form
Boride formation reaction mechanism: B <sub>4</sub> C+2MeO <sub>2</sub> +3C=2MeB <sub>2</sub> +4CO	Boride formation reaction mechanism: 3B <sub>4</sub> C+Me <sub>2</sub> O <sub>3</sub> =2MeB <sub>6</sub> +3CO
Boride formation occur as single step reaction (for eg. HfB <sub>2</sub> formation feasible @ <1000°C, when processed in vacuum)	EuB <sub>6</sub> formation occur in two different steps at temperatures (980°C and 1580°C)
No intermediate reaction products reported	Eu <sub>3</sub> O <sub>4</sub> , EuBO <sub>3</sub> forms at intermediate phases before conversion to EuB <sub>6</sub> phase
Driving force for enhanced sintering: <b>Reaction sintering</b>  Chemical reaction occurs between B <sub>4</sub> C and MeO <sub>2</sub> introduces structural vacancies in B <sub>4</sub> C lattice, alters B/C ratio and contributes for enhanced atomic mobility in comparison with monolithic B <sub>4</sub> C	In the case of rare earth oxides, boride formation causes chemical reactions to occur between B <sub>4</sub> C and Me <sub>2</sub> O <sub>3</sub> ; still results in decreased sintering aptitude. Reason: <b>Pore formation reaction</b> $\left(\frac{4}{23}\right)EuBO_3 + \left(\frac{5}{23}\right)B_4C + \left(\frac{7}{23}\right)C \rightarrow \left(\frac{4}{23}\right)EuB_6 + \left(\frac{12}{23}\right)CO \uparrow$ <ol style="list-style-type: none"><li>1. B<sub>4</sub>C undergo rapid densification involving pore closures at temperatures between 1500-1700°C (Region II)</li><li>2. At T: 1100-1600°C, EuBO<sub>3</sub> phase undergoes chemical reaction to form EuB<sub>6</sub> phase (refer pore former reaction)</li><li>3. This reaction involves the release of CO gas, which creates additional porosities during gas evolution</li></ol> <b>Competition between pore closure (by densification) and new pore formation (due to CO release) – Net effect: Reduced sinter density</b>

## 5.12 CONCLUSIONS (Sintering and Microstructure Development)

In the present thesis work, the specific role of spark plasma sintering parameters and Eu<sub>2</sub>O<sub>3</sub> sinter-aid additions on densification of B<sub>4</sub>C has been investigated with a particular emphasis on the understanding of sintering mechanism and microstructure development.

The following conclusions emerge,

- a) The adopted sintering scheme with final holding at 1900°C has successfully consolidated the B<sub>4</sub>C powder to near theoretical density. Near theoretical dense boron carbide compacts were obtained by Spark Plasma Sintering at comparatively lower temperature (1800°C) and holding time (15 min) than conventional sintering techniques.
- b) The sinterability of boron carbide increases with increase in temperature. Rapid rise in densification of boron carbide is observed at 1500°C. Marginal improvement in densification of boron carbide is observed with the influence of DC-pulsed current
- c) The sinterability of B<sub>4</sub>C was found to decrease with increased addition of Eu<sub>2</sub>O<sub>3</sub>.
- d) Based on critical XRD analysis of sintered compact and heat-treated powder mixture, two distinct reaction pathways are proposed to rationalize EuB<sub>6</sub> formation in sintered compacts.
- e) Microstructural observations revealed locally melted structures at the contact point between the particles, which is a direct evidence for the dominance of Joules heating effect in spark plasma sintering.
- f) Grain size of sintered boron carbide is measured to be in the range of 2-6µm which implies no grain coarsening in the spark plasma sintered compacts.
- g) Sintered B<sub>4</sub>C and B<sub>4</sub>C-18 vol% EuB<sub>6</sub> composite is found to exhibit predominant twinned grain structure. In twinned grains, intragranular EuB<sub>6</sub> phase and pores exhibited lath shape and oriented along the twin boundary.
- h) Interactive microstructure development, involving the competition among EuB<sub>6</sub> formation, pore formation (CO release) and twin morphology significantly dominates the densification process.
- i) Careful STEM and TEM analysis reveals the presence of asymmetric twins, threaded dislocations and stacking faults in dense boron carbide matrix.

---

## Chapter 6: Results and Discussions

### *Mechanical & Thermo-physical Properties*

---

#### 6. Mechanical Properties of Spark Plasma Sintered B<sub>4</sub>C

##### 6.1 Elastic Modulus and Hardness of monolithic B<sub>4</sub>C

The variation of elastic modulus of spark plasma sintered monolithic B<sub>4</sub>C samples as a function of relative density is shown in Fig. 6.1. These samples were obtained by spark plasma sintering at different temperatures as reported earlier in Section 5.1. The presence of porosity in the sample decreases the elastic modulus of the material. Porosity dependent elastic modulus of the samples sintered at 1800°C with different holding periods (5,10 and 15 min.) are shown in Fig. 6.2. The elastic modulus data have been listed in Table 6.1.

Elastic modulus of a porous material is reported to follow the following relationship <sup>[152]</sup>.

$$E = E_0 \frac{(1-p)^2}{1 + \left(\frac{1}{f} - 1\right)p} \dots\dots\dots(6.1)$$

where, E is the elastic modulus of the porous body

E<sub>0</sub> is elastic modulus of the full dense body,

p is volume fraction of porosity and

f is the shape factor of pores

Using the above relation shape factors have been calculated for the pores developed under different processing condition and the values are given in Table 6.2.

**Table 6.1 Density, Elastic modulus and Hardness of monolithic B<sub>4</sub>C sintered under different parameters**

Temperature (°C)	Holding time (minutes)	Pressure (MPa)	ON-OFF Pulse Sequence (milliseconds)	Relative Density (%)	Hardness, HV (GPa)	Elastic Modulus, E (GPa)
1100	15	50	5-5	65 ± 1	0.2	19 ± 15
1200				65.8 ± 1.5	0.2	39 ± 10
1300				66.5 ± 0.5	0.4 ± 0.7	45 ± 8
1400				70.5 ± 0.5	0.9 ± 0.3	74 ± 7
1500				71.8 ± 0.4	2.4 ± 0.6	105 ± 8
1600				81.8 ± 0.4	6.7 ± 1.5	138 ± 8
1700				94.4 ± 0.4	32 ± 2.9	418 ± 11
1800	5			91 ± 0.8	25.7 ± 1.5	403 ± 10
1800	10			96 ± 0.5	33.3 ± 1.5	447 ± 5
1800	15			> 99.9	37.2 ± 1.4	570 ± 20

**Table 6.2 Calculated shape factors of the pores developed under different processing condition of monolithic B<sub>4</sub>C**

Sintering Temperature (°C)	Holding time (minutes)	Pressure (MPa)	Porosity (%)	Shape factor
1600	15	50	18.2	0.32
1700	15		5.6	0.81
1800	5		9	0.84
1800	10		4	0.84
1800	15		0.2	-

Elastic modulus of spark plasma sintered near fully dense B<sub>4</sub>C was measured to be 570 ± 20 GPa which is greater than the elastic modulus values reported in literature <sup>[17]</sup>. The reason for

the difference in elastic modulus primarily lies in the differences in their relative densities. Calculated values of shape factor indicate rounding of pores in B<sub>4</sub>C as sintering temperature increases.

Hardness of monolithic B<sub>4</sub>C obtained by spark plasma sintering under different processing conditions are shown in Fig. 6.1 as a function of relative density. Fully dense B<sub>4</sub>C obtained at 1800 °C shows a maximum hardness of 37.2 GPa which is close to the value (36.4 GPa) reported by B.M. Moshtaghioun et al. for spark plasma sintered B<sub>4</sub>C [143]. Hardness measured for the B<sub>4</sub>C samples that are processed at 1800 °C for 5, 10 and 15 min were 25.7 GPa, 33.3 GPa, and 37.2 GPa respectively (Fig. 6.2).

An abrupt decrease in hardness from 32 GPa to 6.7 GPa was observed when sinter density decreases from 94.4% $\rho_{th}$  to 81.8% $\rho_{th}$ . Increase in porosity decreases the load bearing capability of the material and this is reflected in the measured value of hardness. Hardness of B<sub>4</sub>C measured in the present study (37.2GPa) is comparatively higher than the hardness of compacts that was obtained by hot-pressing (32.5 GPa) and pressureless sintering (25GPa) techniques, mainly due to its increased sample density. [13, 134] This also implies the impact of spark plasma sintering on material properties in comparison with conventional sintering techniques.

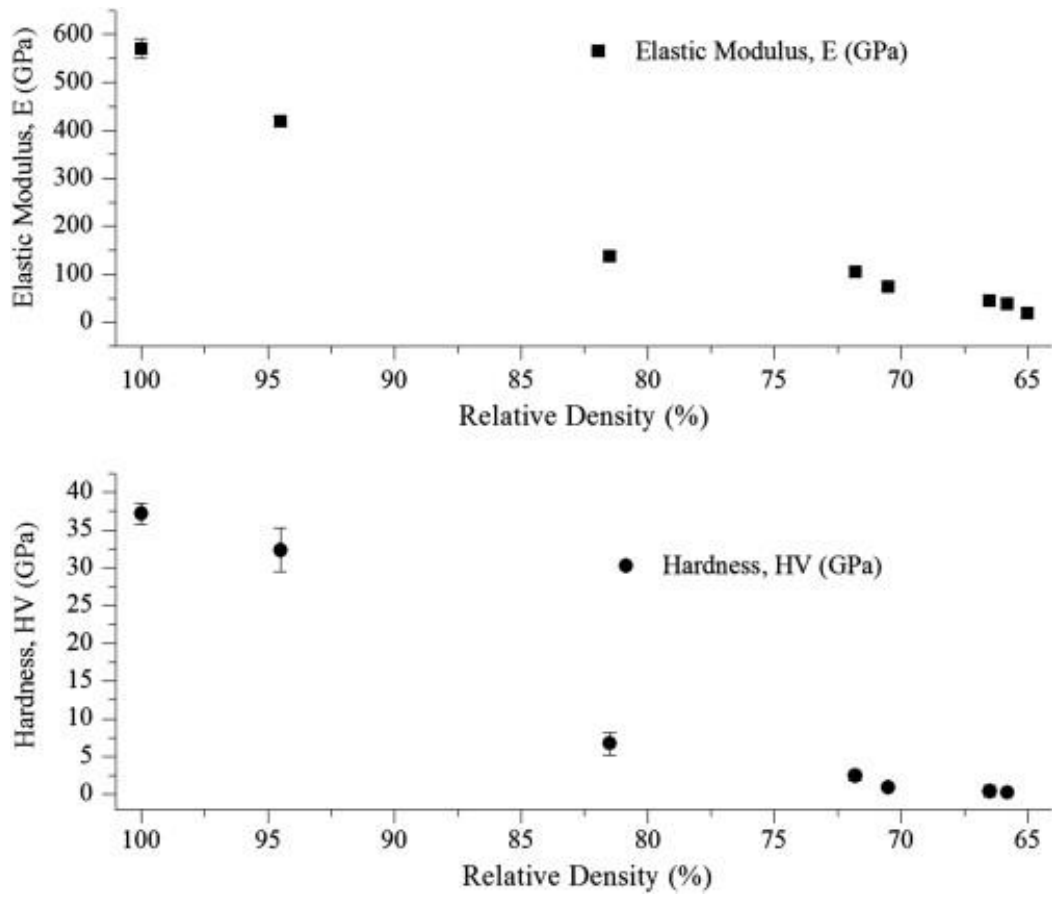


**Fig.6.1: Elastic Modulus and Hardness of Spark Plasma Sintered monolithic B<sub>4</sub>C samples plotted as a function of relative density**

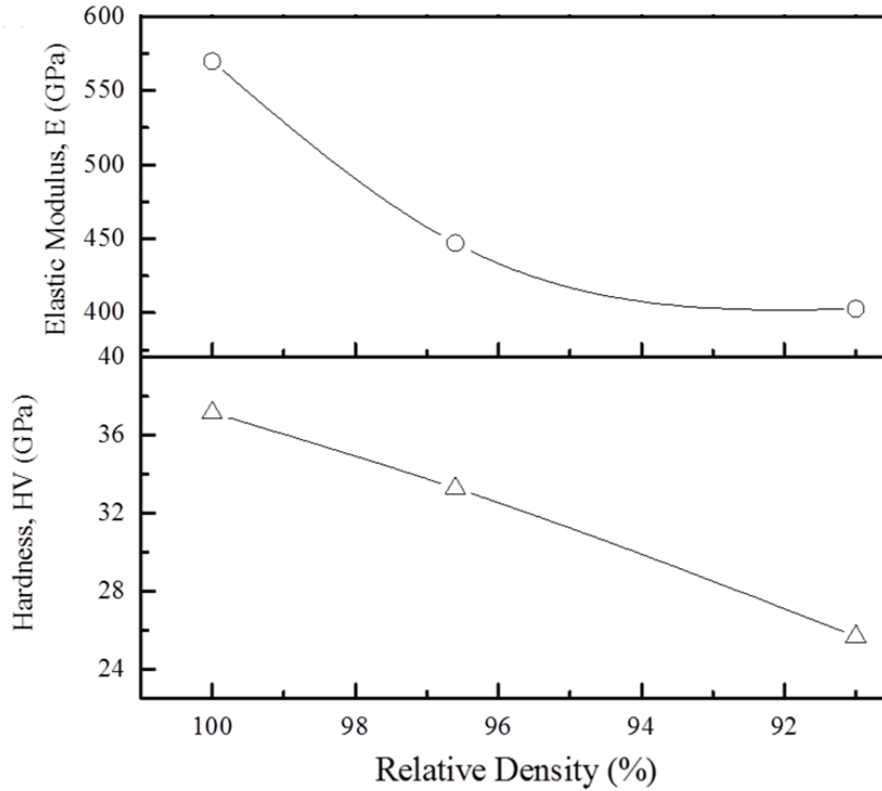


**Fig.6.2 Elastic Modulus and Hardness of B<sub>4</sub>C compact sintered at 1800°C with different holding periods (5,10 and 15 min.) is plotted with respect to its sample density obtained.**

## **6.2 Effect of EuB<sub>6</sub> (second phase) on Elastic Modulus and Hardness of B<sub>4</sub>C**

The elastic modulus of sintered monolithic B<sub>4</sub>C and B<sub>4</sub>C-EuB<sub>6</sub> composite was measured to be  $570 \pm 20$  and  $450 \pm 15$  GPa respectively (Table 6.3). Considering Voigt-Reuss model, the elastic modulus of a composite material should fall in between an upper and a lower bound values. Following relation was used for the estimation elastic modulus of a composite sample.

$$E_c = E_m \cdot V_m + E_s \cdot V_s \quad (6.2)$$

where,  $E_c$  is the predicted value of elastic modulus of dense composite respectively,  $E_m$  and  $V_m$  are elastic modulus and volume fraction of matrix phase,  $E_s$  and  $V_s$  are elastic modulus

and volume fraction of second phase.  $\text{EuB}_6$  is reported to exhibit elastic modulus of about 270 GPa <sup>[153]</sup>. The elastic modulus of dense composite is calculated to be 516 GPa. Considering the porosity effect, the elastic modulus of  $\text{B}_4\text{C-EuB}_6$  is estimated close to the measured value (450 GPa) when the shape factor is close to unity. The load vs. displacement curves for  $\text{B}_4\text{C-EuB}_6$  composite obtained from the instrumented indentation test is given in Fig. 6.3. The plots were found to be very consistent for all the 5 trials. Hardness of  $\text{B}_4\text{C}$  and  $\text{B}_4\text{C-EuB}_6$  composite was measured to be 37.2 GPa and 28.9 GPa. The hardness measured for  $\text{B}_4\text{C-EuB}_6$  composite is lower than the hardness of monolithic boron carbide which is attributed to the presence of relatively low hard  $\text{EuB}_6$  phase along with  $\text{B}_4\text{C}$  grains. Hardness value of  $\text{EuB}_6$  has been reported to be in the range of 18-21 GPa <sup>[64]</sup>.

**Table 6.3: Elastic Modulus and Hardness of sintered  $\text{B}_4\text{C}$  and  $\text{B}_4\text{C-EuB}_6$**

<b>Sample</b>	<b>% (%)</b>	<b>Elastic modulus (E) (GPa)</b>	<b>Hardness (Hv) (GPa)</b>
$\text{B}_4\text{C}$	99.8	$570 \pm 20$	$37.2 \pm 1.4$
$\text{B}_4\text{C-18vol.\% EuB}_6$	94.1	$450 \pm 15$	$28.9 \pm 1$

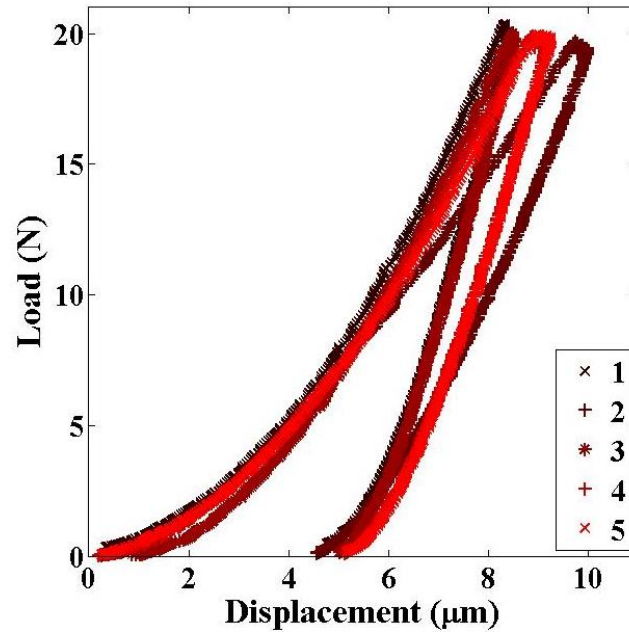


**Fig.6.3 Typical load vs. displacement plot recorded while performing hardness test instrumented on hot pressed B<sub>4</sub>C-10% Eu<sub>2</sub>O<sub>3</sub> samples.**

### **6.3 Fracture toughness of by indentation technique**

Attempt has been made to evaluate indentation fracture toughness of dense boron carbide, porous boron carbide and B<sub>4</sub>C-EuB<sub>6</sub> composite through indentation technique. Fracture toughness can be determined based on the radial cracks that are arising from the corners of the indented locations by considering it as a strength limiting flaws in ceramics. <sup>[144-145]</sup> A typical crack propagation patterns of fully dense B<sub>4</sub>C sample is shown in Fig. 6.4. The technique gives consistent result up to about 10% porosity. At porosity level beyond 10% crack formation from the corners of the indented locations gets impeded. This limits the fracture toughness measurement by indentation technique.

Anstis methodology <sup>[24]</sup> was adopted for indentation fracture toughness calculations.

$$K_{IC} = 0.016 \sqrt{\frac{E}{H}} \frac{P}{c^{\frac{3}{2}}} \quad (6.3)$$

where, E is the elastic modulus, H is the hardness, P is the indentation load and c is the average length of the cracks obtained in the tips of the Vickers marks. Measured elastic modulus and hardness values were incorporated in the indentation fracture toughness calculations.

Indentation fracture toughness of fully dense B<sub>4</sub>C sample was measured as 2.8 MPa.m<sup>1/2</sup> and it increases up to 4.3 MPa.m<sup>1/2</sup> corresponding to 94.4% ρ<sub>th</sub> density. The estimated values of indentation fracture toughness for different samples are given in Table 6.4.

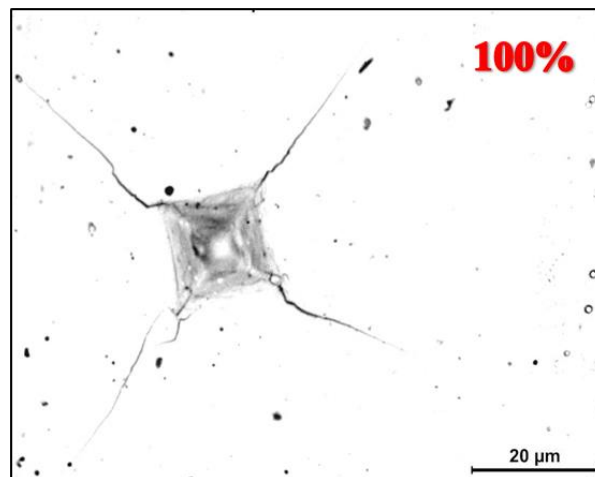


**Fig.6.4 Optical micrograph showing the crack propagation patterns of fully dense B<sub>4</sub>C samples after indentation fracture**

**Table 6.4: Indentation fracture toughness of B<sub>4</sub>C composites processed under different conditions**

<b>Processing condition</b>	<b>Density (%ρ<sub>th</sub>)</b>	<b>Indentation Fracture Toughness (MPa.m<sup>1/2</sup>)</b>
B <sub>4</sub> C,SPS, 1800 °C, 15 min	> 99.9	2.8 ± 0.2
B <sub>4</sub> C,SPS, 1800 °C, 10 min	96	3.1 ± 0.2
B <sub>4</sub> C,SPS, 1800 °C, 5 min	91	5.8 ± 0.4
B <sub>4</sub> C,SPS, 1700 °C, 15 min	94.4	4.3 ± 0.3
B <sub>4</sub> C-18vol.%EuB <sub>6</sub> SPS, 1900 °C, 15 min	94.1	6.6 ± 0.9

Marginal increase in indentation fracture toughness was observed with respect to increase in porosity up to 4%. Upon further increase of porosities results in significant improvement in toughness data. The indentation fracture toughness of SPS processed B<sub>4</sub>C (91% ρ<sub>th</sub>) sample is measured to be 5.8 MPa.m<sup>1/2</sup> which is higher than the values reported for monolithic B<sub>4</sub>C (in open literature) and are close to the values that are widely reported for B<sub>4</sub>C in the presence of second phase additives<sup>[17, 145-146]</sup>. B.M. Moshtaghioun et al. have reported indentation fracture toughness of 4.8 MPa.m<sup>1/2</sup> corresponding to 90.3 %ρ<sub>th</sub> B<sub>4</sub>C sample.<sup>[143]</sup> This increase in fracture toughness can be explained based on the differences that were observed in crack propagation pattern between fully dense and porous compacts (not shown here). B<sub>4</sub>C added with 18vol.% EuB<sub>6</sub> resulted in two times increase in indentation fracture toughness values (6.6 MPa.m<sup>1/2</sup>). The fracture toughness of dense B<sub>4</sub>C compact, the crack propagation is observed to be a straight-line path, whereas, in the case of porous and composite compacts,

crack propagates in a zig-zag fashion as it encounters crack tip deflections at the pore/second phase boundaries and in-turn contributes for increased fracture toughness of the material. Thus, increasing pore/second phase content to a certain extent acts as crack deflectors/arrestors in the material, and contributes for enhancing the indentation fracture toughness of the boron carbide.

#### **6.4 Flexural Strength and Estimation of Weibull Distribution Parameters**

For a given ceramic material, the crack size, shape factor and its orientation differ from sample to sample. It is experimentally noticed and reported that the strength of ceramics differs even while testing samples prepared under identical conditions and are tested under identical loading conditions. The mean strength, as determined from a multiplicity of similar tests depends on volume of material stressed, shape of test specimen and on nature of loading. Thus, it is well recognized that strength of the ceramics needs to be analysed using different probabilistic approaches. Because, the probability of failure or fracture of a given ceramic sample critically depends on the presence of a potentially dangerous crack of size greater than a characteristic critical crack size. Thus, the probability of finding critical crack size is higher in larger volume test specimens and consequently the brittle materials do not have any deterministic strength property. Since brittle materials exhibit volume dependent strength behavior, the mean strength decreases as the specimen volume increases. From the initial experimental observations, it was evident that a definite relationship should exist between the probability that a specimen will fracture and the stress to which it is subjected.<sup>[147]</sup> Weibull distribution function has been used to characterize the strength of monolithic B<sub>4</sub>C and B<sub>4</sub>C-18 vol% EuB<sub>6</sub> composite.

Flexural strength of monolithic B<sub>4</sub>C was measured to be varying in the range of 159 to 203 MPa. Upon reinforcement of EuB<sub>6</sub>, the flexural strength of B<sub>4</sub>C composite samples was increased up to a range of 223 to 302 MPa. The flexural strength ( $\sigma$ ) values were ranked from the minimum to the maximum value and for each strength value a probability of failure  $P(\sigma)$  is assigned based on its ranking  $i$ , with  $i$  ranging from 1 to N, where N is the number of measurements of flexural strength for samples of a particular material. The cumulative probability of failure  $P(\sigma)$  is calculated using the following equation.

$$P(\sigma) = \frac{i - 1/2}{N} \quad (6.4)$$

Following Weibull distribution function, the generalized strength distributions law can adopt the following expression.

$$P(\sigma) = 1 - \exp\left[-\frac{V}{V_o} \left(\frac{\sigma}{\sigma_o}\right)^m\right] \quad (6.5)$$

where, V is the volume of the material tested, V<sub>o</sub> is the reference volume,  $\sigma_o$  is the characteristic flexural strength of the material at which probability of failure is 0.63.

The above equation can be re-written as:

$$\ln[-\ln(1 - P(\sigma))] = \ln \frac{V}{V_o} + m \ln\left(\frac{\sigma}{\sigma_o}\right) \quad (6.6)$$

Characteristics flexural strength and Weibull modulus (m) have been obtained from the linear fitted plot of  $\ln[-\ln(1 - P(\sigma))]$  versus  $\ln(\sigma)$  as shown in Fig. 6.5. The flexural strength values of monolithic B<sub>4</sub>C and B<sub>4</sub>C-EuB<sub>6</sub> composite are estimated to be 185 and 270 MPa respectively. Weibull modulus was estimated to be 16.0 and 12.3 for monolithic B<sub>4</sub>C and B<sub>4</sub>C-18vol.%EuB<sub>6</sub> composite samples, respectively (Table 6.5). The derived Weibull modulus



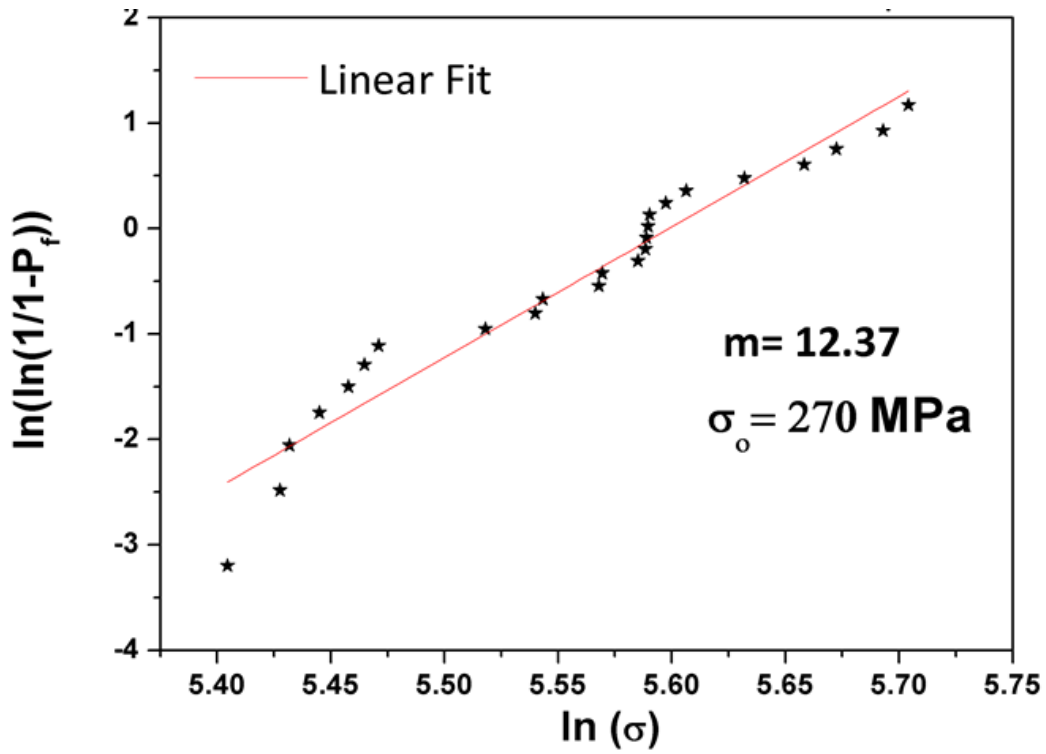


**Fig.6.5: Strength reliability analysis for monolithic B<sub>4</sub>C (0% Eu<sub>2</sub>O<sub>3</sub>) and B<sub>4</sub>C (10% Eu<sub>2</sub>O<sub>3</sub>) based on three point flexural strength and weakest link fracture statistics ( $\sigma$  in MPa)**

**Table 6.5: Flexural strength of hot pressed B<sub>4</sub>C composites measured using 3 point bending test**

Eu <sub>2</sub> O <sub>3</sub> addition to B <sub>4</sub> C (vol. %)	Flexural Strength (MPa)	Weibull modulus (m)	Flexural Stiffness (N/mm)
0	185 ± 15	16	3400
10	270 ± 20	12.33	3900

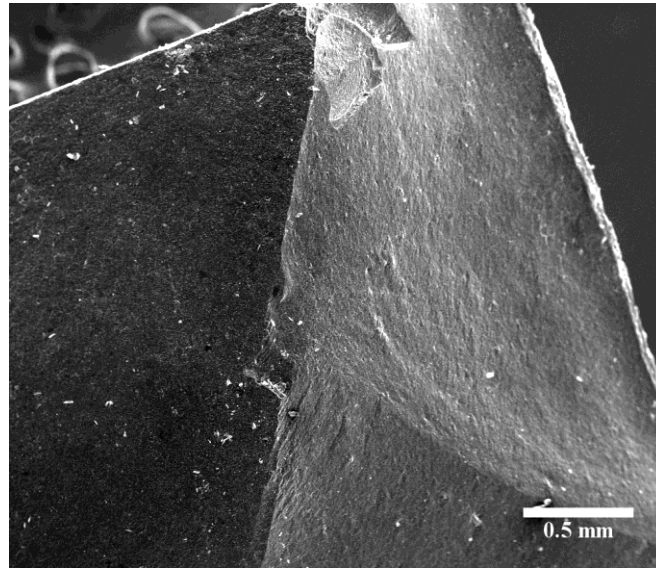
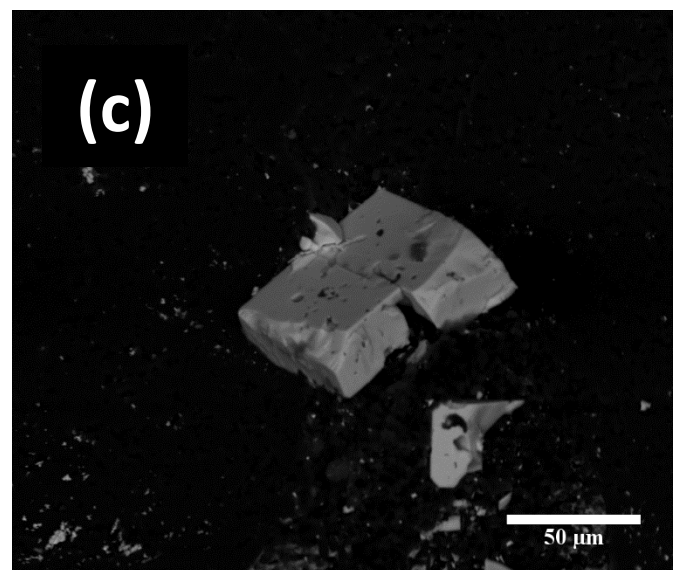
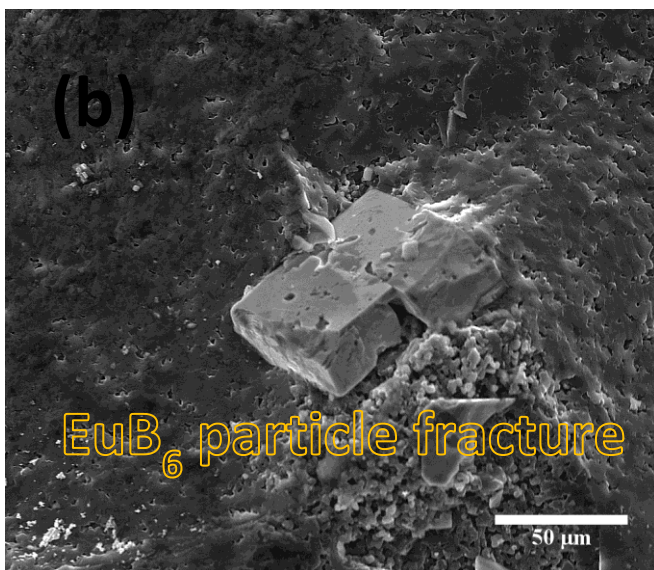
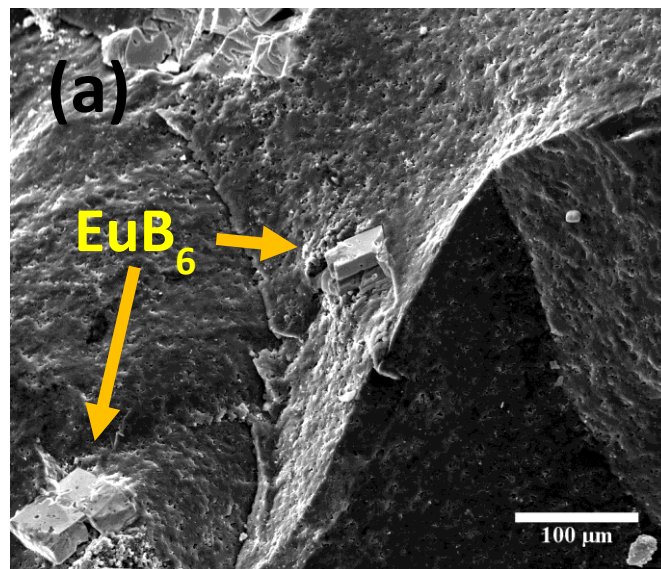


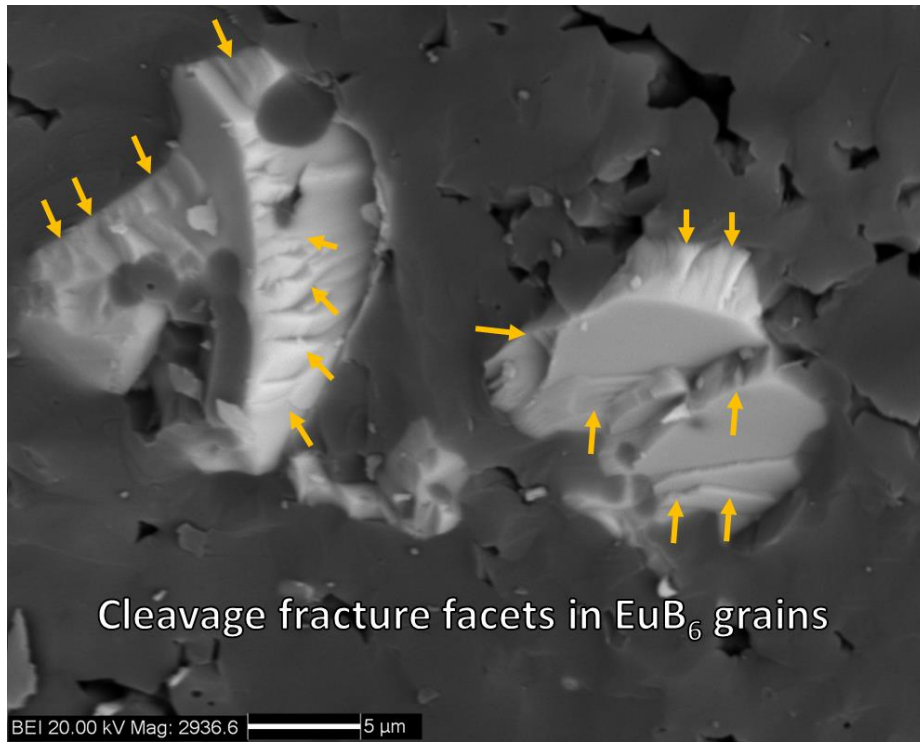
**Fig.6.6 Macroscopic fracture surface of monolithic B<sub>4</sub>C showing fracture planes at 45° angles.**

The fracture surface of bend tested samples were characterized to identify the underlying reason behind the improved failure strength / properties. Representative images of the fracture surface are given in Figures 6.6 and 6.7. The macroscopic examination of fracture surface of monolithic B<sub>4</sub>C shows flat cleavage planes indicating the brittle nature of the fracture. In the composite, the EuB<sub>6</sub> second phase particles were clearly visible along the fracture planes. BSE detector was used to confirm that these particles were indeed europium rich and a representative image is given in Fig. 6.7c. The important point to note here is that in the composites, the fracture planes cut through the second phase particles and hence contributes for enhancing the flexural strength. On a closer observation of fracture surface regions, cleavage faceted regions (Fig. 6.7(d-e)) were identified at the EuB<sub>6</sub> particles. This faceting signature implies EuB<sub>6</sub> is not undergoing simple cleavage fracture rather jagged non-

linear cracking. This sort of non-linear cracking process leads to a reduction of the crack extension force.



(d)



(e)

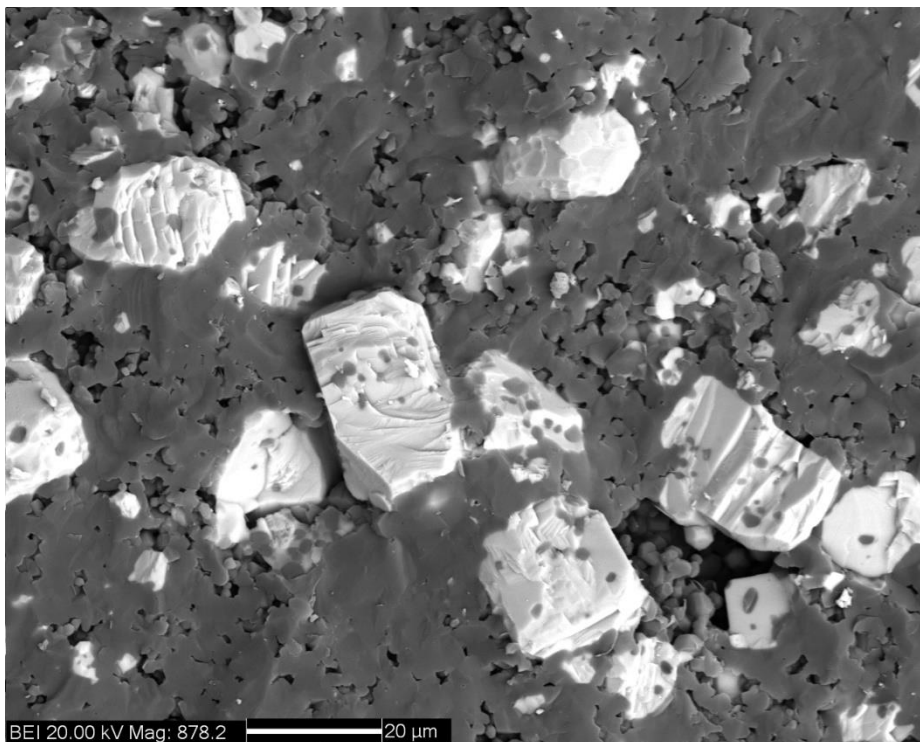
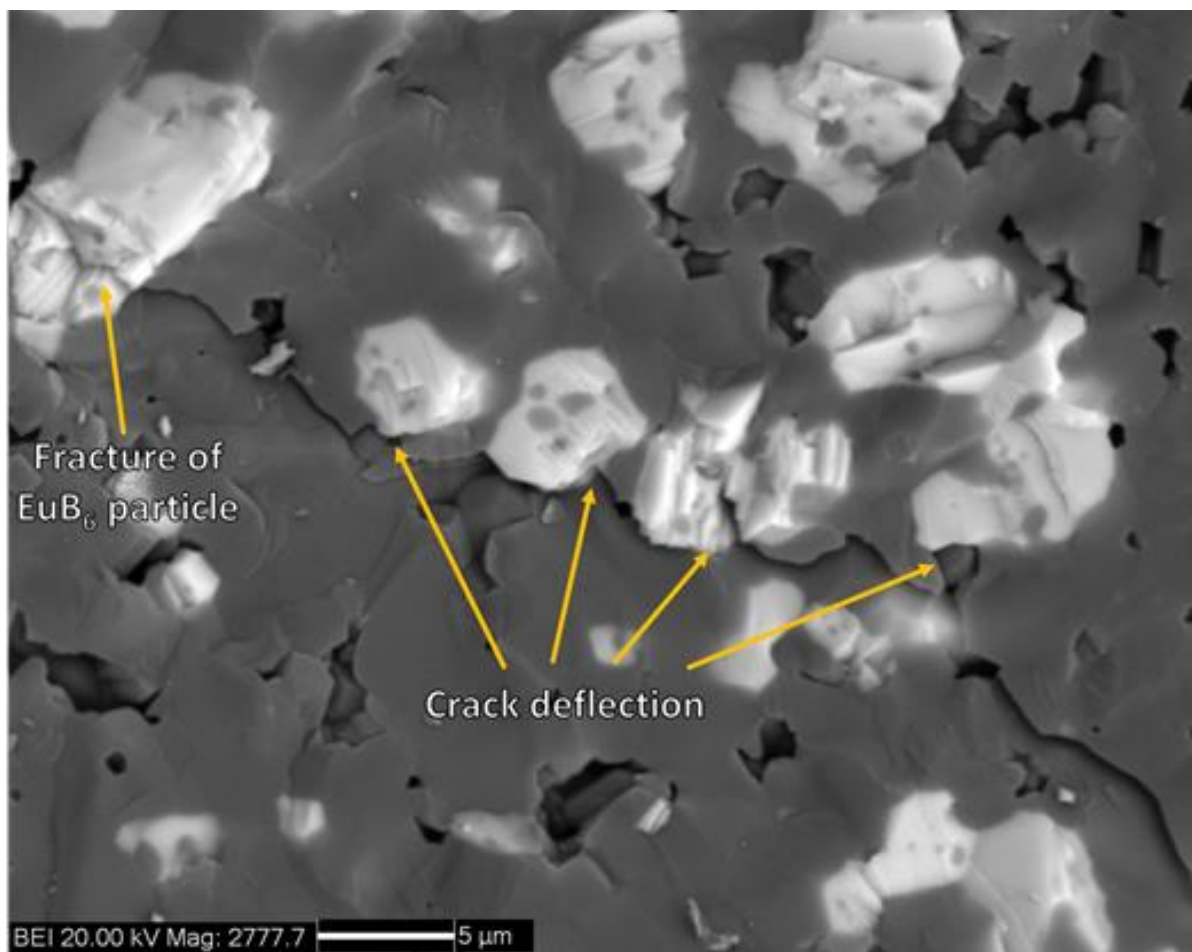


**Fig.6.7(a-e) SEM images showing fracture surfaces of  $\text{B}_4\text{C}$ -10 vol.%  $\text{Eu}_2\text{O}_3$  composite**

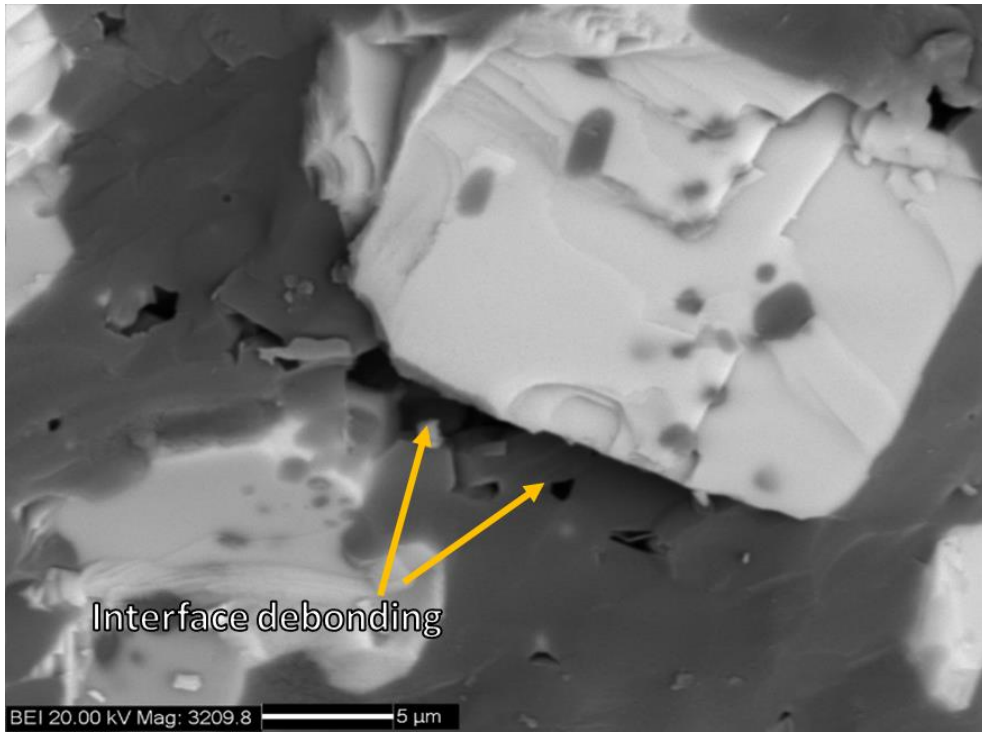
Microstructural analysis (Fig. 6.8(a)-(d)) indicates major toughening phenomenon as crack deflections, interface debonding and crack branching. The difference in lattice parameter between the matrix ( $B_4C$ ) and second phase ( $EuB_6$ ) results in formation of incoherent interface due to the difference in their cell volume and the region of this nature deflects the crack and contributes for fracture toughness improvement. The thermal expansion mismatches between the matrix  $B_4C$  ( $\alpha_m = 4.5 \times 10^{-6} K^{-1}$ )<sup>[148]</sup> and second phase,  $EuB_6$  ( $\alpha_p = 7.4 \times 10^{-6} K^{-1}$ )<sup>[148]</sup> results in the generation of residual stresses at and around the  $EuB_6$  particles. As the second phase exhibit higher coefficient of thermal expansion in comparison with matrix,  $B_4C$  and  $EuB_6$  phases are likely to present in compressive and tensile stress states, respectively. The existence of this compressive stresses in the  $B_4C$  matrix decreases the stress intensity factor by  $\Delta K_I$ . Ultimately, the decrease in stress concentration factor by  $\Delta K_I$  is equivalent to increase in crack growth resistance by the same amount  $\Delta K_I$ .

The crack tip deflects when it encounters the region of residual strain or weak interfaces in the composite.<sup>[144]</sup> This residual strain would occur due to the difference in elastic modulus and/or thermal expansion mismatches between matrix and the second phase. Fig. 6.8(a) show the crack path experiencing multiple deflections at the second phase interface and thereby it takes longer propagation path for failure. If a crack is deflected out of the plane that is normal to an applied uniaxial tensile stress, the crack is no longer loaded in a simple Mode I and is therefore not subjected to the maximum tensile stress and thus, contributes most to the fracture toughness. Fig. 6.8(c) and (d) show the secondary electron (SEI) and back scattered electron (BSE) images of the composites, which clearly show the crack branching and deflections at the  $EuB_6$  particle. Interface debonding was observed at the second phase particles (Fig. 6.8b) and this phenomenon consumes part of the fracturing energy and lowers

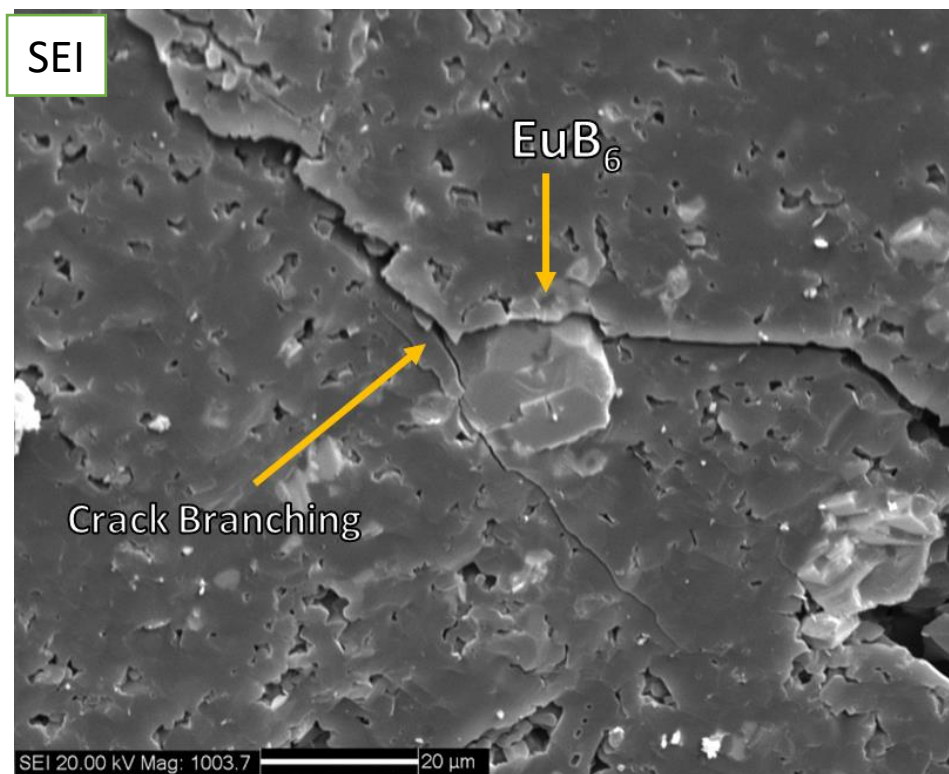
the driving force for further failure and thus, contributes towards enhancing failure resist properties. Thus, the synergistic effects of cleavage faceting, interface debonding, crack branching and deflections together contributes towards realization of 40% higher flexural strength in the developed  $B_4C$ - $EuB_6$  composite.



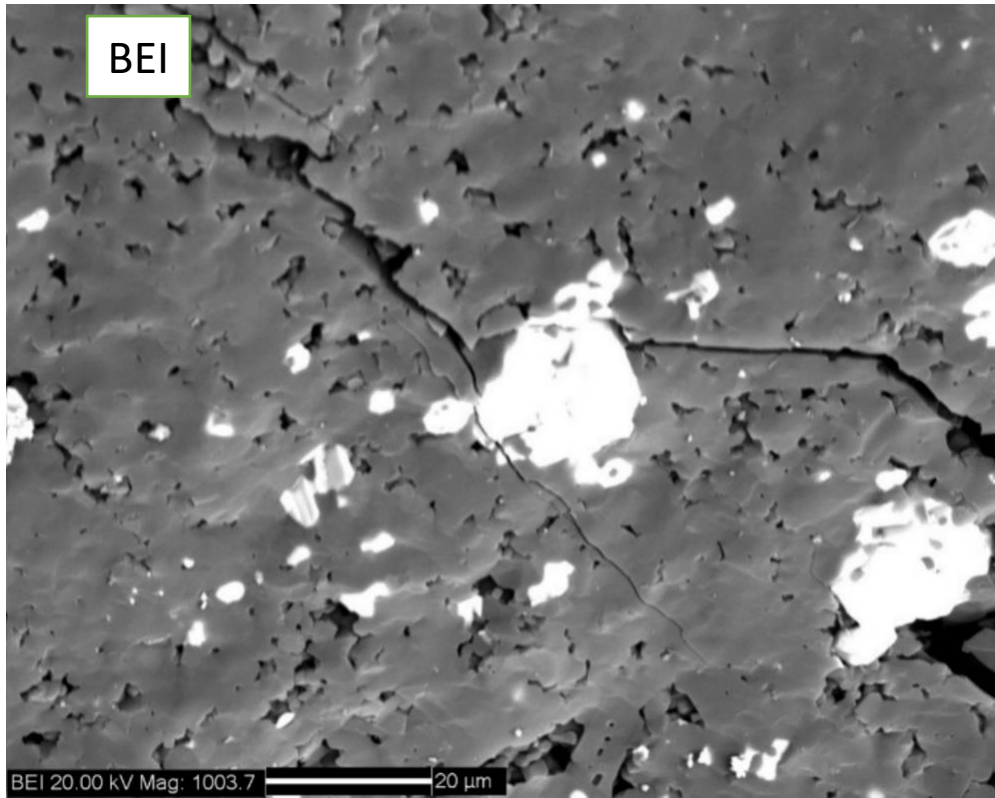
**(a)**



(b)



(c)



**(d)**

**Fig. 6.8(a-d) SEM micrographs showing the crack propagation path experiencing crack deflections, crack branching and interface debonding**

## 6.5 Thermal transport property

Thermal conductivity plays a crucial role in the design of engineering systems, where thermal stress is of significant concern. A variety of measurement techniques are available for thermal characterization of bulk material, such as the steady-state method, transient hot-wire method, laser flash diffusivity method and transient plane source method, to name a few. While steady-state methods measure thermal properties by establishing a temperature difference that does not change with time, transient techniques usually measure time-dependent energy dissipation process of a sample. Each of these techniques has its own advantages and limitations and is suitable for only a limited range of materials, depending on the thermal properties, sample configuration and temperature measurement. In the present work, thermal diffusivity was measured and using specific heat capacity from standard database, thermal conductivity ( $k$ ) was derived for both  $B_4C$  and  $B_4C$ -EuB6 composite using laser flash technique (Thermal Properties AnalyzerFlashline 5000) according to ASTM 1461-13.

In the present work, the thermal conductivity ( $k$ ) has not been measured directly, but calculated as a function of temperature from the measured thermal diffusivity ( $\alpha$ ) and heat capacity ( $C_p$ ), with known ceramic density ( $\rho$ ) using the equation, given below

$$k(T)=\alpha(T).\rho(T).C_p(T)$$

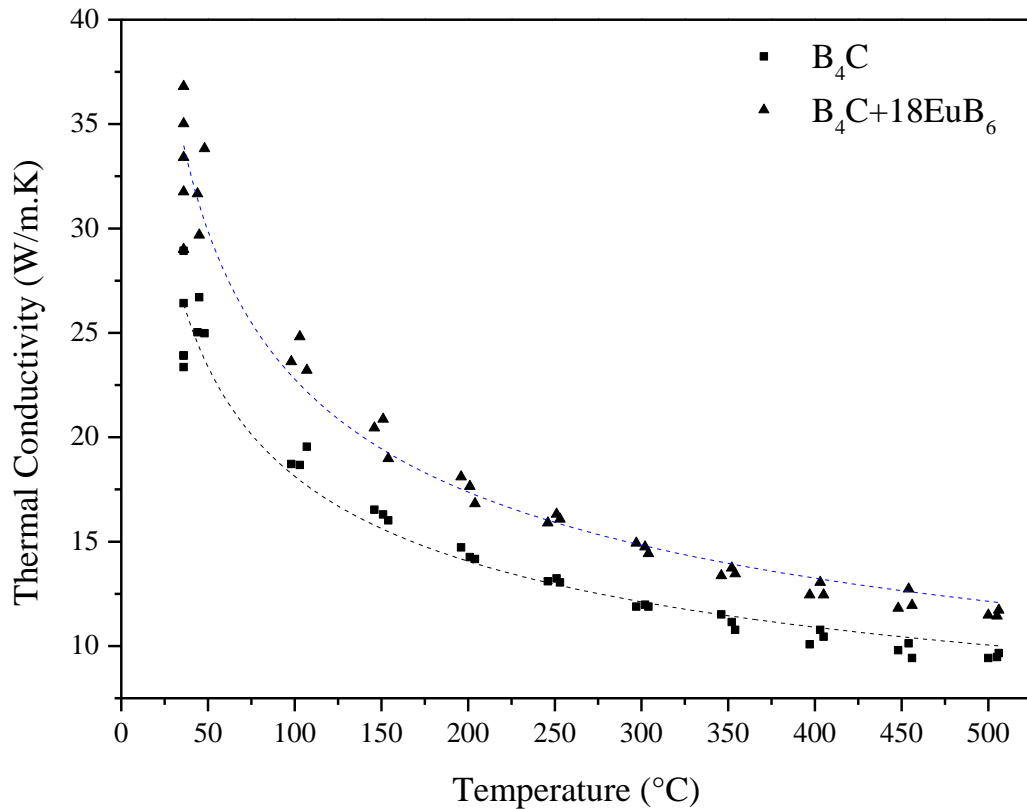


**Fig.6.9 Thermal conductivity of monolithic B<sub>4</sub>C and B<sub>4</sub>C-18 vol.% EuB<sub>6</sub>.**

Fig. 6.9 depicts the estimated thermal conductivity ( $k$ ) of monolithic B<sub>4</sub>C and B<sub>4</sub>C-EuB<sub>6</sub> composite for temperatures ranges between 50 to 500°C. The thermal conductivity of monolithic B<sub>4</sub>C is measured to be 23 W/m.K at room temperature and shows a decreasing trend with increasing temperature. The developed B<sub>4</sub>C-EuB<sub>6</sub> composite also exhibited similar trend in conductivity upon increase of temperature. The developed B<sub>4</sub>C composite exhibited almost 50% higher thermal conductivity in comparison with monolithic B<sub>4</sub>C. Thermal conductivity measured for B<sub>4</sub>C is in good agreement with that of literature reported values (13-22 W/m.K)<sup>[149]</sup>. It is well documented in literature that the thermal conductivity of a composite depends on the thermal conductivity of its components and the interfacial thermal resistance between the components. In case of B<sub>4</sub>C-EuB<sub>6</sub> composite, the addition of the

second phase leads to decreased resistance for the heat flow through the components and their interfaces, thereby contributes for enhanced thermal conduction.

## 6.6 Electrical Transport Property

The parabolic nature of current-voltage characteristics was exhibited by both monolithic B<sub>4</sub>C and B<sub>4</sub>C-EuB<sub>6</sub> composite samples in the investigated temperature range upto 300 °C. This non-linear behavior (V-I) strongly infers the voltage dependency in the current conducting characteristics of the material. The room temperature electrical conductivity of monolithic B<sub>4</sub>C is measured to be 10<sup>-5</sup> (S/cm) (Fig. 6.10). Upon addition of 9 and 18 vol% EuB<sub>6</sub>, the room temperature conductivities of B<sub>4</sub>C was increased to 10<sup>-5</sup> (S/cm) and 10<sup>-4</sup> (S/cm) respectively. EuB<sub>6</sub> is reported to have conductivity of the order of 10<sup>3</sup> (S/cm) which is 7 order higher than monolithic B<sub>4</sub>C values. The very low values of conductivity in the B<sub>4</sub>C - 9 vol% EuB<sub>6</sub> composite indicate EuB<sub>6</sub> phases are below the threshold level to facilitate percolation. Voltage dependence conductivity also confirms that conducting second phase EuB<sub>6</sub> particles are not interconnected.

Variation of electrical conductivity with respect to temperature in the form of Arrhenius plot is shown in Fig. 6.11(a)-(b) for both monolithic B<sub>4</sub>C and B<sub>4</sub>C-18vol% EuB<sub>6</sub> composite. The activation energy estimated for monolithic B<sub>4</sub>C is 0.18 for a temperature range of 50-150 °C, inferring bi-polaron hopping as the chief governing conduction mechanism in B<sub>4</sub>C. At temperatures above 150 °C, the sudden change in the slope of electrical conductivity could be noticed which indicates the activation of higher energy states that facilitating the electrical conduction. The conductivity of B<sub>4</sub>C-9vol.%EuB<sub>6</sub> was close to monolithic B<sub>4</sub>C and also exhibited similar current conduction characteristics as that of monolithic B<sub>4</sub>C suggesting bi-

polaron hopping as the active conduction mechanism.  $B_4C$  with 18 vol.%  $EuB_6$  sample exhibited linear conducting behaviour up to 300 °C, which is completely different from  $B_4C$  and  $B_4C-9EuB_6$  samples. This linear behaviour suggests metal like conductivity, which is not governed through semiconducting  $B_4C$  grains. Reinforcement of 18% $EuB_6$  in  $B_4C$  matrix satisfies and establishes the critical threshold network for percolation - tunnelling and conducts the current along  $EuB_6$  particles (acting as a least resistance path), which is evident from the measured conductivity values of composite sample.

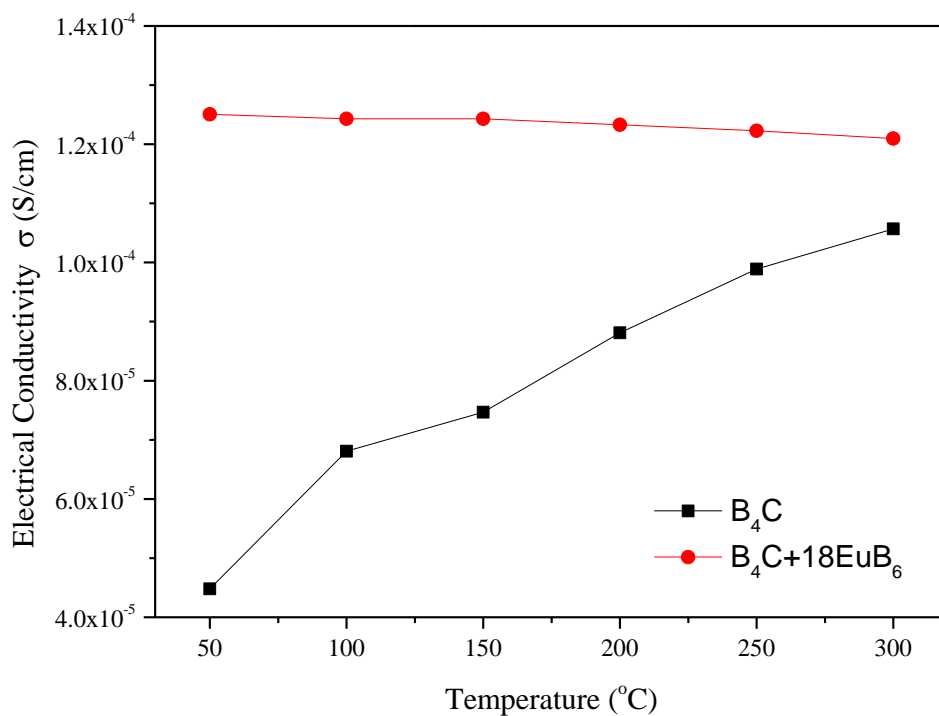


**Fig. 6.10** Variation of electrical conductivity with respect to temperature (a) monolithic  $B_4C$  and (b)  $B_4C-EuB_6$  composite

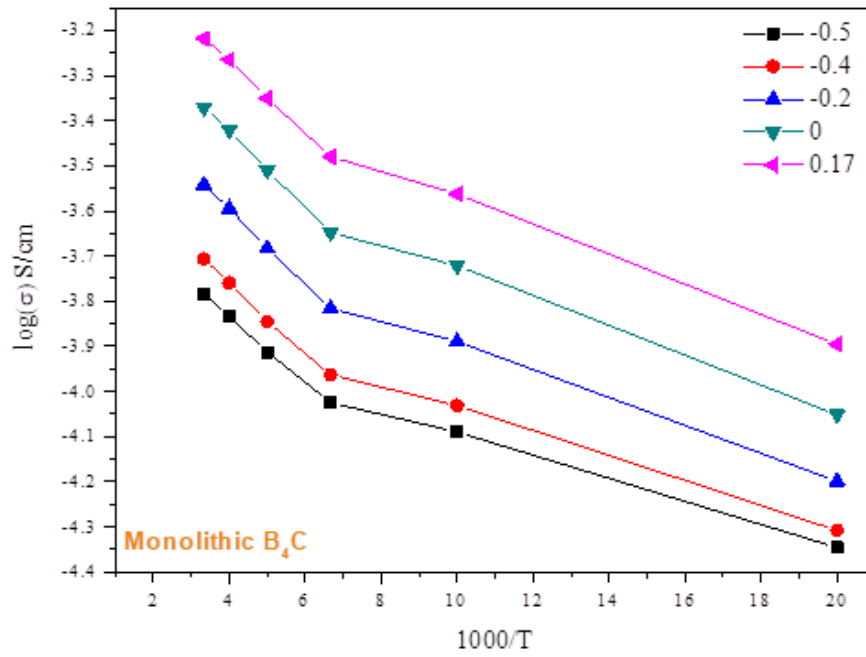


Fig. 6.11(a) Arrhenius plot of electrical conductivity for monolithic  $B_4C$

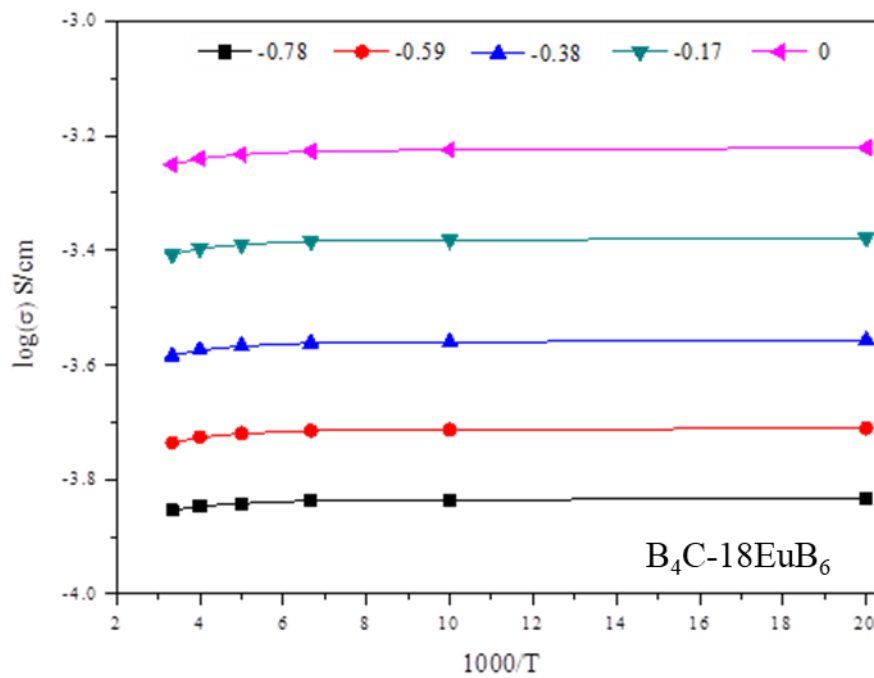


Fig. 6.11(b) Arrhenius plot of electrical conductivity for  $B_4C$ - $EuB_6$  composite

Material composition	Theoretically calculated thermal neutron absorption cross-section (barn)
B <sub>4</sub> C	614
B <sub>4</sub> C+9 vol.%EuB <sub>6</sub>	727
B <sub>4</sub> C+18 vol.%EuB <sub>6</sub>	819

**TABLE 6.6:** Thermal neutron absorption cross-section of B<sub>4</sub>C-EuB<sub>6</sub> composites

At the closure, the relevance of the development of B<sub>4</sub>C-EuB<sub>6</sub> towards nuclear-specific applications should be highlighted. In this context, their respective thermal neutron absorption cross sections <sup>[151]</sup> was calculated and the theoretically predicted values are summarised in Table 6.3. Based on the calculated values, it is to be noted that the B<sub>4</sub>C reinforced with ~18vol.% EuB<sub>6</sub> tend to exhibit 33% higher absorption cross-section in comparison to monolithic B<sub>4</sub>C. Though the value seem promising and makes it as a potential candidate for reactor applications, the actual performance of the material can only be established with In-Pile experiments.

## 6.7 CONCLUSIONS (Mechanical and Thermo-Physical Properties)

- (a). Hardness increases from 0.2 GPa to 37.2 GPa as a function of increasing density of boron carbide from 65% $\rho_{th}$  to near theoretical density.
- (b). Elastic modulus increases as a function of increase in density and reaches a maximum of 570 GPa corresponding to full dense boron carbide.
- (c) The developed B<sub>4</sub>C-EuB<sub>6</sub> composite exhibited 40% superior flexural strength in comparison with monolithic boron carbide.
- (d) B<sub>4</sub>C-EuB<sub>6</sub> composite exhibited almost twice the thermal and electrical conductivities compared with monolithic boron carbide ceramic.
- (e) B<sub>4</sub>C added with Eu<sub>2</sub>O<sub>3</sub> exhibits superior mechanical, thermal and electrical properties without deteriorating the neutron absorption cross-section of the material. In fact, the developed material exhibited higher neutron absorption cross-section compared with monolithic B<sub>4</sub>C.

---

## Chapter 7: Conclusions

---

In the present thesis work, the specific role of spark plasma sintering parameters and  $\text{Eu}_2\text{O}_3$  additions on densification of  $\text{B}_4\text{C}$  has been investigated with a particular emphasis on the understanding of sintering mechanism and microstructure development. The sintered materials have been characterised for mechanical, thermal and electrical properties.

The following conclusions emerge from the present investigation.

- a) The adopted sintering scheme with final holding at 1900 °C has successfully consolidated the  $\text{B}_4\text{C}$  powder to near theoretical density. Near theoretical dense boron carbide compacts has been obtained by Spark Plasma Sintering at comparatively lower temperature (1800°C) and holding time (15 min) than conventional sintering techniques.
- b) Rapid rise in densification of boron carbide is observed at 1500°C. Marginal improvement in densification of boron carbide is observed with the influence of DC-pulsed current.
- c) Microstructural observations revealed locally melted structures at the contact point between the particles, which is a direct evidence for the dominance of Joules heating effect in spark plasma sintering.
- d) Based on critical XRD analysis of sintered compact and heat-treated powder mixture of  $\text{B}_4\text{C}$  and  $\text{Eu}_2\text{O}_3$ , two distinct reaction pathways are proposed to rationalize  $\text{EuB}_6$  formation in sintered compacts. The reaction pathways include formation of intermediate phase  $\text{EuBO}_3$  and formation of CO gas at later stage.

- e) The sinterability of  $B_4C$  was found to decrease with increased addition of  $Eu_2O_3$ . The reason for decreased sintering aptitude of  $B_4C$  in the presence of rare earth oxide addition has been attributed to competition between densification and microstructure development.
- f) Grain size of sintered boron carbide is measured to be in the range of 2-6  $\mu m$  which implies no grain coarsening in the spark plasma sintered compacts.
- g) Sintered  $B_4C$  and  $B_4C$ -18 vol%  $EuB_6$  composite is found to exhibit predominant twinned grain structure. In twinned grains, intragranular  $EuB_6$  phase and pores exhibited lath shape and oriented along the twin boundary.
- h) Interactive microstructure development, involving the competition among  $EuB_6$  formation, pore formation (CO release) and twin morphology significantly dominates the densification process.
- i) Careful STEM and TEM analysis reveals the presence of asymmetric twins, threaded dislocations and stacking faults in dense boron carbide matrix.
- j) Elastic modulus increases as a function of increase in density and reaches a maximum of 570 GPa corresponding to full dense boron carbide. Full dense monolithic  $B_4C$  shows a maximum hardness of 37.2 GPa.
- k) Both elastic modulus and hardness decreases in the  $B_4C$ - $EuB_6$  composite compared to monolithic  $B_4C$ .
- l) The developed  $B_4C$ - $EuB_6$  composite exhibited 40% superior flexural strength in comparison with monolithic boron carbide.
- m)  $B_4C$ - $EuB_6$  composite exhibited superior thermal conductivities compared to monolithic boron carbide in the experimental temperature range from ambient to 500  $^{\circ}C$ .
- n) The electrical conductivity of both monolithic  $B_4C$  and  $B_4C$ - $EuB_6$  composite is found

to be voltage dependent. The composite with 18 vol%  $\text{EuB}_6$  shows metal like electrical conductivity as function of temperature whereas the monolithic  $\text{B}_4\text{C}$  shows semi-conductive behavior.

- o)  $\text{B}_4\text{C}$  added with  $\text{Eu}_2\text{O}_3$  exhibits superior mechanical and thermal properties without deteriorating the neutron absorption cross-section of the material. The developed material has potential application as a neutron absorber material.

---

## Chapter 8: Future Scope

---

1. Comparison of in-situ  $\text{EuB}_6$  and externally added  $\text{EuB}_6$  phases on densification and properties of  $\text{B}_4\text{C}$ .
2. Addition of binary (Eu and Sm) solid solution rare earth oxide on densification of  $\text{B}_4\text{C}$  and the phase evolution/stability of respective rare earth boride(s) would be investigated.
3. Evaluation of Irradiation performance of the developed  $\text{B}_4\text{C}$ - $\text{EuB}_6$  composites and its comparison with respect to monolithic  $\text{B}_4\text{C}$ .
4. Synthesis of nano boron carbide and its densification by field assisted sintering with a special emphasis on retaining fine scale microstructures
5. Investigation the densification behavior of  $\text{B}_4\text{C}$ - $\text{Eu}_2\text{O}_3$  mixture by FLASH sintering method

---

## References

---

1. Thevenot F. Boron carbide – a comprehensive review. *J Eur Ceram Soc*, 1990; **6**: 202-225.
2. Suri AK, Subramanian C, Sonber JK. Synthesis and consolidation of boron carbide: a review. *Int Mater Rev*. 2010; **55**[1]: 4-38.
3. Domnich, V., Reynaud, S., Haber, R.A., Chhowalla, M., Boron carbide: structure, properties and stability under stress. *J. Am. Ceram. Soc.*, 2011; **94**[11]: 3605–3628.
4. Dole S, Prochazka S, Doremus RH. Microstructural coarsening during sintering of boron carbide. *J Am Ceram Soc*. 1989; **72**: 958-966.
5. Angers R, Beauvy M. Hot-Pressing of Boron Carbide. *Ceram Int*. 1983; **10**[2]: 49-55.
6. Kuzenkova MA, Kislyi PS, Grabchuk BL. The structure and properties of sintered boron carbide. *J Less Comm Met*. 1979; **67**[1]: 217-223.
7. H. Lee and R. F. Speyer: ‘Pressureless sintering of boron carbide’, *J. Am. Ceram. Soc.*, 2003, **86**[9], 1468–1473.
8. R. F. Speyer and J. Lee: ‘Advances in pressureless densification of boron carbide’, *J. Mater. Sci.*, 2004, **39**, 6017–6021.
9. Skorokhod V, Vlajic MD, Krstic VD. Mechanical properties of pressureless sintered boron carbide containing TiB<sub>2</sub> phase. *J Mater Sci Lett*. 1996; **15**: 1337-1339.
10. Levin L, Frage N, Dariel MP. The Effect of Ti and TiO<sub>2</sub> Additions on the pressureless sintering of B<sub>4</sub>C. *Met Mater Trans A*. 1999; **30A**: 3201-3210.

11. Kim HW, Koh YH, Kim HE. Reaction sintering and mechanical properties of B<sub>4</sub>C with addition of ZrO<sub>2</sub>. *J Mater Res.* 2000; **15**[11]: 2431-2436.
12. Goldstein A, Geffen Y, Goldenberg A. Boron carbide-zirconium boride in-situ composites by the reactive pressureless sintering of boron carbide-zirconia mixtures. *J Am Ceram Soc.* 2000; **84**[3]: 642-644.
13. Subramanian, C., Roy, T.K., Murthy, T.S.R.Ch., Sengupta, P., Kale, G.B., Krishnaiah, M.V., Suri, A.K., Effect of zirconia addition on Pressureless sintering of boron carbide. *Ceram. Int.*, 2008; **34**: 1543-1549.
14. Grigor'ev ON, Koval'chuk VV, Zaporozhets OI. Synthesis and physicomechanical properties of B<sub>4</sub>C-VB<sub>2</sub> composites. *Powder Metall Metal Ceram.* 2006; **45**[1-2]: 47-58.
15. Goldstein A, Yeshurun Y, Goldenberg A. B<sub>4</sub>C/metal boride composites derived from B<sub>4</sub>C/metal oxide mixtures. *J Eur Ceram Soc.* 2007; **27**[2-3]: 695-700.
16. Yamada S, Hirao K, Yamauchi Y. High strength B<sub>4</sub>C–TiB<sub>2</sub> composites fabricated by reaction hot-pressing. *J Eur Ceram Soc.* 2003; **23**[7]: 1123-1130.
17. Sairam K, Sonber JK, Murthy TSRCh. Development of B<sub>4</sub>C–HfB<sub>2</sub> composites by reaction hot pressing. *Int J Refract Metals Hard Mater.* 2012; **35**: 32-40.
18. Sairam K, Murthy TSRCh, Sonber JK. Mechanical properties of HfB<sub>2</sub> reinforced B<sub>4</sub>C matrix ceramics processed by in-situ reaction of B<sub>4</sub>C, HfO<sub>2</sub> and CNT. In *Materials Challenges and Testing for Manufacturing, Mobility, Biomedical Applications and Climate*, Springer International Publishing, 2014; 87-96.
19. Sairam K, Sonber JK, Murthy TSRCh. Influence of spark plasma sintering parameters on densification and mechanical properties of boron carbide. *Int J Refract Metals Hard Mater.* 2014; **42**: 185-192.

20. Munir, Z.A., Anselmi-Tamburini, U., Ohyanagi, M., The effect of electric field and pressure on the synthesis and consolidation of materials: A review of the spark plasma sintering method. *J. Mater. Sci.* 2006; **41**: 763–777.
21. Hulbert, D.M., Jiang, D., Dudina, D.V., Mukherjee, A.K., The synthesis and consolidation of hard materials by spark plasma sintering. *Int. J. Refract. Met. Hard. Mater.* 2009; **27**: 367-375.
22. Klotz, B., Cho, K., Dowding, R. J., Sisson, S. D., Characterization of boron carbide consolidated by the plasma pressure compaction (P<sup>2</sup>C) method in air. *Ceram. Eng. Sci. Proc.* 2001; **22**[4]: 27–34.
23. Klotz, B. R., Cho, K. C., Dowding, R. J., Sintering aids in the consolidation of boron carbide (B<sub>4</sub>C) by the plasma pressure compaction (P<sup>2</sup>C) method. *Mater. Manuf. Process.* 2004; **19**[4]: 631–639.
24. Hayun, S., Kalabukhov, S., Ezersky, V., Dariel, M.P., Frage, N., Microstructural characterization of spark plasma sintered boron carbide ceramics. *Ceram Int* 2010; **36**: 451–457.
25. Schwetz, K. A., Grellner, W., The influence of carbon on the microstructure and mechanical properties of sintered boron carbide. *J. Less Comm. Met.*, 1981; **82**: 37-47.
26. Tkachenko, Y.G., Britun, V.F., Prilutskii, E.V., Yurchenko, D.Z., Bovkun, G.A., Structure and Properties of B<sub>4</sub>C-SiC Composites. *Powder Metall. Met. Ceram.*, 2005; **44**: 196-201.
27. Prochazka, S., Lake, B., Dense sintered boron carbide containing beryllium carbide. U.S. Patent No. 4005235, 1977.
28. Sigl, S.L., Processing and Mechanical Properties of Boron Carbide Sintered with TiC. *J. Eur. Ceram. Soc.*, 1998; **18**: 1521-1529.
29. Deng, J., Zhou, J., Feng, Y., Ding, Z., Microstructure and mechanical properties of hot-pressed B<sub>4</sub>C/(W,Ti)C ceramic composites. *Ceram. Int.*, 2002; **28**: 425-430.

30. Champagne, B., Angers, R., Mechanical Properties of Hot-Pressed B–B<sub>4</sub>C Materials. *J. Am. Ceram. Soc.*, 1979; **62**[3-4]: 149–153.
31. Mizrahi, I., Raviv, A., Dilman, H., Aizenshtein, M., Dariel, M. P., Frage, N., The effect of Fe addition on processing and mechanical properties of reaction infiltrated boron carbide-based composites. *J. Mater. Sci.*, 2007; **42**: 6923-6928.
32. Halverson, D.C., Pyzik, A.J., Aksay, I.A., Snowden, W.E., Processing of Boron Carbide-Aluminum Composites. *J. Am. Ceram. Soc.*, 1989; **72**[5]: 775-780.
33. Grigorev, O.N., Kotenko, V.A., Shcherbina, O.D., Bega, N.D., Dubovik, T.V., Subbotin, V.I., Mosina, T.V., Lychko, V.V., Berezhinskii, I.L., Production and Properties of Impact-Resistant Composites Based on Boron Carbide and Aluminum Nitride. *Powder Metall. Met. Ceram.*, 2010; **49**: 193-200.
34. Jiang, T., Jin, Z., Yang, J., Qiao, G., Property and Microstructure of Machinable B<sub>4</sub>C/BN Nanocomposites. *Key Eng. Mater.*, 2008; **368-372**: 936-939.
35. Sun C, Li Y, Wang Y. Effect of alumina addition on the densification of boron carbide ceramics prepared by spark plasma sintering technique. *Ceram Int.* 2014; **40**[8]: 12723-12728.
36. Skorokhod, V., Krstic, V.D., High strength-high toughness B<sub>4</sub>C-TiB<sub>2</sub> composites. *J. Mater. Sci. Lett.*, 2000; **19**: 237-239.
37. Huang, S.G., Vanmeensel, K., Van der Biest, O., Vleugels, J., In situ synthesis and densification of submicrometer-grained B<sub>4</sub>C-TiB<sub>2</sub> composites by pulsed electric current sintering. *J. Eur. Ceram. Soc.*, 2011; **31**: 637-644.
38. Yue, X.Y., Zhao, S.M., Lu, P., Chang, Q., Ru, H.Q., Synthesis and properties of hot pressed B<sub>4</sub>C-TiB<sub>2</sub> ceramic composite. *Mat. Sci. Eng. A.*, 2010; **A 527**: 7215-7219.
39. Zhu, S., Fahrenholtz, W.G., Hilmas, G.E., Zhang, S.C., Pressureless Sintering of Zirconium Diboride Using Boron Carbide and Carbon Additions. *J. Am. Ceram. Soc.*, 2007; **90**[11]: 3660-3663.

40. Huang S.G, Vanmeensel K, Vleugels J. Powder synthesis and densification of ultrafine B<sub>4</sub>C-ZrB<sub>2</sub> composite by pulsed electrical current sintering. *J Eur Ceram Soc.* 2014; **34**[8]: 1923-1933.
41. Skorokhod VV. Processing, microstructure and mechanical properties of B<sub>4</sub>C- TiB<sub>2</sub> particulate sintered composites. Part I. Pressureless sintering and microstructure evolution. *Powder Metall Metal Ceram.* 2000;**39**: 414-423.
42. Skorokhod VV. Processing, microstructure and mechanical properties of B<sub>4</sub>C- TiB<sub>2</sub> particulate sintered composites. Part II. Fracture and mechanical properties. *Powder Metall Metal Ceram.* 2000;**39**: 504-513.
43. Wei R, Zhang Y, Gong H. The effects of rare-earth oxide additives on the densification of pressureless sintering B<sub>4</sub>C ceramics. *Ceram Int.* 2013; **39**[6]: 6449-6452.
44. Madelung O, Rössler U, Schulz M, Boron compounds with lanthanides: properties of lanthanide hexaborides: EuB<sub>6</sub>, Landolt-Börnstein - Group III Condensed Matter 41D, Springer Materials, DOI: 10.1007/10681735\_116.
45. Jain, Ashish, R. Kandan. Determination of the thermodynamic stability of europium boride (EuB<sub>6</sub>). *Journal of Thermal Analysis and Calorimetry*, 2017, 132, 275-283.
46. Sonber, J.K., Murthy, TSRCh., Subramanian, C., Hubli, R.C., Suri, A.K. Synthesis, densification and characterization of EuB<sub>6</sub>, *Int. J. Refr. Met. Hard Mater.*, 2013, 38, 67-72.
47. M.L. Baucio, ASM engineered materials reference book, ASM International, USA (1994).
48. P. Dunner, H.J. Heuvel, M. Horle, Absorber materials for control rod systems of fast breeder reactors, *J Nucl Mater*, 1984, 124: 185-194.

49. B. Weidenbaum, E.W. Hoyt, D.L. Zimmerman, W.V. Cummings, K.C. Antony, Properties of some high temperature control materials, T. Simnad, L.R. Zumawalt (Eds.), Materials and fuels for high temperature nuclear energy applications, The M.I.T. Press, Massachusetts (1962), 315-343.
50. D. Gosset, M. Colin, Boron carbides of various compositions: an improved method for X-rays characterisation, *J. Nucl. Mater.*, 1991, 183: 161-173.
51. Chun Cheng, Kolan. M. Reddy, Akihiko Hirata, Takeshi Fujita, Mingwei Chen, Structure and mechanical properties of boron-rich boron carbides, *J Eur Ceram Soc*, 2017; 37[15]: 4514-4523.
52. Beauvy, M. Stoichiometric limits of carbon-rich boron carbide phases, *J Less Comm Met.*, 1983; 90[2]: 169-175.
53. M Bouchacourt, F Thevenot, The properties and structure of the boron carbide phase, *J Less Comm Met.*, 1981; 82: 227-235.
54. M Bouchacourt, F Thevenot, Analytical investigations in the B-C system, *J Less Comm Met.*, 1981; 82[1-2]: 219-226.
55. M Bouchacourt, F Thevenot, The melting of boron carbide and the homogeneity range of the boron carbide phase. *J. Less Common Met.*, 1979; 67: 327-31.
56. R.R. Ridgway, Boron carbide and the method of making the same. US patent no. 1897214, 1933.
57. A. Lipp, Boron carbide: production properties and application, *Technische Rundschau*, 1965.
58. G. Goller, C. Toy, A. Tekin, C. K. Gupta. The production of boron carbide by carbothermic reduction, *High Temp. Mater. Proc.*, 1996, 15, (1-2), 117-122.

59. F. Schroll, A. Vogt, Electrothermic production of boron carbide, US patent no. 2 163 293, 1939.
60. D. K. Bose, K. U. Nair, C. K. Gupta. Production of high purity boron carbide, High Temp. Mater. Proc., 1986; 7[2–3]: 133–140.
61. A. Alizadeh, E. T. Nassaj, N. Ehsani. Synthesis of boron carbide powder by a carbothermic reduction method, J. Eur. Ceram. Soc., 2004; 24: 3227–3234.
62. A. Alizadeh, E. T. Nassaj, N. Ehsani, H. R. Baharvandi. Production of boron carbide powder by carbothermic reduction from boron oxide and petroleum coke or carbon active, Adv. Appl. Ceram., 2006, 105[6]; 291–296.
63. W. Rafaniello, W. G. Moore. Producing boron carbide, US patent no. 4 804 525, 1989.
64. A. Aghai, C. Falamaki, B. E. Yekta, M. S. Afarani. Effect of seeding on the synthesis of B<sub>4</sub>C by the magnesiothermic reduction route, Ind. Ceram., 2002; 22[2]: 121–125.
65. E. G. Gray, Process for the production of boron carbide, US patent no. 2 834 651, 1958.
66. A. Muta, T. Geja, Method for producing boron carbide, US patent no. 3 338 679, 1967.
67. T. A. Zhang Z. H. Dou, H. Yang, Q. L. Ding. Preparation of boron carbide by magnesium reducing – SHS, J. North Eastern Univ., 2003; 24[10]: 935–938.
68. A. K. Khanra, M. M. Godkhindi. Synthesis of boron carbide by self –propagating high temperature synthesis, J. Aust. Ceram. Soc., 2005; 41[1]: 30–35.
69. F. Deng, H. Y. Xie, L. Wang. Synthesis of submicron B<sub>4</sub>C by mechanochemical method, Mater. Lett., 2006; 60[13–14]: 1771–1773.
70. J. Wei, B. Jiang, Y. Li, C. Xu, D. Wu. Straight boron carbide nanorods prepared from carbon nanotubes, J. Mater. Chem., 2002; 12: 3121–3124.

71. K. Yamada. Boron carbide articles formed from an amorphous boron/graphite powder mixture using a shock wave technique, *J. Am. Ceram. Soc.*, 1996; 79[4]: 1113–1116.
72. B. Chang, B. L. Gersten, S. T. Szewczyk, J. W. Adams. Characterization of boron carbide nanoparticles prepared by a solid state thermal reaction, *Appl. Phys. A*, 2007, 86A, 83–87.
73. S. T. Benton, R. David. Methods for preparing boron carbide articles, US patent no. 3 914 371, 1975.
74. A. S. Ramos, S. P. Taguchi, E. C. T. Ramos, V. L. Arantes, S. Ribeiro. High energy ball milling of powder B-C mixture, *Mater. Sci. Eng. A*, 2006; 422A[1–2]: 184–188.
75. R. G. Bourdio. Process of preparing boron carbide from boron halide and a hydrocarbon, US patent no. 3 334 967, 1967.
76. R. A. Clifton. Production of boron carbide whiskers, US patent no. 3 525 589, 1970.
77. E. W. James. Catalyst for growth of boron carbide crystal whiskers, US patent no. 3 423 179, 1969.
78. J. F. Ditter, F. J. Gerhart, R. E. Williams. Boron carbide, US patent no. 4 017 587, 1977.
79. I. M. MacKinnon, B. G. Reuben. The synthesis of boron carbide in an RF plasma, *J. Electrochem. Soc.*, 1975; 122[6]: 806–811.
80. H. Vincent, C. Vincent, M. P. Berthet, J. Bouix, G. Gonzalez. Boron carbide formation from  $\text{BCl}_3\text{-CH}_4\text{-H}_2$  mixtures on carbon substrates and in a carbon fibre reinforced Al composite, *Carbon*, 1996; 34[9]: 1041–1055.

81. M. Olsson, S. Soderberg, B. Stridh, J. O. Carlsson. Chemical vapour deposition of boron carbide: morphology and microstructure, *Thin Solid Films*, 1989; 172[1]: 95–109.
82. U. Jansson, J. O. Carlsson, B. Stridh, S. Soderberg, M. Olsson. Chemical vapor deposition of boron carbides: phase and chemical composition, *Thin Solid Films*, 1989; 172[1]: 81–93.
83. S. Mierzejewska, T. Niemyski. Preparation of crystalline boron carbide by vapour phase reaction, *J. Less Comm. Met.*, 1965; 8: 368–374.
84. S. Mondal, A. K. Banthia. Low temperature synthetic route for boron carbide, *J. Eur. Ceram. Soc.*, 2005; 25: 287–291.
85. A. Sinha, T. Mahata, B. P. Sharma. Carbothermal route for preparation of boron carbide powder from boric acid-citric acid gel precursor, *J. Nucl. Mater.*, 2002; 301: 165–169.
86. I. Yanase, R. Ogawara, H. Kobayashi. Synthesis of boron carbide powder from polyvinyl borate precursor, *Mater. Lett.*, 2009; 63: 91–93.
87. A. M. Hadian, J. A. Bigdeloo. The effect of time, temperature and composition on boron carbide synthesis by sol-gel method, *J. Mater. Eng. Perform.*, 2008; 17[1]: 44–49.
88. H. Konno, A. Sudoh, Y. Aoki, H. Habazaki. Synthesis of C/B<sub>4</sub>C composites from sugar–boric acid mixed solutions, *Mol. Cryst. Liq. Crys. A*, 2002; 386A[1]: 15–20.
89. I. Hasegawa, Y. Fujii, T. Takayama, K. Yamada. Phenolic resin–boron oxide hybrids as precursors for boron carbide, *J. Mater. Sci. Lett.*, 1999; 18:1629–1631.

90. M. G. L. Mirabelli, L. G. Sneddon. Synthesis of boron carbide via Poly vinylpentaborane precursors, *Am. Chem. Soc.*, 1988; 110[10]: 3305–3307.
91. H. Wada, S. Ito, K. Kuroda, C. Kato. The synthesis of boron nitride and boron carbide by pyrolysis of boric acid/1,2,3-prpanetriol condensation product', *Chem. Lett.*, 1985; 14[6]: 691–692.
92. L. Shi, Y. Gu, L. Chen, Y. Qian, Z. Yang, J. Ma. A low temperature synthesis of crystalline B<sub>4</sub>C ultrafine powders, *Solid State Commun.*, 2003; 128: 5–7.
93. Y. Gu, L. Chen, Y. Qian, W. Zhang, J. Ma. Synthesis of nanocrystalline boron carbide via a solvothermal reduction of CCl<sub>4</sub> in the presence of amorphous boron powder, *J. Am. Ceram. Soc.*, 2005; 88[1]: 225–227.
94. C. Ronning, D. Schwen, S. Eyhusen, U. Vetter, H. Hofsass. Ion beam synthesis of boron carbide thin films, *Surf. Coat. Technol.*, 2002; 158–159: 382–387.
95. B. M. Todorovic, I. Draganic, D. Vasiljevic-Radovic, N. Romdevic, M. Romccecic, M. Dramicanin, Z. Markovic. Synthesis of amorphous boron carbide by single and multiple charged boron ions bombardment of fullerene thin films, *Appl. Surf. Sci.*, 2007; 253: 4029–4053.
96. M. Carlsson, F. J. G. Garcia, M. Johnsson. Synthesis and characterization of boron carbide whiskers and thin elongated platelets, *J. Cryst. Growth*, 2002; 236: 466–476.
97. R. V. Krishnarao, J. Subrahmanyam. Studies on the formation of whiskers and platelets of B<sub>4</sub>C and BN, *J. Mater. Sci.*, 2004; 39: 6263–6269.
98. X. An, H. Zhai, H. Zhai, C. Cao, H. Zhu. Synthesis and characterization of boron carbide nanobelts, *Key Eng. Mater.*, 2007; 336–338[III]: 2166–2168.

99. R. Ma, Y. Bando. Investigation on the growth of boron carbide nanowires, *Chem. Mater.*, 2002; 14: 4403–4407.
100. I. A. Bairamashvili. Experience in production of articles from boron carbide for fast reactor control rods, *Proc. Techn. Committ. Meet. on ‘absorber materials, control rods and designs of backup reactivity shutdown systems for breakeven cores and burner cores for reducing plutonium stockpiles’*, Obninsk, Russia, July 1995, International Atomic Energy Agency, IAEA-TECDOC-884, 220–224.
101. A. W. Weimer. Carbide, nitride and boride materials, synthesis and processing, 89–95; 1997, London, Chapman & Hall.
102. K. U. Nair, D. K. Bose, C. K. Gupta. The production of elemental boron by fused salt electrolysis, *Miner. Proc. Extract. Metall. Rev.*, 1992; 9: 283–291.
103. A. Jain, S. Anthonysamy, K. Ananthasivan, R. Ranganathan, V. Mittal, S. V. Narsimhan, V. Mittal. Characterization of electrodeposited elemental boron, *Mater. Charact.*, 2008; 59: 890–900.
104. W. D. Kingery, in “Sintering’ 91,” edited by A. C. D. Chaklader and J. A. Lund, (Trans Tech, Brookfield, VT, 1992) P. 1.
105. G. C. Kuczynski, *Trans. AIME* 185; 1949: 169.
106. F. V. Lenel, *ibid.* 175; 1948: 878.
107. R. L. Coble, Initial sintering of alumina and hematite. *J. Amer. Ceram. Soc.* 41 (1958) 55.
108. W. D. Kingery, M. Berg. Study of the initial stages of sintering solids by viscous flow, evaporation-condensation, and self-diffusion. *J. Appl. Phys.* 26 (1955) 1205.

- 109.R. M. German, Z. A. Munir. Morphology relations during bulk-transport sintering. *Met. Trans 6A* (1975) 2229.
- 110.B. Y. Yin, L. S. wang. Studies on activated sintering of jet milled B<sub>4</sub>C powders, *Atom. Energy Sci. Technol.*, 2003, 37 (Suppl.), 70–72, 76.
- 111.K. M. Taylor, N. Falls, R. J. Palicka. Dense carbide composite for armor and abrasives, US patent no. 3 765 300, 1973.
- 112.D. Mallick, T. K. Kayal, J. Ghosh, O. P. Chakrabarti, S. Biswas, H. S. Maiti. Development of multi-phase B–Si–C ceramic composite by reaction sintering. *Ceram. Int.*, 2009; 35[4]: 1667–1669.
- 113.Yamada,S., Hirao,K., Yamauchi, Y., Kanzaki. S., B<sub>4</sub>C–CrB<sub>2</sub> composites with improved mechanical properties. *J. Eur. Ceram. Soc.*, 2003; **23**: 561–565.
- 114.Ostapenko,I. T., Slezov, V. V., Tarasov, R. V., Kartsev, N. F., Podtykan. V. P., Densification of boron carbide powder during hot pressing. *Sov. Powder Metall. Met. Ceram.*, 1979; **18**[5]: 312-316.
- 115.Hirao,K., Sakaguchi,S., Yamauchi, Y., Kanzaki, S., Yamada, S., Boron carbide based sintered compact and method for preparation thereof. US Patent no. 0059541A1; 2005.
- 116.S. Tuffe, J. Dubois, G. Fantozzi, G. Barbier. Densification, microstructure and mechanical properties of TiB<sub>2</sub>-B<sub>4</sub>C based composites, *Int. J. Refract. Met. Hard Mater.*, 1996, 14, 305–310.
- 117.A. Li, Y. Zhen, Q. Yin, L. Ma, Y. Yin. Microstructure and properties of (SiC,TiB<sub>2</sub>)/B<sub>4</sub>C composites by reaction hot pressing, *Ceram. Int.*, 2006, 32, 849–856.
- 118.Z. Panek. The synthesis of SiC-B<sub>4</sub>C ceramics by combustion during hot-pressing, *J. Eur. Ceram. Soc.*, 1993, 11, 231–236.

119. K. S. Singhal, B. P. Singh. Sintering of boron carbide under high pressures and temperatures', *Ind. J. Eng. Mater. Sci.*, 2006, 13, (2), 129–134.
120. Larsson, P., Axen, N., Hogmark, S., Improvements of the microstructure and erosion resistance of boron carbide with additives. *J. Mater. Sci.*, 2000; **35**: 3433-3440.
121. Namtae, C., Zhihao, B., Speyer, R.F., Density- and hardness-optimized pressureless sintered and post-hot isostatic pressed B<sub>4</sub>C. *J. Mater. Res.*, 2005; **20**[8]: 2110-2116.
122. G. F. Taylor. Apparatus for making hard metal compositions, US Patent No. 1,896,854, 1933.
123. G. D. Cremer. Powder metallurgy, US Patent No. 2,355,954, 1944.
124. R.W. Boesel, C.G. Goetzel. Progress in Spark Sintering, *POWDER MET INT*, 1971.
125. C.G. Goetzel, V.S. Demarchi, Electrically Activated Pressure-Sintering (Spark Sintering) of Titanium-Aluminum-Vanadium Alloy Powders. *Powder Met. Int.* 3 (1971) 80.
126. K. Inoue, Method of electrically sintering discrete bodies. US Patent 3,340,052, 1967.
127. S. Grasso, Y. Sakka, G. Maizza. Electric current activated/assisted sintering (ECAS): a review of patents 1906-2008. *Sci. Technol. Adv. Mater.*, 2009; 10[5].
128. Ghosh, D., Subhash, G., Sudarshan, T. S., Radhakrishnan, R., Gao, X. L., Dynamic Indentation Response of Fine-Grained Boron Carbide. *J. Am. Ceram. Soc.*, 2007; **90**[6]: 1850–1857.
129. Y. Kodera, N. Isibashi, T. Imai, T. Yamamoto, M. Ohyanagi, U. Anselmi-Tamburini, Z. A. Munir. Spark plasma sintering of less-crystallized boron carbide with defects, *Ceram. Trans.*, 2006, 194, 101–111.

130. Z. Shen, H. Peng and M. Nygren. Formidable increase in the superplasticity of ceramics in the presence of an electric field. *Adv. Mater.* 15 (2003) 1006.
131. M. Yue, J. Zhang, Y. Xiao, G. Wang, T. Li. New kind of NdFeB magnet prepared by spark plasma sintering. *IEEE Trans Magnetics* 39 (2003) 3551.
132. Sonber, J.K., Murthy, T.S.R.Ch., Subramanian, C., Fotedar, R.K., Hubli, R.C., Suri, A.K., Synthesis, Densification and Characterization of Boron Carbide. *Trans. Ind. Ceram. Soc.* 2013; 72[2]: 100-107.
133. Bertolino, N., Garay, J., Tamburini, U.A., Munir, Z.A., Electromigration effects in Al-Au multilayers. *Scr. Mater.* 2001; **44**[5]: 737-742.
134. Jianxin, D., Erosion wear of boron carbide ceramic nozzles by abrasive air-jets. *Mater. Sci. Eng. A*, 2005; **A408**: 227–233.
135. Mukhopadhyay, A., Venkateswaran, T., Basu, B., Spark plasma sintering may lead to phase instability and inferior mechanical properties: A case study with TiB<sub>2</sub>. *Scr. Mater.* 2013; **69**: 159-164
136. Kalyanaraman, R., Yoo, S., Krupashankara, M.S., Sudarshan, T.S., Dowding, R.J., Synthesis and consolidation of iron nanopowders. *Nanostructured Materials* 1998; **10**[8]: 1379–1392.
137. Ghosh, D., Subhash, G., Sudarshan, T. S., Radhakrishnan, R., Gao, X. L., Dynamic Indentation Response of Fine-Grained Boron Carbide. *J. Am. Ceram. Soc.*, 2007; **90**[6]: 1850–1857.
138. Sano, T., Randow, C.L., The Effect of Twins on the Mechanical Behavior of Boron Carbide. *Metall. Mater. Trans. A*, 2011; 42A: 570–574.
139. Mackinnon, I. D. R., Aselage, T. L., Van Deusen, S. B., High Resolution Imaging of Boron Carbide Microstructures. *Am. Inst. Phys. Conf. Proc.*, 1986; 140: 114–120.

140. Fujita T, Guan P, Reddy KM. Asymmetric twins in rhombohedral boron carbide. *Appl Phys Lett*. 2014; **104**:021907.
141. Xie KY, An Q, Toksoy MF. Atomic-level understanding of “asymmetric twins” in boron carbide. *Phys Rev Lett*. 2015; **17**: 175501.
142. Oleinik, G. S., Ostapchuk, T. V., Effect of pores on the cleavage of twinned boron carbide crystals. *Powder Metall. Met. Ceram.*, 1995; **34**: 500-504.
143. Moshtaghioun, B.M., Cumbreira-Hernández, F.L., Gómez-García, D., Bernardi-Martín, S.D., Domínguez-Rodríguez, A., Monshi, A., Abbasib, M.H., Effect of spark plasma sintering parameters on microstructure and room-temperature hardness and toughness of fine-grained boron carbide (B<sub>4</sub>C). *J. Eur. Ceram. Soc.*, 2013; **33**: 361–369.
144. Weiderhorn, S. M., Brittle fracture and toughening mechanisms in ceramics. *Ann. Rev. Mater. Sci.*, 1984; **14**: 373-403.
145. Moshtaghioun, B.M., Ortiz, A.L., Gómez-García, D., Domínguez-Rodríguez, A., Toughening of super-hard ultra-fine grained B<sub>4</sub>C densified by spark-plasma sintering via SiC addition. *J. Eur. Ceram. Soc.*, 2013; **33**: 1395–1401.
146. Sigl, L. S., Kleebe, H. J., Microcracking in B<sub>4</sub>C-TiB<sub>2</sub> Composites. *J. Am. Ceram. Soc.*, 1995; **78**[9]: 2374-2380.
147. B. Basu, K. Balani. *Advanced Structural Ceramics*, John Wiley & Sons, 2011; 44-47.
148. B. Eisenmann, H. Schäfer (1988), K.-H. Hellwege, A. M. Hellwege (ed.) *Elements, Borides, Carbides, Hydrides* · 6.2, Borides Landolt-Börnstein - Group III Condensed Matter 14A, SpringerMaterials

149. C. Wood., A. Zoltan, D. Emin, Paul E. Gray, Thermal Conductivity Behavior of Boron Carbides, 1985; In: Ashworth T., Smith D.R. (eds) Thermal Conductivity 18. Springer, Boston, MA
150. S. Yamada, K. Hirao, Y. Yamauchi, S. Kanzaki. Mechanical and electrical properties of  $B_4C-CrB_2$  ceramics fabricated by liquid phase sintering. *Ceram. Int.*, 2003; 29[3]: 299-304.
151. Varley F. Sears (1992): Neutron scattering lengths and cross sections, *Neutron News*, 3:3, 26-37
152. Nielsen L.F., Elasticity and Damping of Porous Materials and Impregnated Materials, *J Am. Ceram. Soc.*, 1984; 67[2]:93-98.
153. Duan J., Zhou T., Zhang L., Du J-G., Jiang G., Wang H-B, Elastic properties and electronic structures of lanthanide hexaborides, *Chin. Phys. B*, 2015; 24: 096201-1-9.